

**MEASUREMENT OF PROJECTILE BREAK-UP  
CROSS-SECTIONS IN  ${}^6,7\text{Li}+{}^{112}\text{Sn}$  REACTIONS**

*By*

**DIPAYAN CHATTOPADHYAY**

**PHYS01201504019**

**Bhabha Atomic Research Centre, Mumbai**

*A thesis submitted to the*

*Board of Studies in Physical Sciences*

*In partial fulfillment of requirements*

*for the Degree of*

**DOCTOR OF PHILOSOPHY**

*of*

**HOMI BHABHA NATIONAL INSTITUTE**



December, 2018

# Homi Bhabha National Institute

## Recommendations of the Viva Voce Committee

As members of the Viva Voce Committee, we certify that we have read the dissertation prepared by Mr. Dipayan Chattopadhyay entitled "Measurement of projectile break-up cross-sections in  ${}^6,7\text{Li}+{}^{112}\text{Sn}$  reactions" and recommend that it may be accepted as fulfilling the thesis requirement for the award of Degree of Doctor of Philosophy.

Chairman – Dr. D. C. Biswas		Date: 13/12/2018
Guide / Convener – Dr. S. Santra		Date: 13/12/2018
Co-guide - Dr. K. Mahata		Date: 13/12/2018
Examiner – Prof. Rajdeep Chatterjee		Date: 13/12/18
Member 1- Prof. R. Palit		Date: 13/12/2018
Member 2- Dr. R. Tripathi		Date: 13/12/2018

Final approval and acceptance of this thesis is contingent upon the candidate's submission of the final copies of the thesis to HBNI.

I/We hereby certify that I/we have read this thesis prepared under my/our direction and recommend that it may be accepted as fulfilling the thesis requirement.

Date: 13/12/2018

Place: HBNI,

ANUSHAKTI NAGAR

  
Co-guide

  
Guide

## STATEMENT BY THE AUTHOR

This dissertation has been submitted in partial fulfillment of requirements for an advanced degree at Homi Bhabha National Institute (HBNI) and is deposited in the library to be made available to borrowers under rules of the HBNI.

Brief quotations from this dissertation are allowable without special permission, provided that accurate acknowledgement of source is made. Requests for permission for extended quotation from or reproduction of this manuscript in whole or in part may be granted by the Competent Authority of HBNI when in his or her judgment the proposed use of the material is in the interests of scholarship. In all other instances, however, permission must be obtained from the author.

Dipayan Chattopadhyay  
(Dipayan Chattopadhyay)

## DECLARATION

I, hereby declare that the investigation presented in the thesis has been carried out by me. The work is original and the work has not been submitted earlier as a whole or in part for a degree/diploma at this or any other Institution/University.

*Dipayan Chattopadhyay*  
(Dipayan Chattopadhyay)

# List of Publications arising from the thesis

## I. Journals:

1. “Elastic, inelastic and inclusive alpha cross-sections in  ${}^6\text{Li}+{}^{112}\text{Sn}$  system”,  
D. Chattopadhyay, S. Santra, A. Pal, A. Kundu, B. K. Nayak, K. Mahata, K. Ramachandran, R. Tripathi, V. V. Parkar, S. Sodaye, D. Sarkar, B. Pandey and G. Kaur,  
*EPJ Web of Conferences*, **2016**, *117*, 06022.
2. “Resonant, direct, and transfer breakup of  ${}^6\text{Li}$  by  ${}^{112}\text{Sn}$ ”,  
D. Chattopadhyay, S. Santra, A. Pal, A. Kundu, K. Ramachandran, R. Tripathi, D. Sarkar, S. Sodaye, B. K. Nayak, A. Saxena, and S. Kailas ,  
*Phys. Rev. C*, **2016**, *94*, 061602(R).
3. “Role of cluster structure in the breakup of  ${}^7\text{Li}$ ”,  
D. Chattopadhyay, S. Santra, A. Pal, A. Kundu, K. Ramachandran, R. Tripathi, B. J. Roy, T. N. Nag, Y. Sawant, B. K. Nayak, A. Saxena, and S. Kailas ,  
*Phys. Rev. C*, **2018**, *97*, 051601(R).
4. “Resonant breakup of  ${}^8\text{Be}$  in  ${}^{112}\text{Sn}({}^7\text{Li}, {}^8\text{Be} \rightarrow 2\alpha)$  reaction” ,  
D. Chattopadhyay, S. Santra, A. Pal, A. Kundu, K. Ramachandran, R. Tripathi, B. J. Roy, Y. Sawant, B. K. Nayak, A. Saxena, and S. Kailas,  
*Phys. Rev. C*, **2018**, *98*, 014609.

## II. Conferences:

1. "Study of direct and sequential break-up reactions in  ${}^6\text{Li}+{}^{112}\text{Sn}$  system" ,  
D. Chattopadhyay, S. Santra, A. Pal, A. Kundu, B. K. Nayak, K. Mahata, K. Ramachandran, R. Tripathi, V. V. Parkar, G. Kaur, D. Sarkar, S. Sodaye, B. Pandey and S. Kailas, *DAE Symp. On Nucl. Phys.*, **2015**, *60*, 338.
  
2. "Observation of breakup via  $1^+$  resonant state of  ${}^6\text{Li}$ ",  
D. Chattopadhyay, S. Santra, A. Pal, A. Kundu, K. Ramachandran, R. Tripathi, D. Sarkar, S. Sodaye, B. K. Nayak, A. Saxena and S. Kailas, *DAE Symp. On Nucl. Phys.*, **2016**, *61*, 360.
  
3. "Inclusive  $\alpha$  and  $d$  in  ${}^6\text{Li}+{}^{112}\text{Sn}$  system" ,  
D. Chattopadhyay, S. Santra , A. Pal, A. Kundu, K. Ramachandran, R. Tripathi, D. Sarkar, S. Sodaye, B. K. Nayak, A. Saxena and S. Kailas, *DAE Symp. On Nucl. Phys.*, **2016**, *61*, 466.
  
4. " $1p$  transfer induced breakup in  ${}^7\text{Li}+{}^{112}\text{Sn}$  reaction",  
D. Chattopadhyay, S. Santra, A. Pal, A. Kundu, K. Ramachandran, R. Tripathi, B. J. Roy, Y. Sawant, D. Sarkar, J. Pandey, B. K. Nayak, A. Saxena and S. Kailas, *Proceedings of the international conference in nuclear physics with energetic heavy ion beams, Chandigar,INDIA: abstract book*, **2017**.
  
5. "Resonant breakup of  ${}^8\text{Be}$  in  ${}^{112}\text{Sn}({}^7\text{Li},{}^8\text{Be}\rightarrow\alpha + \alpha)$  reaction" ,  
D. Chattopadhyay, S. Santra, A. Pal, A. Kundu, K. Ramachandran, R. Tripathi, B. J. Roy, Y. Sawant, T. N. Nag, B. K. Nayak, A. Saxena and S. Kailas, *DAE Symp. On Nucl. Phys.*, **2017**, *62*, 374.

6. “Direct and sequential breakup in  ${}^7\text{Li}+{}^{112}\text{Sn}$  reaction” ,  
S. Santra, D. Chattopadhyay, A. Pal, A. Kundu, K. Ramachandran, R. Tripathi,  
B. J. Roy, Y. Sawant, T. N. Nag, B. K. Nayak, A. Saxena and S. Kailas, *DAE  
Symp. On Nucl. Phys.*, **2017**, *62*, 416.

Dipayan Chattopadhyay  
(Dipayan Chattopadhyay)

*Dedicated to*  
***My Parents***

## Acknowledgements

I acknowledge with a sense of deep and sincere gratitude, the meticulous guidance, ingenious discussions and steady encouragement rendered by **Prof. Satyaranjan Santra**, Professor, Homi Bhabha National Institute, Mumbai. I owe the greatest debt of gratitude to him for suggesting the research problem followed by ever willing help and the freedom extended to me throughout the period of my research. I greatly appreciate his support and guidance not only in research but also in my day to day life. Working under his guidance, I have earned a great deal of scientific knowledge which has shaped my research skills and encouraged me to pursue in research field. This document would not exist without his guidance and patience.

I am profoundly obliged to **Prof. S. Kailas**, Former Group Director, Physics Group, BARC, for his encouragement and providing the necessary suggestions needed for this work.

I take this opportunity to thank **Dr. K. Mahata, Dr. R. Tripathi, Dr. V. V. Parkar, Dr. P. C. Rout, Dr. K Ramachandran** and **Dr. B. J. Roy** for their constant encouragement, valuable discussion, and moral support from time to time throughout the course of the work.

I am deeply thankful to **Prof. B. K. Nayak**, Dean, Academic, Mathematical and Physical sciences, HBNI and **Prof. A. Saxena**, Former Head, Nuclear Physics Division, BARC, Mumbai for their support and needful help during the various stages of my research work.

I also take this opportunity to express my sincere thanks to all the faculty members of my committee (**Prof. D. C Biswas, Prof. S. Santra, Dr. K. Mahata, Dr. R. Tripathi and Prof. R. Palit**) for their valuable suggestions in regards to complete this task and for providing me constant encouragement.

I would like to express my gratitude and thanks to **Dr. D. Syam, Dr. Srijit Bhattacharya**, and **Dr. Goutam Goswami** for their encouragement and constant support.

I am also grateful to my friends **Kum. Neha Grover, Mr. Asim Pal, Mrs. Dona Ghosh, Kum. Ananya Kundu, Mr. T. N. Nag, Mr. Debashish Sarkar, Mr. Raman Gandhi, Dr. Sanat Pandit, Dr. Gayatri Mohanto, Kum. Sukanya De, Mr. Shrikanta Goswami, Kum. Shilpi Gupta, Mr. Sandeep Joshi, Mr. Raman Sehgal**, my batchmates of 57<sup>th</sup> batch at training school and all of my collaborators for providing me the constant help, moral support and encouraging environment to take the challenges.

I concede my heartiest admiration and gratitude for my parents (**Mr. Dipak Chattopadhyay** and **Mrs. Archana Chattopadhyay**) for the moral support and countless blessings. I am also thankful to all the staff of NPD and IADD for constant support.

Dipayan chattopadhyay  
(Dipayan Chattopadhyay)

# Contents

<b>SYNOPSIS</b>	<b>xiv</b>
<b>List of Figures</b>	<b>xxiv</b>
<b>List of Tables</b>	<b>xxx</b>
<b>1 Introduction</b>	<b>1</b>
1.1 Interesting features involving weakly bound nuclei . . . . .	3
1.1.1 Cluster structure . . . . .	4
1.1.2 Borromean structure . . . . .	5
1.1.3 Extended density distribution . . . . .	7
1.1.4 Synthesis of super-heavy element . . . . .	9
1.1.5 Soft dipole resonance . . . . .	10
1.1.6 Astrophysical interest . . . . .	11
1.2 Breakup reactions mechanism . . . . .	12
1.2.1 Direct breakup . . . . .	13
1.2.2 Sequential breakup . . . . .	14
1.2.2.1 Resonant breakup . . . . .	14
1.2.2.2 Transfer breakup . . . . .	16
1.2.3 Fragment capture or Incomplete fusion . . . . .	17
1.2.4 Complete fusion . . . . .	17

1.3	General Motivation of the thesis . . . . .	18
<b>2</b>	<b>Experimental methods</b>	<b>21</b>
2.1	Generation and acceleration of the projectile . . . . .	22
2.2	Interaction of charged particle with matter . . . . .	24
2.3	Semiconductor detector for charged particle detection . . . . .	25
2.3.1	Silicon surface barrier detector . . . . .	25
2.3.2	Silicon strip detector . . . . .	26
2.4	Experimental setup . . . . .	26
2.5	Electronics for signal processing and DAQ . . . . .	29
2.6	Analysis method for breakup fragments in coincidence . . . . .	30
2.7	Coincidence efficiency of Double Sided Silicon Strip Detector (DSSD) array	35
<b>3</b>	<b>Coupled reaction channels formalism</b>	<b>39</b>
3.1	Introduction . . . . .	39
3.2	Coupled-channels method . . . . .	41
3.3	Born approximation and DWBA method . . . . .	47
3.4	Continuum Discretized Coupled Channels method . . . . .	50
<b>4</b>	<b>Direct, resonant and transfer breakup of <math>{}^6\text{Li}</math></b>	<b>53</b>
4.1	Introduction . . . . .	53
4.2	Identification of breakup modes : Relative energy distribution . . . . .	55
4.3	Breakup cross sections . . . . .	58
4.3.1	Determination of experimental breakup cross-section from coinci- dence spectra . . . . .	58
4.3.2	Reconstruction of emission angle of projectile like fragment . . . . .	61
4.3.3	Direct and Resonant breakup of ${}^6\text{Li} \rightarrow \alpha + d$ . . . . .	62
4.3.4	Transfer breakup . . . . .	66
4.4	Summary and conclusions . . . . .	68

<b>5</b>	<b>Direct, resonant and transfer breakup of <math>{}^7\text{Li}</math></b>	<b>70</b>
5.1	Introduction . . . . .	70
5.2	Identification of breakup modes . . . . .	72
5.2.1	Relative energy distributions . . . . .	72
5.2.2	Q-value distributions . . . . .	77
5.3	Determination of breakup cross-section . . . . .	81
5.3.1	Direct and resonant breakup of ${}^7\text{Li}$ . . . . .	82
5.3.2	$-1n$ and $-2n$ transfer breakup of ${}^7\text{Li}$ . . . . .	84
5.3.3	$+1p$ transfer breakup of ${}^7\text{Li}$ . . . . .	88
5.3.3.1	CRC calculation: . . . . .	90
5.3.3.2	CDCC-CRC calculation: . . . . .	93
5.4	$-1n$ and $-1p$ transfer cross-section of ${}^7\text{Li}$ . . . . .	93
5.5	The effect of breakup and transfer couplings on elastic scattering . . . . .	97
5.6	Proximity of breakup to target . . . . .	99
5.6.1	Distribution of $ E_1 - E_2 $ versus $E_{\text{rel}}$ . . . . .	99
5.6.2	Distribution of $\beta$ versus $\theta_{12}$ . . . . .	101
5.7	Summary and conclusions . . . . .	104
<b>6</b>	<b>Understanding alpha particle productions in <math>{}^6\text{Li}+{}^{112}\text{Sn}</math> reaction</b>	<b>108</b>
6.1	Introduction . . . . .	108
6.2	Data analysis and discussion . . . . .	109
6.2.1	Elastic and inelastic scattering . . . . .	109
6.2.2	Inclusive $\alpha$ . . . . .	112
6.2.3	Disentangling $\alpha$ contributions . . . . .	112
6.2.4	Systematics of inclusive breakup $\alpha$ . . . . .	117
6.2.5	Cross-section of inclusive ${}^3\text{He}$ , $t$ , $d$ and $p$ . . . . .	120
6.3	Summary and conclusions . . . . .	120

<b>7 Summary and future outlooks</b>	<b>123</b>
7.1 Summary . . . . .	123
7.2 Future outlooks . . . . .	124
<b>References</b>	<b>127</b>

## SYNOPSIS

Towards the cessation of the 19<sup>th</sup> century many scientists thought that no new advances in physics remained to be made. Yet within ten years Henri Becquerel, Pierre and Marie Curie as well as Ernest Rutherford succeed in marking out an entirely new branch of physics called radioactivity. In 1911, the famous gold-foil experiment carried out by Rutherford and his group has laid the foundation of nuclear physics. Later the discovery of neutron by Chadwick confirmed the composition of nucleus as a combination of proton and neutron. With the motivation to extract the structural information of nucleus, such as size, shape, lifetimes etc., first artificial nuclear reaction involving accelerated beam of projectiles with stationary target was initiated by Cockcroft and Walton in 1932 [1]. After the invention of artificial accelerators the production of nuclei by fusion became possible and as a result nuclear landscape has widened greatly. So to quest for the origin of matter one has to rely on the studies of the nuclear reaction. However, only few nuclei are stable (around 300), others are unstable. The plot of the neutron number versus proton number known as Segre Chart distinguishes the stable nuclei from the unstable ones that spread on bothsides of the stability line. If we go farther away from the stability line, nuclei become more unstable and instability reaches to a point, where emission of particle starts to achieve the stability. To understand the whole region of the Segre Chart, the complete information of stable and unstable nuclei is required. Lots of studies have been done near the stability line, but the knowledge of nuclei far away from the stability valley is insufficient, because those nuclei have very short lifetime or radioactive. The properties of these nuclei also influence explosive astrophysical events such as supernovae. However, direct measurement of structural properties of these nuclei is not possible because of their short life times and limited availability. So, one has to search for the indirect methods in order to obtain the structural information of these rare exotic nuclei. The weakly bound stable projectiles, like  ${}^6\text{Li}$  and  ${}^9\text{Be}$ , show somewhat similar behaviour (such as low breakup threshold, core+valence cluster structure, etc.) as that of the exotic nuclei.

Therefore, by studying the reaction mechanism of  ${}^6,7\text{Li}$  and  ${}^9\text{Be}$ , the nuclei which can be made available easily and abundantly from the stable beam accelerators, one can predict some of the interesting properties of the weakly bound exotic nuclei. Motivated by this, the studies chosen for the present thesis work is on the reactions involving weakly bound projectiles  ${}^6\text{Li}$  and  ${}^7\text{Li}$ .

As  ${}^6,7\text{Li}$  nuclei are weakly bound by nature and exhibit cluster structure like  $\alpha + x$ , where  $x$  is a deuteron or triton, while moving in the field of the target, they may directly dissociate into their cluster constituents or may get in-elastically excited to one of the resonant states (with finite life time) before dissociating into ‘ $\alpha$ ’ and ‘ $x$ ’ fragments. Several measurements involving the above weakly bound projectiles show significantly larger cross sections for the inclusive alpha particle production compared to the production of the complementary fragment ‘ $x$ ’. This indicates that there are mechanisms other than direct (and resonant)  $\alpha + x$  breakup which are responsible for such a large production of alpha particles [2]. The other processes may include the exchange of nucleons between the weakly bound projectile and the target forming the intermediate quasi-bound projectile-like fragments which in turn dissociate into two fragments out of which at least one of the fragments is  $\alpha$ , and this process is known as transfer breakup.

Another interesting observation in the reactions involving weakly bound projectiles is the suppression of complete fusion cross section at above barrier energies [3,4]. Due to low breakup threshold, there is a certain probability of breakup of the projectile before it reaches the fusion barrier of a target nucleus leading to loss of incoming flux. It may so happen that only one of the breakup fragments gets captured and the other escapes. So, the chance of complete capture of whole projectile by the target is reduced. However, the effect on complete capture probability, i.e., on complete fusion cross section, depends on the location of the breakup associated with the time scale of different states of intermediate projectile-like nuclei through which the breakup occurs. It may be possible that both direct as well as sequential breakup processes are responsible for the suppression

of complete fusion and the enhancement of incomplete-fusion cross-sections. As the heavy ion transfer reaction is peripheral, the probability of particle pickup/stripping by/from the projectile observed to be the maximum at the grazing distance. Now, if the states of intermediate projectile-like nuclei through which the breakup occurs is short lived ( $\sim 10^{-22}$  sec.) then the breakup occurs near to the target and only one of the two breakup fragments gets captured by the target leading to the suppression of complete fusion cross-section. So, apart from the direct breakup of the projectile to its cluster constituents, the transfer breakup has also its own importance.

Now, the main motivation of the present thesis work was to measure and find out the dominant modes of breakup of the projectiles  ${}^6,{}^7\text{Li}$  and understand the underlying reaction mechanisms involving weakly bound projectiles. Several measurements involving  ${}^6,{}^7\text{Li}$  projectiles exist in the literature [5,6,7] where some of these breakup channels have been studied but the complete reaction mechanism is still far from being fully understood. So, it is of tremendous interest to study the topic of breakup reactions in the present context. There are inconsistencies in the existing data of different breakup cross sections leading to different conclusions on the dominance of various breakup modes. Of course, these measurements involve different targets and sometimes with same targets but different energies. So, it is worth looking for the dependence on target as well as beam energy. With these motivations, we proposed to study the breakup reaction mechanisms in the reactions involving  ${}^6,{}^7\text{Li}$  as projectiles and a medium mass target  ${}^{112}\text{Sn}$ , as the experimental data with medium mass targets are scarce. To study the energy dependence, measurements have also been done for a particular projectile-target system at two different energies.

Several studies have shown that the resonant breakup is one of the most dominant breakup channels. For example, in case of  ${}^6\text{Li}+{}^{209}\text{Bi}$  system the breakup of  ${}^6\text{Li}$  into  $\alpha + d$  via its  $3^+$  resonance state was dominant [6]. Similarly, in  ${}^7\text{Li}+{}^{65}\text{Cu}$  reaction, the  $1n$  transfer followed by breakup of  ${}^6\text{Li}$  into  $\alpha + d$  via  $3^+$  and  $2^+$  resonances has been observed [5]. It has been well established that the relative angular momentum of  $\alpha$  and  $d$  involved

in the above breakup correspond to  $L=2$  [8]. So, one would expect the breakup of  ${}^6\text{Li}$  via all three resonance states with  $L=2$ , i.e.,  $3^+$ ,  $2^+$  and  $1^+$  states should occur. But, so far there is no measurement available in the literature on the experimental breakup cross-section of  ${}^6\text{Li}$  into  $\alpha + d$  via its  $1^+$  resonance state. So, it would be interesting to look for such new breakup channels that may help understand the reaction mechanism better. The search for the  $1^+$  resonant breakup state along with the breakup via other well known resonances and dominant transfer triggered channels will provide deeper insight to explain large cross sections for inclusive  $\alpha$  production.

Similar measurements have also been carried out for  ${}^7\text{Li}$  induced reactions, namely  ${}^7\text{Li}+{}^{112}\text{Sn}$  reaction, where we search for the breakup via new resonant states of  ${}^7\text{Li}$ , different transfer triggered breakup channels, possible new channels of direct breakup ( ${}^7\text{Li}\rightarrow{}^6\text{He}+p$ ) and compare their relative cross sections. The cluster structure of a light nucleus plays an important role in predicting possible breakup channels. The  ${}^7\text{Li}$  as a cluster of  $\alpha$  and  $t$  with a binding energy of only 2.47 MeV is very well known. Direct breakup of  ${}^7\text{Li}$  into  $\alpha + t$  and sequential breakup via the first resonance state ( $7/2^-$ , 4.63 MeV) of the cluster have been measured in a few systems. But, there is no measurement available on the sequential breakup corresponding to the second resonance state ( $5/2^-$ , 6.67 MeV). The study of the second resonance state is however very important as various studies on elastic scattering show a significant effect of coupling of the  $5/2^-$  state of  ${}^7\text{Li}$  [9,10]. So, the interest was to measure this new channel to understand the mechanism of  $\alpha + t$  resonance breakup.

Cluster models of the structure of the light nuclei often provide a rather simple description of some of the energy levels which are difficult to access in the usual shell model framework. So far the cluster structure of  ${}^7\text{Li}$  as  $\alpha + t$  and  ${}^6\text{Li}+n$  is well established [11]. But  ${}^7\text{Li}$  may also exist as a cluster of  ${}^6\text{He}+p$ , but no experimental observation is available. So the observation of the direct breakup of  ${}^7\text{Li}$  into  ${}^6\text{He}$  and  $p$ , i.e.,  ${}^7\text{Li}\rightarrow{}^6\text{He}+p$ , will provide a direct evidence on the possibility of an additional cluster structure of  ${}^7\text{Li}$

and help us understand the complete structure of  ${}^7\text{Li}$  and its energy levels.

Another interesting aspect is the proximity of the projectile breakup to the target nucleus (related to the timescale of the breakup). If the breakup occurs prior to reaching or near the fusion barrier, then that breakup which is known as near target breakup is responsible for CF suppression. On the other hand if the breakup occurs far away from the target nucleus, known as asymptotic breakup, it would not be responsible for complete fusion suppression. So to identify the breakup states that are responsible for complete fusion suppression it is essential to separate out the asymptotic breakup components from the near target one.

Based on the above mentioned motivations, several measurements were carried out involving weakly bound projectiles  ${}^6\text{Li}$  and  ${}^7\text{Li}$  at a beam energy of 30 MeV ( $E/V_B \sim 1.35$ ) using 14UD BARC-TIFR Pelletron-Linac facility. Self-supporting enriched ( $> 99\%$ )  ${}^{112}\text{Sn}$  foil of thickness  $\sim 540 \mu\text{g}/\text{cm}^2$  was used as target. In order to detect all the desired breakup channels mentioned above in coincidence, an large array of maximum five-telescopes consisting of ten double sided silicon strip detectors as  $\Delta E$ -E have been used. Two Si surface barrier detectors ( $M_1$  and  $M_2$ ) of thickness 1 mm were placed at  $\pm 20^\circ$  with respect to the beam direction for normalization and beam monitoring. In addition, there were five single telescopes ( $T_1$ -  $T_5$ ) of silicon surface barrier detectors (with  $\Delta E \sim 50 \mu\text{m}$ ,  $E \sim 1000$ - $2000 \mu\text{m}$ ) placed on the second rotatable arm of the scattering chamber to measure the elastic scattering angular distribution covering additional angular range as well as some overlapping angles for normalizing the elastic counts of the strip telescopes. In addition, the measurements involving  ${}^6\text{Li}$  beam has been performed at another energy of 22 MeV (around the Coulomb barrier) to investigate the energy dependence of different breakup cross-sections. For the determination of inclusive cross-sections for the production of different charged particle like  $\alpha$ ,  ${}^3\text{He}$ ,  $t$ ,  $d$  and  $p$  the measurements have been carried out for five different energies ranging from 22 MeV to 30 MeV in steps of 2 MeV. The outcomes of the above measurements are as follows:

### **(a) Direct, resonant and transfer breakup in ${}^6\text{Li}$ by ${}^{112}\text{Sn}$ :**

The major projectile-breakup channels observed in the  ${}^6\text{Li}+{}^{112}\text{Sn}$  reaction at  $E_{beam} = 30$  and  $22$  MeV are (i) direct and sequential breakup of  ${}^6\text{Li} \rightarrow \alpha + d$ , (ii) sequential breakup via  $1n$  stripping followed by breakup into  $\alpha + p$ , and (iii) sequential breakup via  $1d$  pickup followed by breakup into  $\alpha + \alpha$  [12]. The sequential  $\alpha + d$  breakup modes of  ${}^6\text{Li}$  via its resonant state ‘ $1^+$ ’ (5.65 MeV) along with ‘ $2^+$ ’ (4.31 MeV), and ‘ $3^+$ ’ (2.18 MeV) states in the continuum have been identified for the first time through the relative energy distribution and the cross-sections for all these breakup channels were measured [12]. Breakup via the  $3^+$  state of  ${}^6\text{Li}$  in the continuum, dominates the total  $\alpha + d$  breakup cross section at  $E_{beam} = 30$  MeV. However, at  $E_{beam} = 22$  MeV, only direct breakup of  ${}^6\text{Li}$  into  $\alpha + d$  is observed. The breakup channels proceeding via  $1n$  and  $1d$  transfer reactions are observed at both the energies. The relative energy spectra show that  $\alpha + p$  breakup proceeds via the ground state of  ${}^5\text{Li}$  ( $E_{rel}=1.97$  MeV) for both the beam energies. For the  $\alpha + \alpha$  breakup channels, the breakup at  $E_{beam} = 22$  MeV proceeds only through the  $0^+$  state of  ${}^8\text{Be}$  whereas at  $E_{beam} = 30$  MeV it proceeds through both  $0^+$  (0.092 MeV) and  $2^+$  (3.12 MeV) states of  ${}^8\text{Be}$ . Experimental  $\alpha + d$  breakup cross sections via three resonance states of  ${}^6\text{Li}$  reasonably agree with the CDCC calculations. A comparison of breakup cross sections at two energies reveals that the cross sections for  $\alpha + d$  breakup for the present system are more than  $\alpha + p$  as well as  $\alpha + \alpha$  breakup. All the breakup channels observed in the present measurements produce  $\alpha$  as one of the two breakup fragments and contribute to the total inclusive  $\alpha$  yield. The additional channels, i.e.,  $\alpha + x$  breakup followed by  $x$  capture, and  $1p$  transfer followed by  $\alpha + n$  breakup are expected to have significant contributions in inclusive  $\alpha$ .

### **(b) Direct, resonant and transfer breakup in ${}^7\text{Li}$ by ${}^{112}\text{Sn}$ :**

Direct and sequential breakup of the projectile in the  ${}^7\text{Li}+{}^{112}\text{Sn}$  reaction has been measured at a beam energy of 30 MeV. Cross sections for sequential breakup of  ${}^7\text{Li}$  into  $\alpha$  and  $t$  cluster fragments via its second resonant state of  $5/2^-$  (6.68 MeV) in the continuum

have been measured for the first time along with the first resonant state ( $7/2^-$ , 4.63 MeV) [13]. Probabilities of sequential breakup proceeding through  $-1n$  and  $-2n$  transfer channels, i.e., ( ${}^7\text{Li}, {}^6\text{Li}$ ) and ( ${}^7\text{Li}, {}^5\text{Li}$ ) reactions followed by breakup, into  $\alpha + d$  and  $\alpha + p$  respectively were found to dominate over  $\alpha + t$  breakup. Measured cross sections for the above breakup channels and elastic scattering have been compared with the coupled-channels calculations to understand the reaction mechanism involving the weakly bound projectile  ${}^7\text{Li}$ . Significant cross section for direct breakup of  ${}^7\text{Li} \rightarrow {}^6\text{He} + p$  has also been measured for the first time, indicating the importance of the new ( ${}^6\text{He} + p$ ) cluster configuration that may be necessary to understand the complete structure of  ${}^7\text{Li}$  and its energy levels [13].

The  $\alpha - \alpha$  coincidence data from the above measurements have also been analyzed to investigate the possible breakup of  ${}^8\text{Be}$  via new resonance states. Relative energy distribution along with Monte-Carlo simulation in fact confirms the observation of breakup of  ${}^8\text{Be}$  from its  $4^+$  (11.35 MeV) resonant state for the first time along with its well-known  $0^+$  (92 keV) and  $2^+$  (3.12 MeV) resonances [14]. The experimental cross sections for  $+1p$  transfer induced breakup in ( ${}^7\text{Li}, {}^8\text{Be} \rightarrow 2\alpha$ ) reaction through different resonance states of  ${}^8\text{Be}$  have been obtained and compared with the coupled channels calculations. The spectroscopic factors for several new overlaps responsible for  ${}^8\text{Be}$  production have been obtained by reproducing the experimental  $\alpha + \alpha$  breakup cross-sections.

**(c) Elastic, inelastic and inclusive alpha cross-sections in  ${}^6\text{Li} + {}^{112}\text{Sn}$  system:**

The differential cross sections for inelastic scattering and inclusive alpha have been extracted for  ${}^6\text{Li} + {}^{112}\text{Sn}$  system at a beam energy of 30 MeV. Coupled-channels calculations are performed to include the effect of projectile breakup and target excitations. The normalized cluster-folded potential that explains simultaneously the elastic and two inelastic states are used to calculate the projectile breakup cross sections. The calculated non-capture breakup cross section of  ${}^6\text{Li} \rightarrow \alpha + d$  is found to be very small compared to the inclusive alpha yield suggesting possible  $\alpha$  contributions from various transfer induced breakup channels [15].

In order to understand the origin of production of large  $\alpha$  particle, the  ${}^6\text{Li}+{}^{112}\text{Sn}$  reaction was studied at near-barrier energies. Angular distributions were performed at five bombarding energies, namely, 22.0, 24.0, 26.0, 28.0 and 30.0 MeV. The distributions were characterized by a Gaussian shape, which was integrated in order to obtain  $\alpha$  particle cross sections. The results were compared with previous data [2,16-20] of  ${}^6\text{Li}$  scattering on various heavier targets and found to exhibit a universal behaviour. The non-capture breakup channels of  ${}^6\text{Li}$  only explains  $\sim 25\%$  of the total  $\alpha$  and thus indicating that the  $d$ -capture as most dominant channel responsible for such high inclusive  $\alpha$  production. In addition to inclusive  $\alpha$ , the angular distribution of other products like  ${}^3\text{He}$ ,  $t$ ,  $d$  and  $p$  are measured for the same energies and it has been observed that the  $\alpha$  production cross-section is much higher than each of the other channels.

To conclude, the present thesis work has looked into the possibilities of the different of breakup channels of two weakly bound nuclei  ${}^6\text{Li}$  and  ${}^7\text{Li}$ . The role of cluster structure of the projectiles on possible breakup modes has been investigated. Several new results have been observed for the first time as mentioned above which has advanced the understanding of the field. Angular distribution of cross-section for different breakup channels were estimated and compared with the coupled channels calculations. The detailed study of resonant, direct and transfer induced breakup into two fragments via different resonant states provides a good foundation towards understanding the reaction mechanisms of total  $\alpha$  production, the sequential modes of projectile breakup and their impact on fusion cross sections.

The thesis has been organized as follows: In Chapter 1, a brief introduction to the heavy ion reactions has been given. Reaction mechanism involving weakly bound nuclei and the current status in the field has been presented along with the general motivation for the thesis work. Chapter 2 describes the general experimental techniques used for the detection of breakup fragments in coincidence along with singles measurement of elastic and inclusive particle. A brief description of the coupled channels formalism used in

the analysis has been presented in Chapter 3. Chapter 4 highlights the resonant, direct and transfer breakup of  ${}^6\text{Li}$  by  ${}^{112}\text{Sn}$  [12]. In chapter 5, the role of cluster structure in the breakup of  ${}^7\text{Li}$  has been discussed [13]. The resonant breakup of  ${}^8\text{Be}$  in  ${}^{112}\text{Sn}$  ( ${}^7\text{Li}, {}^8\text{Be} \rightarrow 2\alpha$ ) has also been described here [14]. The inclusive cross section for  $\alpha$ ,  ${}^3\text{He}$ ,  $t$ ,  $d$  and  $p$  and the production mechanisms of large inclusive  $\alpha$  yield have been presented in chapter 6 [15]. The summary of the thesis along with the future scope of the work is highlighted in Chapter 7.

## References:

- [1] Cockcroft J.D. and Walton E.T.S., Nature,129(3261), 649 (1932).
- [2] S. Santra et al., Phys. Rev. C 85, 014612 (2012).
- [3] M. Dasgupta et. al, Phys. Rev. C 66,041602(R) (2002).
- [4] P. K. Rath et. al, Phys. Rev. C 79,051601(R) (2009).
- [5] A. Shrivastava et. al, Phys. Lett. B 633,463 (2006).
- [6] S. Santra et. al, Phys. Lett. B 677,139 (2009).
- [7] D. H. Luong et. al, Phys. Lett. B 695,105 (2011).
- [8] A. Diaz-Torres et. al, Phys. Rev. C 68,044607 (2003).
- [9] K. Rusek et. al, Phys. Rev. C 85,014608 (2003).
- [10] W. Ott et. al, Nucl. Phys. A 489,329 (1988).
- [11] V. Mihailovic et. al, Nucl. Phys. A 311, 377 (1978).
- [12] D. Chattopadhyay et. al, Phys. Rev. C 94,061602(R) (2016).
- [13] D. Chattopadhyay et. al, Phys. Rev. C 97,051601(R) (2018).
- [14] D. Chattopadhyay et. al, Under review in peer reviewed journal.
- [15] D. Chattopadhyay et. al, EPJ Web of Conferences 117,06022 (2016).
- [16] K. O. Pfeiffer et. al, Nucl. Phys. A 206,545 (1973).
- [17] A. Pakao et. al, Phys. Rev. Lett. 90,202701 (2003).
- [18] F. Souza et. al, Nucl. Phys. A 821,36 (2009).
- [19] H. Kumawat et. al, Phys. Rev. C 81,054601 (2010).

[20]C. Signorini et. al, Eur. Phys. J. A 10,249 (2001).

# List of Figures

1.1	The Segre chart. . . . .	2
1.2	Dominant cluster structure of weakly bound nuclei. . . . .	5
1.3	Schematic representation of Borromean structure of ${}^6\text{He}$ [11]. . . . .	6
1.4	Density distribution of ${}^{11}\text{Li}$ nucleus [12]. . . . .	7
1.5	Comparison of the size of the ${}^{11}\text{Li}$ and its two neutron-halo with stable nuclei [15]. . . . .	8
1.6	Comparison of RMS radii of Li isotopes [16]. . . . .	8
1.7	Variation of Super-heavy production cross-section with element number [17].	10
1.8	Schematic of soft dipole resonance(SDR) and giant dipole resonance(GDR) modes of halo nuclei [19]. . . . .	11
1.9	Various breakup reaction processes in ${}^6\text{Li}+{}^{112}\text{Sn}$ system. . . . .	15
2.1	Layout of the Pelletron-LINAC accelerator facility at TIFR, Mumbai, India [30]. . . . .	23
2.2	The typical configuration of a silicon surface barrier detector. . . . .	26
2.3	The front side of a typical Micron-make W1-type silicon strip detector. . .	27
2.4	The schematic diagram of the experimental setup showing strip detector array, single telescopes and monitors inside the scattering chamber. . . . .	27
2.5	The photograph of double-sided silicon strip detector array along with surface barrier telescopes at BARC-TIFR Pelletron-LINAC facility, Mumbai, India. . . . .	28

2.6	Block diagram of the electronics for the measurement of breakup fragments.	31
2.7	Typical two-dimensional ( $\Delta E$ versus $E_{\text{total}}$ ) energy-calibrated spectrum acquired in one of the vertical strips at $\theta = 70^\circ$ for a beam energy of 30 MeV. The inset shows the total coverage in $\theta$ and $\phi$ by the strip detector array, and the intensity represents the number of $\alpha$ particles detected in coincidence with $t$ , $d$ , or $p$ in any two vertical strips.	32
2.8	Schematic of co-ordinate transformation.	33
2.9	Velocity diagram displaying the laboratory and center-of-mass frames for decay of projectile-like fragment [37].	36
2.10	The flow chart for the simulation of 3-body kinematics using Monte Carlo technique.	37
3.1	Jacobi-Coordinate used in CDCC method.	51
4.1	Comparison of the yield distributions of $\alpha - d$ , $\alpha - p$ , and $\alpha - \alpha$ breakup as a function of relative energy at two different beam energies, i.e., 22 and 30 MeV.	57
4.2	Sequential $\alpha + d$ breakup cross section in center-of-mass frame measured at 30 MeV.	62
4.3	Differential cross sections for direct breakup of ${}^6\text{Li} \rightarrow \alpha + d$ in center-of-mass frame measured at $E_{\text{beam}}$ of (a) 30 MeV and (b) 22 MeV. Corresponding experimental elastic scattering angular distribution (diamonds) along with the results of CDCC calculations (dash-dot-dotted lines) are shown in (c) and (d).	64
4.4	Differential cross sections in center-of-mass frame for sequential breakup of (a) ${}^6\text{Li} \rightarrow {}^5\text{Li} \rightarrow \alpha + p$ , and (b) ${}^6\text{Li} \rightarrow {}^8\text{Be} \rightarrow \alpha + \alpha$ measured at $E_{\text{beam}} = 30$ MeV and 22 MeV. Lines represent CRC calculations.	67

5.1	(a) Relative energy distribution without efficiency correction, (b) efficiency of the detector array and (c) efficiency corrected relative energy distribution corresponding to $\alpha + t$ breakup. . . . .	74
5.2	(a) Relative energy distribution without efficiency correction, (b) efficiency of the detector array and (c) efficiency corrected relative energy distribution corresponding to $\alpha + \alpha$ breakup. . . . .	75
5.3	Efficiency corrected relative energy distributions corresponding to (a) $\alpha + d$ breakup, (b) $\alpha + p$ breakup and (c) ${}^6\text{He} + p$ breakup respectively. The relative energy bin size in the histogram (c) is 0.1 MeV which is double of that in (a) and (b). . . . .	78
5.4	Two dimensional plot of $E_{\text{rel}}$ versus $Q$ -value for $\alpha + p$ , $\alpha + t$ and ${}^6\text{He} + p$ breakup reactions showing the distribution of events with different projectile-like and target-like excitations. . . . .	79
5.5	Same as Fig. 5.4 but for $\alpha + \alpha$ breakup. . . . .	80
5.6	Same as Fig. 5.4 but for $\alpha + d$ breakup. . . . .	80
5.7	Differential cross sections for (a,b) sequential breakup of ${}^7\text{Li} \rightarrow \alpha + t$ for its $7/2^-$ and $5/2^-$ resonance states respectively, (c) direct breakup of ${}^7\text{Li} \rightarrow \alpha + t$ and (d) direct breakup of ${}^7\text{Li} \rightarrow {}^6\text{He} + p$ . The lines represent the results of CDCC calculations. . . . .	85
5.8	Differential cross sections for (a) sequential breakup of ${}^7\text{Li} \xrightarrow{-2n} {}^5\text{Li} \rightarrow \alpha + p$ and (b-d) sequential breakup of ${}^7\text{Li} \xrightarrow{-1n} {}^6\text{Li} \rightarrow \alpha + d$ through $3^+$ , $2^+$ and $1^+$ resonance states of ${}^6\text{Li}$ respectively. Solid lines represent the results of CRC calculations. . . . .	87

5.9	Differential cross sections in center-of-mass frame for sequential breakup of ${}^7\text{Li}\rightarrow{}^8\text{Be}\rightarrow\alpha + \alpha$ corresponding to (a) $0^+$ , (b) $2^+$ and (c) $4^+$ states of ${}^8\text{Be}$ along with (d) the elastic scattering, measured at $E_{\text{beam}} = 30$ MeV. The hollow circles in (a), (b) and (c) represent $2\alpha$ breakup cross sections corresponding to no target excitation, whereas, the filled circles represent total breakup cross sections corresponding to both ground state as well as excited states of the target like nuclei. Lines represent the results of the CRC calculations using FRESKO. Dashed lines represent theoretical cross sections only for g.s. to g.s. transition and solid lines represent total cross sections for g.s. and excited states of ${}^{111}\text{In}$ . . . . .	89
5.10	Experimental and theoretical cross sections for sequential breakup of ${}^7\text{Li}\rightarrow{}^8\text{Be}\rightarrow\alpha + \alpha$ corresponding to (a) $0^+$ , (b) $2^+$ and (c) $4^+$ states of ${}^8\text{Be}$ corresponding to no target excitation. Dashed and solid lines represent the results of FRESKO calculations using ‘CRC only’ and ‘CDCC+CRC’ formalisms respectively. . . . .	91
5.11	Experimental cross sections for 1p stripping corresponding to g.s. of ${}^6\text{He}$ and (a) g.s., (b) 1st excited state and (c) 2nd excited state of ${}^{113}\text{Sb}$ . Solid lines represent FRESKO calculations using ‘CDCC+CRC’ formalism. . . . .	94
5.12	Experimental cross sections for 1n stripping corresponding to g.s. of ${}^6\text{Li}$ and (a) g.s. and (b) 0.738 MeV excited state of ${}^{113}\text{Sn}$ . Solid lines represent FRESKO calculations using ‘CDCC+CRC’ formalism. . . . .	95
5.13	Measured (circles) elastic scattering cross sections have been compared with the FRESKO calculations (lines) showing the effect of coupling of direct and resonant breakup and transfer channels. . . . .	98

5.14	The variation of coincidence events of $\alpha - \alpha$ with respect to $ E_1 - E_2 $ versus $E_{rel}$ . The curved lines represent maximum allowed energy difference $ E_1 - E_2 $ as a function of relative energy (see text for details). Inset shows the intensity distribution of $0^+$ state in the range of $ E_1 - E_2  = 0$ to the maximum allowed $ E_1 - E_2 ^{max} \sim 3.4$ MeV. . . . .	100
5.15	Diagram of orientation of fragment velocities. . . . .	102
5.16	Experimental $\beta$ versus $\theta_{12}$ distribution for the breakup of ${}^8\text{Be}$ into $2\alpha$ . The lines represent theoretical correlations assuming $E_1 = E_2$ . . . . .	103
5.17	A Monte-Carlo simulation on $\beta$ versus $\theta_{12}$ distribution for the breakup of ${}^8\text{Be}$ into $2\alpha$ assuming asymptotic breakup for the ${}^7\text{Li}+{}^{112}\text{Sn}$ reaction, corresponding to the present detector setup. . . . .	104
5.18	A comparison of simulation with experimental $\beta$ distribution corresponding to $0^+$ , $2^+$ and $4^+$ events. . . . .	105
6.1	Experimental differential cross sections for (a) elastic scattering and (b, c) inelastic scattering corresponding to ( $2^+$ , 1.256 MeV) and ( $3^-$ , 2.35 MeV) excited states of ${}^{112}\text{Sn}$ respectively. Solid lines correspond to the results of coupled-channels calculations using FRESKO. . . . .	110
6.2	A typical two-dimensional raw spectrum of a telescope placed at $105^\circ$ and $E_{beam} = 30$ MeV. . . . .	111
6.3	Inclusive $\alpha$ spectra at $\theta \sim \theta_{gr}$ for different bombarding energies. . . . .	113
6.4	Inclusive $\alpha$ angular distribution for ${}^6\text{Li}+{}^{112}\text{Sn}$ at energies $E_{lab} = 22-30$ MeV. Lines are $\chi^2$ minimized fit to the data and used to obtain the angle integrated cross sections. . . . .	114
6.5	Inclusive $\alpha$ (circles, present data) and $\alpha$ contributions from different transfer and breakup channels for different beam energies. . . . .	115
6.6	The individual contribution of different breakup channels leading to inclusive $\alpha$ for 30 MeV beam energy. . . . .	116

6.7	Inclusive breakup $\alpha$ cross sections involving ${}^6\text{Li}$ projectile with several different targets including ${}^{112}\text{Sn}$ (present data) as a function of reduced energy.	118
6.8	Variation of ' $\sigma^{react.}-\sigma_{\alpha}^{inc.}$ ' with normalized energy ' $E_{c.m.}/[Z_p Z_t/(A_p^{1/3} + A_t^{1/3})]$ ', for ${}^6\text{Li}+{}^{209}\text{Bi}$ , ${}^6\text{Li}+{}^{90}\text{Zr}$ and ${}^6\text{Li}+{}^{59}\text{Co}$ are represented by red, blue and green hollow circles respectively. The filled circles with same colour represents the CF cross-section for the respective system at that normalized energy.	119
6.9	Inclusive (a) ${}^3\text{He}$ , (b) $t$ , (c) $d$ and (d) $p$ cross-sections at energies $E_{\text{beam}}=22-30$ MeV.	121

# List of Tables

1.1	Breakup threshold of the Borromean structure of some of the weakly bound nuclei. . . . .	6
4.1	Experimental and calculated cross sections for various channels at $E_{beam} = 30$ and 22 MeV. . . . .	68
5.1	Comparison of the observed energies and widths of the resonance peaks in relative energy distributions with the ones available from the literature [24, 59]. . . . .	76
5.2	The states of the projectile ${}^7\text{Li}$ included in the model space of the CDCC calculations. $E_x$ , $E_{min}$ and $E_{max}$ respectively represent the mean, minimum and maximum excitation energies of a particular bin state above the $\alpha$ - $t$ breakup threshold. . . . .	83
5.3	Structure information and spectroscopic amplitudes for the overlaps $A = C + x$ corresponding to different states of the nuclei $A$ , $C$ and $x$ used in the CRC calculations for ( ${}^7\text{Li}, {}^8\text{Be}$ ) reaction. . . . .	96
5.4	Structure information and spectroscopic amplitudes for the overlaps $A = C + x$ corresponding to different states of the nuclei $A$ , $C$ and $x$ used in the CRC calculations for ( ${}^7\text{Li}, {}^6\text{Li}$ ) and ( ${}^7\text{Li}, {}^6\text{He}$ ) reactions. . . . .	97
6.1	Calculated cross-sections for various channels producing $\alpha$ at $E_{beam} = 22$ – $30$ MeV. . . . .	116

6.2	Experimental integrated cross-sections for ${}^3\text{He}$ , $t$ , $d$ and $p$ at $E_{beam} =$ 22–30 MeV. . . . .	122
-----	--	-----

# Chapter 1

## Introduction

Towards the cessation of the 19<sup>th</sup> century, after a few amazing discoveries, many scientists thought that no new advances in physics remained to be made. Yet within ten years Henri Becquerel, Pierre and Marie Curie and additionally Ernest Rutherford discovered an entirely new window of physics called radioactivity. In 1911, the well-known gold-foil experiment carried out by Rutherford and his group laid the foundation of nuclear physics. Later the discovery of neutron by Chadwick confirmed the composition of nucleus as a combination of proton and neutron. With the motivation to extract the information related to the size, shape, lifetimes etc. of nucleus, first artificial nuclear reaction involving accelerated beam of projectiles with stationary target was built by Cockcroft and Walton in 1932 [1]. Advancement in building new accelerators which could efficiently accelerate these heavy ions ( $A > 4$ ) was initiated by Alvarez in 1940, where he produced 50 MeV  $^{12}\text{C}^{6+}$  ions [2]. By 1950, with the go for creating new transuranic elements, one of the first results of heavy ion reactions were obtained with  $^{12}\text{C}$  and  $^{13}\text{C}$  beams of energies around  $\sim 110$ - $120$  MeV, that were bombarded onto Al and Au to produce  $^{34}\text{Cl}$  and  $^{205}\text{At}$  [3]. Since then a new branch of nuclear reactions induced by heavy ions emerged with the aim of producing elements heavier than those occurring naturally. After the invention of such artificial accelerators the production of nuclei by fusion became possible and as a result nuclear landscape has widened substantially. So to look for the origin of matter one has

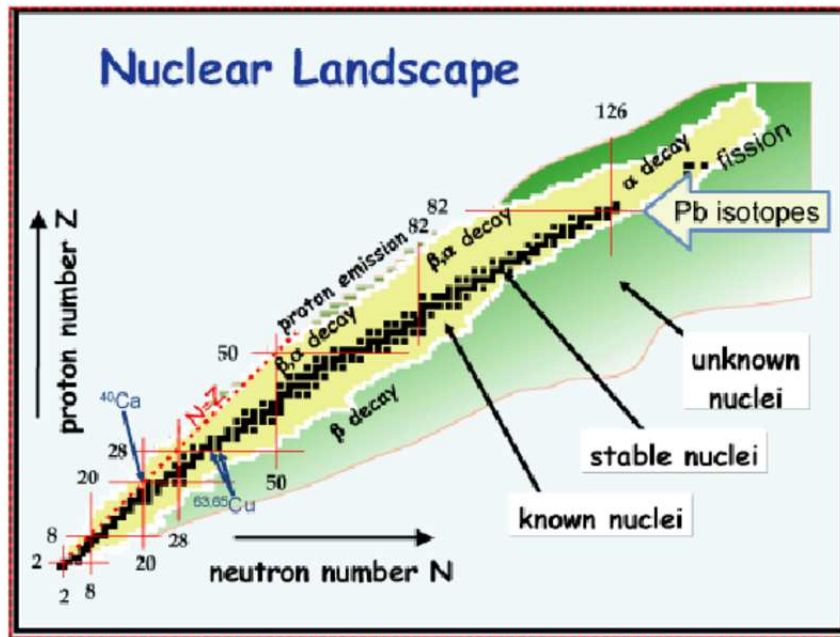


Figure 1.1 The Segre chart.

to depend on the studies of the nuclear fusion reactions. However, only a few nuclei are found to be stable (around 300). Fig. 1.1 represents the plot of the neutron number( $N$ ) versus proton number( $Z$ ) known as Segre Chart distinguishes the stable nuclei from the unstable ones that spread on both sides of the stability line. If we go farther away from the stability line, nuclei become more unstable and instability reaches to a point, where the nuclei can no longer hold any more neutron(neutron drip-line) or proton(proton drip-line). To grasp the total region of the Segre Chart, the entire data of stable and unstable nuclei is needed. Lots of studies have been done near the stability line, but the knowledge of nuclei far away from the stability line is insufficient, because those nuclei have very short lifetime being radioactive. The properties of these nuclei also influence the results of explosive astrophysical events such as supernovae. However, direct measurement of structural properties of these nuclei is not possible because of their short life times and limited availability. So, one should search for the indirect ways so as to get the structural data of those rare exotic nuclei. The weakly bound stable projectiles, like  ${}^6,7\text{Li}$  and  ${}^9\text{Be}$ ,

show somewhat similar behaviour (such as low breakup threshold, core+valence cluster structure, etc.) as that of the exotic nuclei. Also, the projectile dissociation of weakly bound nuclei serves as an input to the determination of radiative capture cross section of astrophysical interest. In the absence of nuclear or higher order Coulomb effects on the reaction, the astrophysical S factor can be extracted from the Coulomb dissociation cross-section for low relative energies. The information of astrophysical S-factor provides an input to the determination of reaction rate of various nucleosynthesis processes in stellar burning astrophysical sites. Therefore, by studying the reaction mechanism involving  ${}^6,7\text{Li}$  and  ${}^9\text{Be}$  nuclei, which are available easily and abundantly from the stable beam accelerators, one can predict a number of fascinating properties of the weakly bound exotic nuclei and understand the elemental abundances of various stars. Attempts have been made to understand the breakup mechanism of weakly bound nuclei  ${}^6,7\text{Li}$ ,  ${}^9\text{Be}$  but it is far from being fully understood [4–9]. The present thesis work is in fact fully dedicated to the detailed investigation of breakup reaction mechanism of  ${}^6,7\text{Li}$  projectile nuclei on medium mass target  ${}^{112}\text{Sn}$ .

As, the weakly bound nuclei such as  ${}^6,7\text{Li}$  and  ${}^9\text{Be}$ , have a low breakup threshold, the population of low lying continuum is probable and expected to give a large coupling effect at energies around the Coulomb barrier. As a consequence, the weakly bound stable and unstable nuclei exhibit remarkably different features with respect to the tightly bound ones.

## 1.1 Interesting features involving weakly bound nuclei

A number of unusual characteristics of weakly bound nuclei have already been discovered, such as unusually large radii with some of the valence nucleon(s) forming a halo structure. For some of the weakly bound nuclei, the mean-field approximations are no

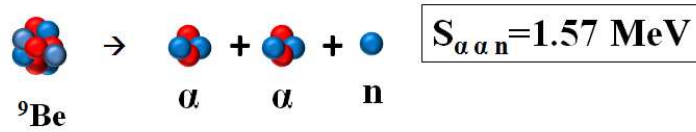
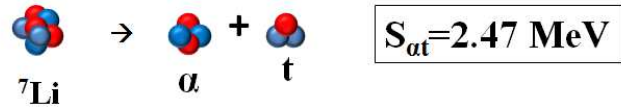
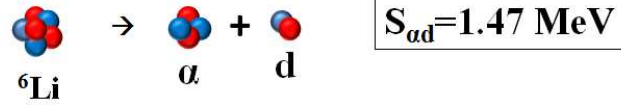
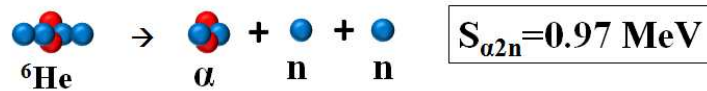
longer be useful instead the three-body cluster models appear to be much more promising. One of the fascinating aspects of the weakly bound nuclei is the possibility of studying nuclei near the neutron drip line. The weakly bound nuclei like  ${}^6\text{He}$ ,  ${}^{11}\text{Li}$  etc. also exhibit two-neutron halo “Borromean” type of structure, where three separate parts of the nucleus are bound together in such a way that if any one is removed, the remaining two become unbound. These properties are interlinked to other characteristic features such as low binding energy, large radius and extended density distribution, core-halo oscillation, extended  $B(E_1)$  strength over excitation energies etc.. Because of so many interesting features of the weakly bound nuclei as described above, the nuclear physics studies involving weakly bound nuclei has been drawing a lot of attention in recent years. The detailed understanding of these features will be useful to understand the low energy capture cross-sections of astrophysical relevance and to simulate the synthesis of super-heavy element by fusion of nuclei near drip line.

Some of the interesting features of weakly bound nuclei are discussed briefly in the following subsections.

### 1.1.1 Cluster structure

Clustering is a general phenomenon widely observed in everyday aspects such as the gathering of galaxies in the universe or in complex biological system. In nuclear physics, the term ‘cluster’ refers to the organization of protons and neutrons in the atomic nucleus e.g. the  $\alpha$  particle consisting of two protons and two neutrons forming the ‘ $\alpha$ -cluster’. The  $\alpha$ -cluster structure has been observed in case of tightly bound nuclei e.g.,  ${}^{12}\text{C}$ ,  ${}^{16}\text{O}$ ,  ${}^{20}\text{Ne}$ , etc.

Cluster models of the structure of weakly bound nuclei frequently provide a rather simple description of some of the energy levels which are difficult to access in the usual shell-model framework. Weakly bound nuclei, such as  ${}^6\text{He}$ ,  ${}^{6,7}\text{Li}$ ,  ${}^9\text{Be}$  have predominant  $\alpha + x$  cluster structure with low breakup threshold as shown in Fig. 1.2. Apart from the

**Stable ions:****Unstable ions:****Figure 1.2** Dominant cluster structure of weakly bound nuclei.

well-known  $\alpha + x$  cluster,  ${}^6\text{Li}$ ,  ${}^7\text{Li}$  also exhibit some additional cluster structures, such as  ${}^6\text{Li}$  exhibits  ${}^3\text{He} + \text{t}$  with breakup threshold  $\sim 16$  MeV and  ${}^7\text{Li}$  shows  ${}^6\text{Li} + \text{n}$  and  ${}^6\text{He} + \text{p}$  structures with breakup threshold 7.25 and 9.97 MeV respectively.

**1.1.2 Borromean structure**

The weakly bound nuclei such as  ${}^6\text{He}$ ,  ${}^{11}\text{Li}$ ,  ${}^9\text{Be}$ , etc. with three body clusters exhibit an important characteristics, where the three separate parts of the nucleus are bound together in such a way that if any one is removed, the remaining two become unbound. This structure is known as “Borromean”, originated from the Borromean Rings consist of three topological circles which are interlinked [10]. The lightest Borromean nucleus is  ${}^6\text{He}$  with  $\alpha + \text{n} + \text{n}$  cluster structure with very short half-lives ( $\sim 807$  ms). The possible combination using any two among  $\alpha$ ,  $\text{n}$  and  $\text{n}$  are  ${}^5\text{He}$  and dineutron ( $\text{n}-\text{n}$ ), both are unstable. After  $\sim 807$  ms  ${}^6\text{He}$  is converted to  ${}^6\text{Li}$  via  $\beta^-$  decay process. If one consider

${}^6\text{Li}$  as a superposition of  $\alpha$ , p and n, then the possible combination of forming the binary subsystems using them are  ${}^5\text{Li}(\alpha+p)$ ,  ${}^5\text{He}(\alpha+n)$  and deuteron(p-n). Though  ${}^5\text{Li}$  and  ${}^5\text{He}$  are unstable, but deuteron is weakly bound stable nucleus, hence the Borromean structure does not exist in  ${}^6\text{Li}$ . The nucleus  ${}^9\text{Be}$  is the lightest stable nuclei with  $\alpha+\alpha+n$  Borromean structure. Similarly,  ${}^{11}\text{Li}({}^9\text{Li}+n+n)$  and  ${}^8\text{He}({}^6\text{He}+n+n)$ , which are radioactive, also have the Borromean structure.  ${}^{22}\text{C}$ , another radio-active element, is the latest and heaviest known Borromean nucleus with cluster structure  ${}^{20}\text{C}+n+n$  having breakup threshold of  $\sim 0.035$  MeV. The breakup threshold of some of the weakly bound nuclei with Borromean structure are shown in Table 1.1

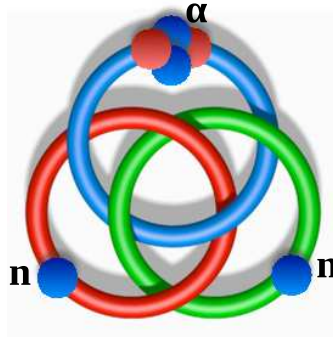


**Figure 1.3** Schematic representation of Borromean structure of  ${}^6\text{He}$  [11].

**Table 1.1** Breakup threshold of the Borromean structure of some of the weakly bound nuclei.

Nuclei	Borromean structure	Breakup threshold $E_{th}$ (MeV)
${}^6\text{He}$	$\alpha+n+n$	0.98
${}^9\text{Be}$	$\alpha+\alpha+n$	1.57
${}^{11}\text{Li}$	${}^9\text{Li}+n+n$	0.37
${}^8\text{He}$	${}^6\text{He}+n+n$	2.13
${}^{14}\text{Be}$	${}^{12}\text{Be}+n+n$	1.27
${}^{17}\text{B}$	${}^{15}\text{B}+n+n$	1.39
${}^{19}\text{B}$	${}^{17}\text{B}+n+n$	0.09

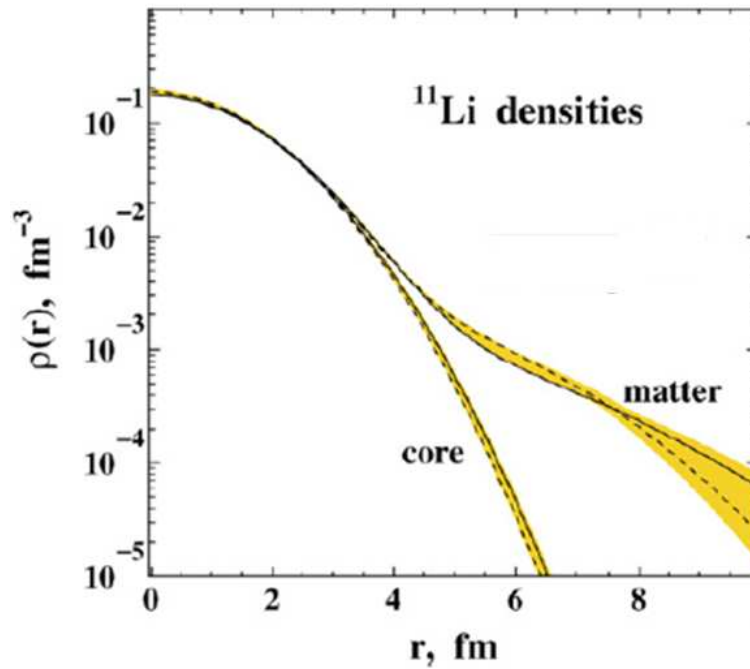
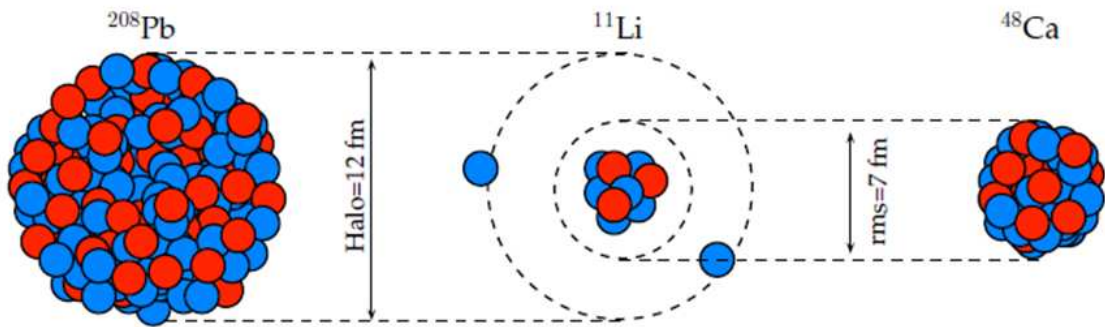


Figure 1.4 Density distribution of  $^{11}\text{Li}$  nucleus [12].

### 1.1.3 Extended density distribution

The drip-line nuclei are weakly bound in nature and exhibit core+valence(neutron(s) or proton(s)) structure. Though the measured charge and matter radii of stable nuclei are nearly equal and has the  $1.2A^{1/3}$  dependence, the scenario is different for loosely bound halo nuclei. As the halo nucleon(s) is(are) situated at a larger distance (distances) from the core, the radii of those nuclei are appreciably larger than  $1.2A^{1/3}$  values. This suggests the existence of large deformation along with a long tail in the matter distribution as shown in Fig. 1.4. One example of a halo nucleus is  $^{11}\text{Li}$ , which has a half-life of 8.6 ms. It contains a core of 3 protons and 6 neutrons, and a halo of two independent and loosely bound neutrons. It decays into  $^{11}\text{Be}$  by the emission of an anti-neutrino and an electron. The RMS matter radius of  $^{11}\text{Li}$  is as that of  $^{48}\text{Ca}$ , and the radius of the halo neutrons as large as for the outermost neutrons in  $^{208}\text{Pb}$  [13, 14]. The comparison of the size of the  $^{11}\text{Li}$  with them is shown in Fig. 1.5.



**Figure 1.5** Comparison of the size of the  $^{11}\text{Li}$  and its two neutron-halo with stable nuclei [15].

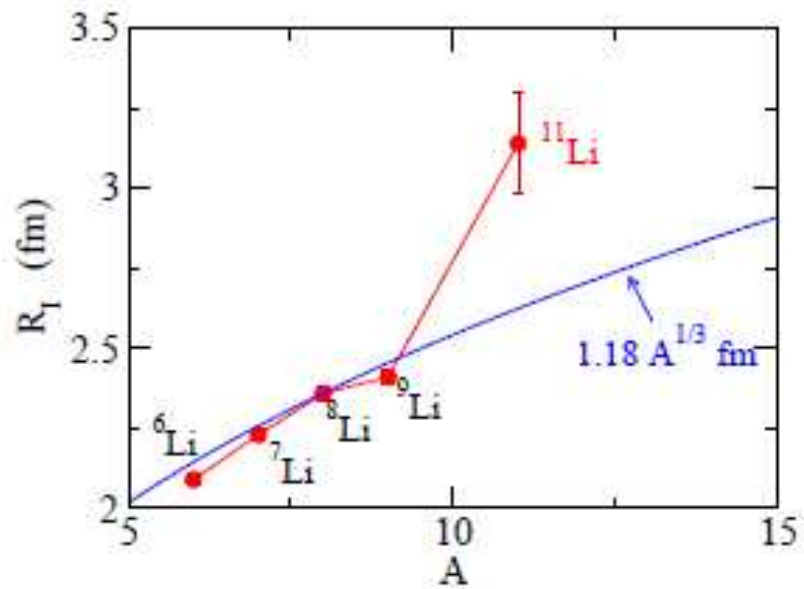


**Figure 1.6** Comparison of RMS radii of Li isotopes [16].

The interaction cross-section at very high energy can be written as:

$$\sigma_I = \pi (R_p + R_t)^2 \quad (1.1)$$

where,  $R_p$  and  $R_t$  denotes the radius of the projectile and target respectively. If halo nucleus is used as projectile, the  $R_p$  would be comparatively larger. Hence, the interaction cross-section would be enhanced as expected from the equation 1.1. The comparison of the RMS radii of Li isotopes shown in Fig. 1.6 reveals the halo characteristic nature of  $^{11}\text{Li}$ .

#### 1.1.4 Synthesis of super-heavy element

Uranium with proton number  $Z=92$  is the heaviest unstable element found in nature. All elements with proton numbers larger than that Uranium have to be produced artificially through nuclear reactions. While elements up to  $Z=100$  can be reached via neutron capture process with subsequent  $\beta$ -decays. The elements with  $Z>100$  are created via the heavy-ion induced nuclear fusion reactions. But with the increase in proton number, the Coulomb repulsion between the projectile and target increases, consequently the production cross-section of super-heavy elements goes down. The production cross-section of super-heavy element with element number is shown in Fig. 1.7. Instead, if one uses the neutron rich isotope as projectile to form the same super-heavy element, then the production cross-section might increase. So to form the super-heavy element with higher cross-section, the high intensity neutron rich RIB (radioactive ion beam) is needed. It is estimated that around 5000 to 7000 bound nuclei should exist, out of which only 1500 nuclei are observed. New territory can be explored with next-generation rare isotope facilities. Investigating the properties of weakly bound nuclei like  $^{6,7}\text{Li}$  and  $^9\text{Be}$  will complement studies using the next generation of high-intensity isotope-separator on-line (ISOL) radioactive ion beam facilities as they show somewhat similar behaviour as that

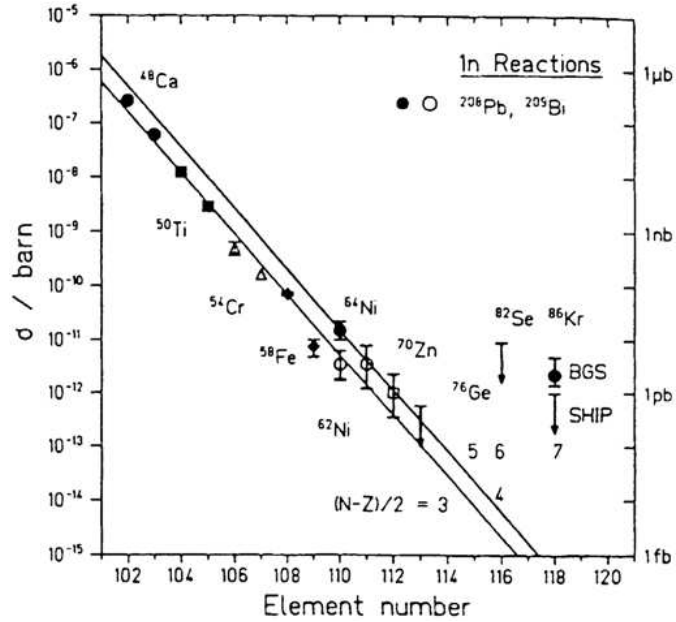


**Figure 1.7** Variation of Super-heavy production cross-section with element number [17].

of neutron-rich radioactive ion beams. Hence, the complete understanding of the breakup mechanism of weakly bound nuclei will be useful to simulate the synthesis of super-heavy element(SHE) by fusion near neutron drip line.

### 1.1.5 Soft dipole resonance

Weakly bound halo nucleus exhibits core+valence cluster structure, where the core is surrounded by the valence nucleon(s) which is(are) at large distance(distances) from the core. Consider the case of  $^{11}\text{Li}$  nucleus, which has a “Borromean” structure. Here two neutrons are weakly bound to a core, and located at large distances from it. The extended density tail of the halo might give rise to a ‘soft electric dipole mode’. Thereafter, a novel phenomenon was proposed whereby the oscillation of the halo neutrons and the core might lead to low-energy soft dipole resonance states [18].

The soft dipole resonance is a phenomenon occurring only when the nuclear surface has an appreciably large neutron-proton density difference [18]. Therefore, it is different from

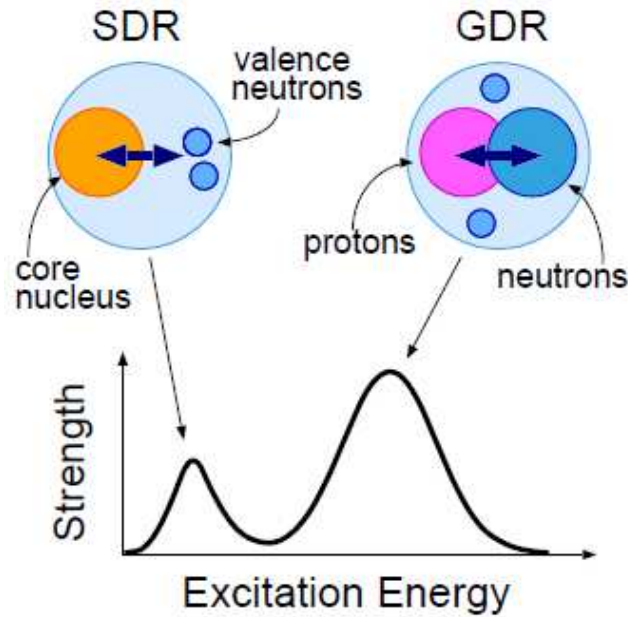


**Figure 1.8** Schematic of soft dipole resonance(SDR) and giant dipole resonance(GDR) modes of halo nuclei [19].

the standard giant dipole resonance, where protons and neutrons collectively oscillate with respect to each other. Soft dipole resonances located slightly above the neutron threshold can have impact on the neutron capture rates in r-process nucleosynthesis [18]. The excitation of soft dipole resonance is expected to be  $\sim 1$  MeV as compared to the standard giant dipole resonance where the excitation energy is  $\sim 15$ -20 MeV. The schematic of soft dipole resonance along with excitation energy curve is shown in Fig. 1.8. However, it is still debated whether the small bump like structure is caused by the soft dipole resonance or due to the complicated nuclear structure of  $^{11}\text{Li}$  [19].

### 1.1.6 Astrophysical interest

The determination of capture cross section involving charged particle reactions at very low energies is of particular importance in astrophysics. Reaction rates serve as input to various astrophysical models such as primordial nucleosynthesis or stellar evolution. Ideally cross sections are measured directly in experiments, however, in most cases a

direct measurement is very difficult or even impossible at the relevant low energies since cross sections become very small because of Coulomb repulsion of the interacting particles. Often one has to rely on the extrapolation of the cross section to low energies. Alternative methods have been proposed where the considered reaction is not studied directly but a closely related process can be measured in the laboratory.

In the case of radiative capture reactions the Coulomb dissociation method has been used successfully as an indirect method in recent years [20]. Here, the inverse reaction of radiative capture i.e. the breakup of the nucleus produced in the capture process, is studied during the scattering on a highly charged target, which supplies the necessary photons through its Coulomb field. From the dissociation cross section the astrophysical S factor of the capture reaction can be extracted with the help of nuclear reaction theory.

In view of the above discussions, it is essential to understand the breakup reactions mechanism of weakly bound nuclei in details.

## 1.2 Breakup reactions mechanism

With the condition that the impact parameter is close to the grazing distance ( $b_{gr}$ ), the breakup reactions are said to occur with typical collision time scale  $\sim 10^{-22}$  sec.. Hence, breakup reactions can be classified as direct and peripheral. If the projectile has low breakup threshold then while moving in the field of the target nucleus it may break up into its cluster constituents directly or get excited into a resonant state above the breakup threshold followed by its breakup. These two processes are known as ‘direct breakup’ and ‘resonant breakup’ respectively. For weakly bound projectile such as  ${}^6\text{Li}$ ,  ${}^7\text{Li}$  and  ${}^9\text{Be}$  the transfer reactions may sometime lead to the formation of quasi-bound state of the ejectile of very short life time resulting in its breakup into  $\alpha + x$  pair where,  $x$  is the breakup fragment complementary to  $\alpha$ . This breakup process is known as ‘transfer-triggered breakup’. Because of breakup, the projectile is splitted into two or more fragments. Therefore, the simplest two body kinematics is no longer be appropriate to predict the reaction kine-

matics involving breakup reaction, rather one need to understand at-least the three body kinematics. If we assume the binary breakup of projectile, then the total reaction Q-value for each breakup event can be obtained by using the following relation [9]:

$$Q = E_1 + E_2 + E_{loss} + E_{recoil} - E_{beam} \quad (1.2)$$

where,  $E_1$  and  $E_2$  are the laboratory energies of the two breakup fragments,  $E_{beam}$  is the beam energy,  $E_{loss}$  is the energy loss in the target calculated at half-thickness and  $E_{recoil}$  is the recoil energy of the residual target nucleus in the laboratory frame. If the reconstructed Q-value is found to be less as compared to the  $Q_{gg}$  during breakup process, then the reduction in  $Q_{gg}$  will provide the information regarding the excitation energy associated with the target like nucleus.

In order to get the information of excitation energy of the intermediate projectile-like fragment through which the breakup occurs one need to reconstruct the kinematical quantity, named ‘relative energy’. The relative energy between the two breakup fragments will depend on the fragment mass, kinetic energy and relative angular separation between them. Mathematically this quantity is expressed as [21]:

$$E_{rel} = \frac{m_2 E_1 + m_1 E_2 - 2\sqrt{m_1 m_2 E_1 E_2} \cos\theta_{12}}{m_1 + m_2} \quad (1.3)$$

The experimental two dimensional event by event plot of  $E_{rel}$  versus Q-value highlights the excitations of target like fragment associated with the excitations of projectile-like fragment through which the breakup occurs.

### 1.2.1 Direct breakup

Direct breakup of nucleus is a reaction process where the projectile splits into its constituent fragments. This breakup occurs directly from the free continuum states i.e. it is one-step process. Both the Coulomb and nuclear fields experienced by the projectile in

the vicinity of the target are responsible for this process. Direct breakup may occur prior to reaching the fusion barrier. In such cases only the Coulomb interaction between the projectile and target is responsible as the nuclear interaction is short ranged. Breakup of projectiles induced by the differential Coulomb field of heavy nuclei are of considerable interest since they provide valuable informations regarding the electromagnetically induced interactions of the projectile constituents. Coulomb breakup processes also provide interesting possibilities for studies of astrophysical aspects. If none of the breakup fragments produced from the direct breakup process gets captured by the target, then the process is called as ‘non-capture direct breakup process’. During this breakup process, if the target remains in the ground state, then such non-capture breakup process is referred as ‘elastic breakup’. The typical time scale of the breakup process is  $\sim 10^{-22}$  sec, hence sometimes the direct breakup process is also referred as prompt breakup process. The schematic of direct non-capture breakup process is illustrated in panel (a) of Fig. 1.9, where the projectile  ${}^6\text{Li}$  breaks into fragments  $\alpha$  and  $d$  in the field of the target and none of the fragments are captured by the target.

## 1.2.2 Sequential breakup

Sequential breakup is basically two-step process, where the projectile is first in-elastically excited to its one of the resonant states having finite width or exchange nucleon(s) with the target before decaying into respective two or more fragments. The former process is known as ‘resonant breakup’ and the latter one is referred to as ‘transfer breakup’.

### 1.2.2.1 Resonant breakup

The life-time of the ‘resonant breakup’ process depends on the life-time of the resonant state. Hence, the resonant breakup process is slow process as compared to the direct one. The life-time of the resonant state decides the location of the breakup. If the resonant state through which the breakup occurs is narrower, then the mean life-time of that

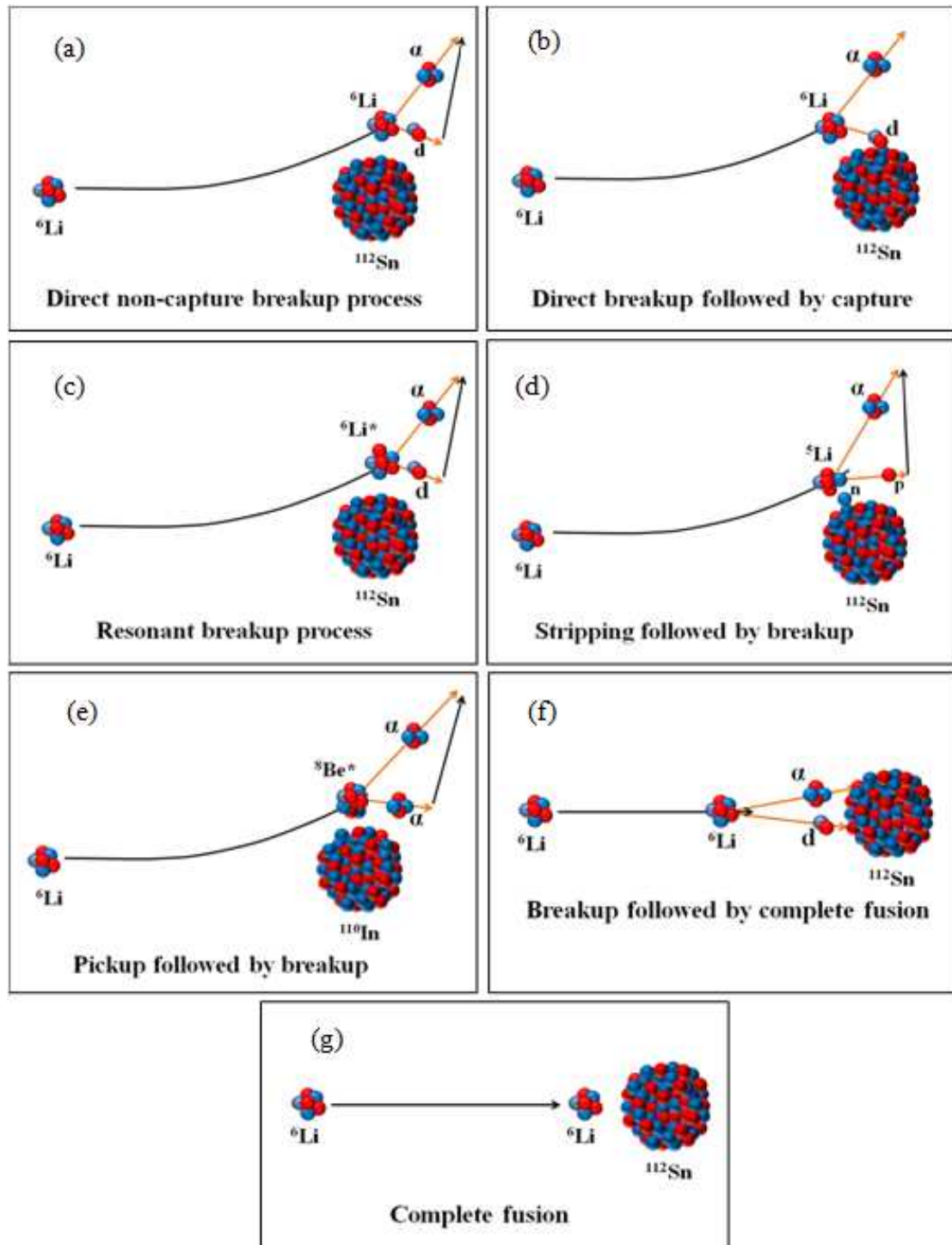


Figure 1.9 Various breakup reaction processes in  ${}^6\text{Li}+{}^{112}\text{Sn}$  system.

state would be relatively longer, that suggests that the breakup will occur far away while receding from the target. Hence, the breakup from that state has no role on incoming flux loss but the coupling of that channel may affect the elastic scattering as well as fusion cross-sections. The panel (c) of Fig. 1.9 represents the resonant breakup of  ${}^6\text{Li}$  into its cluster constituents  $\alpha$  and  $d$ .

### 1.2.2.2 Transfer breakup

Transfer-triggered breakup is a two-step peripheral collision process, the projectile must transfer a few nucleon to or from the target, leaving the projectile-like fragment in an unbound state which results into the breakup into its constituent fragments. These processes are respectively known as ‘stripping-followed by breakup’ and ‘pick-up followed by breakup’ as shown in panels (d) and (e) of Fig. 1.9 respectively. The probability of transfer-triggered breakup depends on the transfer probability which again depends on the structure of both the projectile and the target. After transfer of nucleon(s), if the projectile-like fragment produced is of quasi-bound type, then it will immediately break into its constituent fragments. In-fact, some of the quasi-bound nuclei may also exhibit resonant structure. If the transfer product is stable but of weakly bound in nature, then the breakup of that projectile-like fragment will still occur if it is formed with excitation energy above the breakup threshold. Hence, along with direct and resonant breakup, transfer-induced breakup is equally important for weakly bound projectiles ( ${}^6\text{Li}$ ,  ${}^7\text{Li}$  and  ${}^9\text{Be}$ ) to understand different modes of projectile breakup and their consequences on  $\alpha$ -particle production, fusion cross sections, and other observables. In addition to understanding the breakup reaction mechanism, the cross sections for the individual transfer-induced breakup channels provide correct coupling strengths required for realistic coupled-channels calculations to find their effects on elastic as well as fusion cross sections.

### 1.2.3 Fragment capture or Incomplete fusion

Another dominant reaction mode is the partial capture of the projectile by the target, known as ‘incomplete fusion’. It occurs when the breakup of the projectile occurs prior to the distance of closest approach  $d = \frac{Z_p Z_t e^2}{2E_{c.m.}} \left[ 1 + \frac{1}{\sin^4 \left( \frac{\theta_{c.m.}}{2} \right)} \right]$  [22] resulting into the possibility of capture of one of the fragments by the target. The breakup location plays a crucial role while understanding the phenomenon of incomplete fusion. The partial capture of the one-of-the cluster fragment of projectile may also be originated from the direct transfer of the cluster fragment to the target. It is very difficult to separate out the contributions of breakup followed by capture from the direct transfer of cluster fragment from projectile to target leading to incomplete fusion. If the breakup occurs asymptotically far away while receding from the target then it has no role on incomplete fusion, however if it occurs close to the target then it may have a role to play on incomplete fusion. In addition to the direct and resonant breakup, near target transfer-triggered breakup also plays an important role in deciding the total incomplete fusion cross section. The breakup followed by capture of one the fragment is schematically represented in panel (b) of Fig. 1.9.

### 1.2.4 Complete fusion

Complete fusion occurs at small impact parameter  $b \ll b_{gr}$ . Here, whole of the projectile is captured by the target forming the compound nucleus (with the attainment of the complete thermodynamic equilibrium), which is hot. This compound nucleus then deexcite either by fission or by particle evaporation leaving the evaporation residue. The typical life-time of compound nucleus  $\sim 10^{-16}$  sec. It may also happen that, after breakup both the fragments may get captured by the target and this process is known as breakup followed by complete fusion. It is very difficult experimentally to disentangle the process so called breakup followed by complete fusion from the normal complete fusion process. The panels (f) and (g) of Fig. 1.9 represent the breakup followed by complete fusion and pure

complete fusion processes respectively.

### 1.3 General Motivation of the thesis

In light of the above discussions, this thesis has several key motivations:

**I.** As already discussed that apart from the direct breakup, transfer breakup also has its own importance. Now, it will be of our interest to investigate which of the above breakup processes are dominant in reactions involving  ${}^{6,7}\text{Li}$  as projectile i.e. whether the majority of the breakup comes through one step process or multi-step processes. Luong *et al.* have observed a few prominent breakup channels for  ${}^{6,7}\text{Li}+{}^{207,208}\text{Pb}, {}^{209}\text{Bi}$  reactions and  ${}^7\text{Li}+{}^{144}\text{Sm}$  reactions at sub barrier energies [4]. Different breakup modes of  ${}^{6,7}\text{Li}$  were identified through the relative energy [21] distributions. They have found that breakup of  ${}^6\text{Li}$  into  $\alpha + p$  is greater than the breakup into  $\alpha + d$  for all the targets, though the 1n stripping Q-Value is different for different target. It was also observed that 1p pickup by  ${}^7\text{Li}$  followed by the breakup into  $\alpha + \alpha$  is the most preferred breakup mode for all the systems. For  ${}^7\text{Li}+{}^{144}\text{Sm}$ , breakup triggered by 2n stripping was also found to be dominant. However, Santra *et al.* [5] have observed the dominance of resonant breakup of  ${}^6\text{Li}$  into  $\alpha + d$  via its  $3^+$  state over the transfer triggered breakup by 1n stripping. For  ${}^7\text{Li}+{}^{65}\text{Cu}$ , Shrivastava *et al.* [6] found the dominance of breakup triggered by 1n stripping. So to investigate whether, the breakup phenomenon is dependent on target properties or not, the breakup reaction mechanism of  ${}^{6,7}\text{Li}$  is further probed with a medium mass target  ${}^{112}\text{Sn}$  for the present thesis work. To find the energy dependence of various breakup modes if any, the measurements for  ${}^6\text{Li}+{}^{112}\text{Sn}$  were carried out at two energies, one at above barrier and another at sub barrier energy.

**II.** Several studies show that the breakup of  ${}^6\text{Li}$  into  $\alpha + d$  occurs predominantly via its resonance states with  $L=2$  [23, 24]. Since the g.s. of  ${}^6\text{Li}$  is  $1^+$ , it can have three resonance states with  $L=2$ , i.e,  $3^+$ ,  $2^+$  and  $1^+$ . So one would expect the resonant breakup of  ${}^6\text{Li}$  into  $\alpha + d$  via all its  $3^+$ ,  $2^+$  and  $1^+$  states [23, 24]. However, measurements exist in literature

only for  $3^+$  and  $2^+$  states. Since the excitation energy and width of the ' $1^+$ ' state is very large, the cross section is expected to be less compared to the other two ( $2^+$  and  $3^+$ ) resonance states. Also, since the relative energy of the breakup fragments proceeding via this resonance state is large (4.18 MeV), the detection cone angle [8] is expected to be large requiring a bigger detector system. So far there is no study available in the literature on the experimental breakup cross-section of  ${}^6\text{Li}$  into  $\alpha + d$  by its  $1^+$  state. From earlier studies it was observed that the breakup cross-section of  ${}^6\text{Li}$  into  $\alpha + d$  is less than that of inclusive  $\alpha$ . The failure of explanation of inclusive  $\alpha$  yield makes the subject essential to search for new breakup channels like breakup via new resonant states or through new transfer channels that are responsible for the high yield of  $\alpha$ .

**III.** The  ${}^7\text{Li}$  as a cluster of  $\alpha$  and  $t$  with a binding energy of only 2.47 MeV is very well known. The breakup of  ${}^7\text{Li}$  into  $\alpha + t$  can take place through all possible resonance states corresponding to  $L=3$  [23] i.e., via  $7/2^-$  (4.63 MeV) and  $5/2^-$  (6.67 MeV) states. Direct breakup of  ${}^7\text{Li}$  into  $\alpha + t$  and sequential breakup via the first resonance state ( $7/2^-$ , 4.63 MeV) of the cluster have been measured for several systems. However, there is no measurement available on the sequential breakup corresponding to the second resonance state ( $5/2^-$ , 6.67 MeV). The study of the second resonance state is however very important as various studies on elastic scattering show a significant effect of coupling of the  $5/2^-$  state of  ${}^7\text{Li}$  [25,26]. So, it would be interesting to measure this new channel to understand the mechanism of  $\alpha + t$  resonance breakup deeper.

**IV.** Cluster models of the structure of the light nuclei frequently provide a rather simple description of some of the energy levels which are difficult to access in the usual shell model framework. The model described in Ref. [27] is used to study the low-lying energy levels of the nucleus  ${}^7\text{Li}$ , whose structure is treated as a superposition of the cluster structures ' $\alpha+t$ ' and ' ${}^6\text{Li}+n$ ' with binding energies of 2.47 and 7.25 MeV respectively. When both cluster structures are considered simultaneously, the optimal separation between the clusters  $\alpha$  and  $t$  and the separation between the clusters  ${}^6\text{Li}$  and  $n$  in the ground state are

equal to the corresponding separations ( $\sim 3.5$  fm) in the excited state and the minimal energy of  ${}^7\text{Li}$  is lowered by 1.96 MeV [27]. Other possible cluster structure like  ${}^6\text{He} + p$  was not considered into the model because of its high binding energy ( $\sim 9.96$  MeV) [27]. Investigation on the breakup channel  ${}^7\text{Li} \rightarrow {}^6\text{He} + p$  will shed light on the possibility of the another cluster structure of  ${}^7\text{Li}$ .

**V.** The importance of the  $2\alpha$  cluster structure of  ${}^8\text{Be}$  at its ground state ( $0^+$ ) as well as other two resonance states at 3.12 MeV ( $2^+$ ) and 11.35 MeV ( $4^+$ ) is well reflected by the values of the spectroscopic factors for  $\langle {}^8\text{Be} | \alpha + \alpha \rangle$  overlaps:  $S(\text{g.s.})=0.84$ ,  $S(2^+)=0.83$ , and  $S(4^+)=0.75$  [28]. Since the third resonance state ( $4^+$ ), like other two states, has a good overlap between two  $\alpha$ -particles in the cluster [29], the breakup of  ${}^8\text{Be}$  into two  $\alpha$  via this state is also possible at favorable excitation energies. However, there is no experimental evidence reported so far on the observation of  ${}^8\text{Be}$  breakup via the  $4^+$  resonance state. So it would be interesting to investigate experimentally the existence of  ${}^8\text{Be}$  breakup via its third resonance state and compare with the breakup probabilities via its  $0^+$  and  $2^+$  states.

**VI.** Another interesting aspect of the breakup process is the vicinity of the breakup to the target that is related to the time scale of the intermediate projectile-like fragment via which the breakup takes place. If the breakup occurs prior to reaching the fusion barrier (near target breakup), then that breakup is accountable for incoming flux loss. On the other hand if the breakup occurs a long way far while receding from the target nucleus, called asymptotic breakup, it would no longer be responsible for incomplete fusion cross-section. Thus to identify the breakup states responsible for incomplete fusion it is essential to separate out the asymptotic breakup components from the near target one.

# Chapter 2

## Experimental methods

The detection and identification of the particles originated from the collision of two nuclei are fundamental tools to study different aspects of nuclear reactions. The identification corresponds to the details of mass, charge, kinetic energy and the emission angle of the particle. If in a nuclear reaction, the outgoing channel consists of two particles, then one can reconstruct the kinematic details of the reaction by just detecting and identifying one of the particles. But the situation becomes more complex if there are three particles in the outgoing channel. Breakup, nucleon transfer followed by breakup, etc., are the examples of these types of reactions. For a reaction involving three particles in the outgoing channel, one needs to detect at least two of them in coincidence in order to extract the kinematical information about the reaction. As the principal goals of this thesis are (i) to study the mechanism of breakup of  ${}^6\text{Li}$  and  ${}^7\text{Li}$  projectiles by a medium mass target  ${}^{112}\text{Sn}$  and (ii) measure the breakup cross-sections to understand the contributions of break-up channels to total reaction, it is very very important to detect the charged particles produced from the breakup reaction in coincidence with high efficiency. Study of these reactions involves the generation and acceleration of projectile followed by the detector setup, electronics and data acquisition system. The details of each of the components are described in the following subsections.

## 2.1 Generation and acceleration of the projectile

The study of low energy nuclear reaction generally involves projectiles having energies of the order of few tens of MeV/nucleon. This can be obtained by accelerating the projectiles. All the measurements reported in this thesis were carried out using the BARC-TIFR 14UD Pelletron-LINAC facility at Mumbai.

The ion source named SNICS (Source of Negative Ions by Cesium Sputtering) has been attached to the top of the accelerator, which produces negative ions of the desired projectile. The negative ions are initially accelerated to low energies (150-250 KeV) in short horizontal section till they reach the injector magnet. In injector magnet the ions are mass analyzed by the 90° bending magnet to remove the impurities before the entry into the vertical accelerator column. The injected negative ions are then accelerated by the high voltage terminal situated at the center of the accelerator and thus gain an energy equal to the amount of terminal voltage ( $V_T$ ). The high voltage at the terminal is obtained by continuous transfer of charge to the terminal by means of the chain of steel pellets, hence the name Pelletron accelerator. Inside the terminal, the ions are passed through the carbon stripper foils where they lose their electrons due to the charge exchange collision with the stripper material. As a result positive charge state 'q' is obtained by the ions after passing through the stripper section. The ions are then repelled by the high voltage terminal and thus accelerated with energy  $qV_T$  till they reach the analyzing magnet. Thus, the energy gained by the ions in the two stage acceleration is  $(q+1)V_T$ . Analyzing magnet is used to bend the ions according to [31]

$$B = 720.76 \frac{\sqrt{mE}}{q} \quad (2.1)$$

where, 'B' is the magnetic field in Gauss and 'm' is the mass of the ion in a.m.u. and 'E' is the energy of the accelerated ion in MeV. The magnet is also used to extract out the desired charge state of the ion. After extraction of the desired charge state, ion beam can

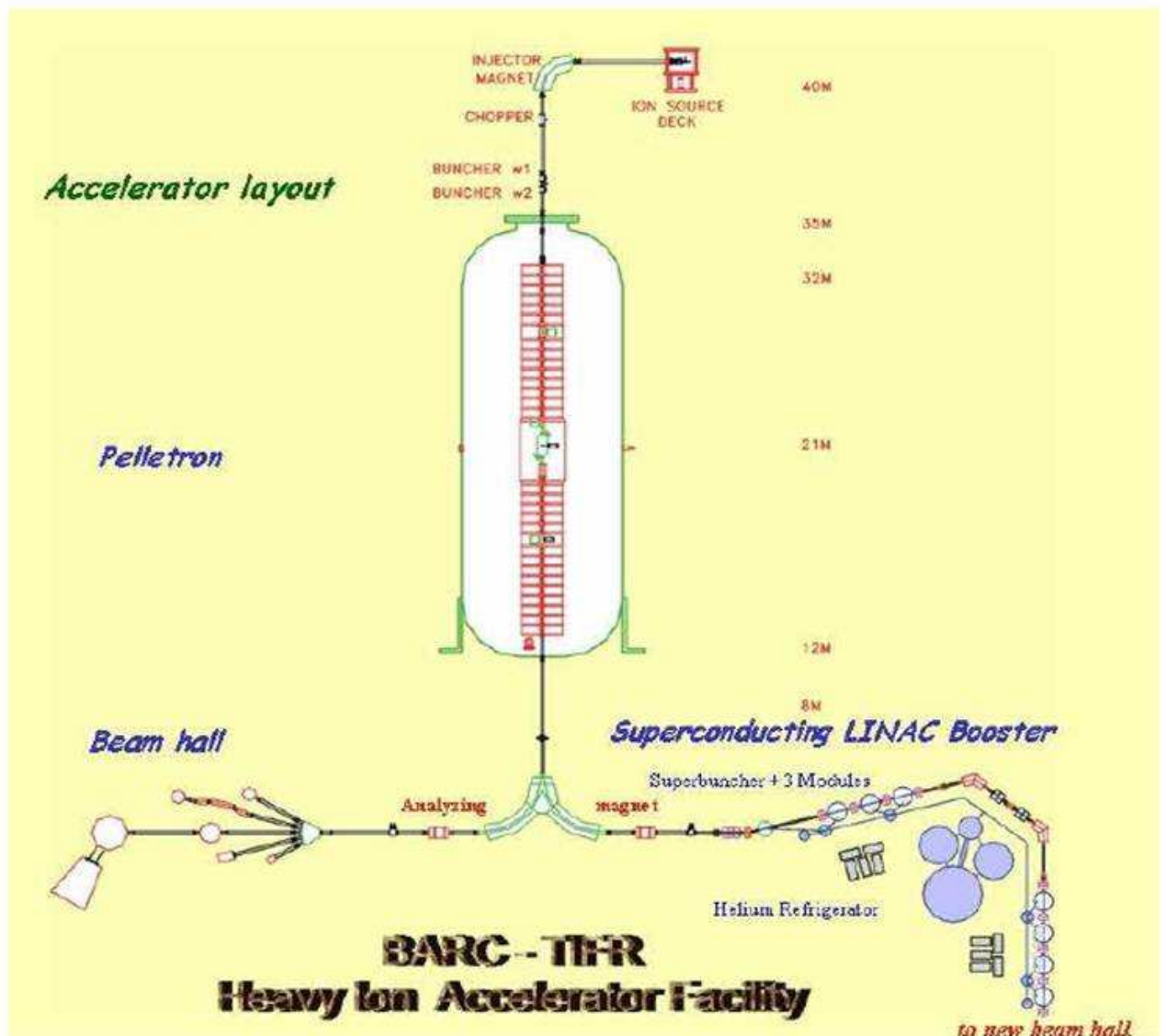


Figure 2.1 Layout of the Pelletron-LINAC accelerator facility at TIFR, Mumbai, India [30].

be taken to one of the five beam lines by using switching magnet. There are five beam lines  $0^\circ$ ,  $15^\circ\text{N}$ ,  $15^\circ\text{S}$ ,  $30^\circ\text{N}$ , and  $30^\circ\text{S}$  in the Pelletron beam hall, three beam lines  $15^\circ$ ,  $30^\circ$ , and  $45^\circ$  in LINAC Hall-1, and three beam lines  $15^\circ$ ,  $30^\circ$ , and  $45^\circ$  in LINAC Hall-2. LINAC is used to boost the energy of the Pelletron beam. In the present study the energy delivered by the Pelletron was sufficient and LINAC booster was not used and hence not discussed.

All the measurements of the thesis involving the breakup and transfer-breakup reactions have been carried out at  $30^\circ$  beam line in LINAC Hall-1 using the general purpose scattering chamber [32].

## 2.2 Interaction of charged particle with matter

Since the electromagnetic interaction has long range, it is not necessary for the light or heavy charged particle to always make a direct collision with an atom. When a charged particle enters the detector, it will interact mainly with the orbital electrons of the material of the detector by the Coulomb field. While passing through the detector, the particle will transfer its energy to the atom. Depending on the incident energy, the charged particle may be able to excite the atoms into higher levels or remove electrons from the atom. Interaction between the particle with orbital electrons leads to the energy loss of the particle.

The energy loss of the incident particle inside the detector increases with decrease in energy and is given by the Bethe-Bloch formula [33]:  $-\frac{dE}{dx} \propto \frac{MZ^2}{E}$ , where  $E$  is the incident energy,  $M$  is the mass and  $Z$  is the atomic number of the particle. This is the principle of energy loss which is used in  $\Delta E - E$  telescope configuration for particle identification. The  $\Delta E$  detector is a thinner detector where the particle loses some of its energy and then while passing through the thicker one i.e. through  $E$  detector it will lose all of its energy and get stopped. The plotting of the energy loss in  $\Delta E$  with  $E$  creates different bands for different projectile-like fragments and thus helps to identify the fragments.

## 2.3 Semiconductor detector for charged particle detection

Now-a-days, semiconductor detector is being extensively used for nuclear reaction studies, because of its several advantages, such as,

- (i) because of the small band gap ( $\sim 1$  eV), the generation of electron-hole pair is easier in semiconductor detector as compared to the gas detector,
- (ii) semiconductor detectors are compact in size.

The semiconductor detector is basically a reversed biased p-n junction diode. When a p-n junction diode is operated in a reverse biased mode, the depletion depth is increased with the bias voltage and ultimately makes the detector fully depleted of free charge carriers. So when an energetic charged particle enters into the semiconductor detector, it will create ionization in the depletion region, generating electron-hole pairs and drift of these charge carrier produces an electrical signal. The amplitude of the signal is directly proportional to the deposited energy by the incident particle.

The semiconductor detectors used in our experiments are silicon surface barrier detectors and silicon strip detectors.

### 2.3.1 Silicon surface barrier detector

Generally, n-type silicon wafer is oxidized on one side and then coated with thin layer of gold to form the p-n junction. Slight oxidation before evaporation of gold layer plays an important role in the properties of the surface barrier. The junction is then mounted in an insulating ring with metalized surfaces for ohmic contacts. The detectors fabricated using this way is known as silicon surface barrier detector (SSB) as the barrier is formed at the surface of the crystal. SSBs can be made with varying thickness and depletion region. For the transmission type of detector, the depletion region is extended entirely into the thickness of silicon wafer makes them efficient to measure the energy deposition

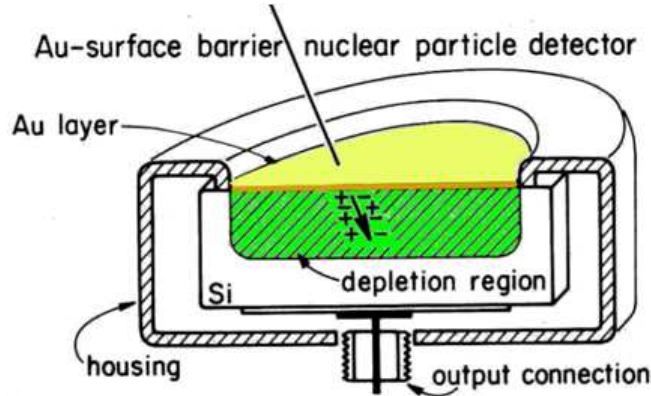


**Figure 2.2** The typical configuration of a silicon surface barrier detector.

by the particle. Typically, this technology allows production of such transmission type of detector having thicknesses ranging from  $10\ \mu\text{m}$  to few mm [34]. The typical configuration of a silicon surface barrier detector is shown in Fig. 2.2.

### 2.3.2 Silicon strip detector

To fulfill the demand of detectors with large solid angles for measuring low cross sections using coincidence technique, now-a-days segmented large area Si strip detectors are being used. They are constructed with segmented p-side and n-side contacts and widely used in nuclear and particle physics experiments. Both single and double-sided detectors are available. In all experiments of this thesis, double-sided silicon strip detectors are used to obtain position and energy loss information. The typical energy resolution of individual strips are  $\sim 50\ \text{KeV}$ . The front side of a typical Micron-make W1-type silicon strip detector is shown in Fig. 2.3.

## 2.4 Experimental setup

In all experiments relevant to the thesis, the main focus was to detect the binary breakup fragments in coincidence. The breakup fragments are emitted at particular cone angle [8],

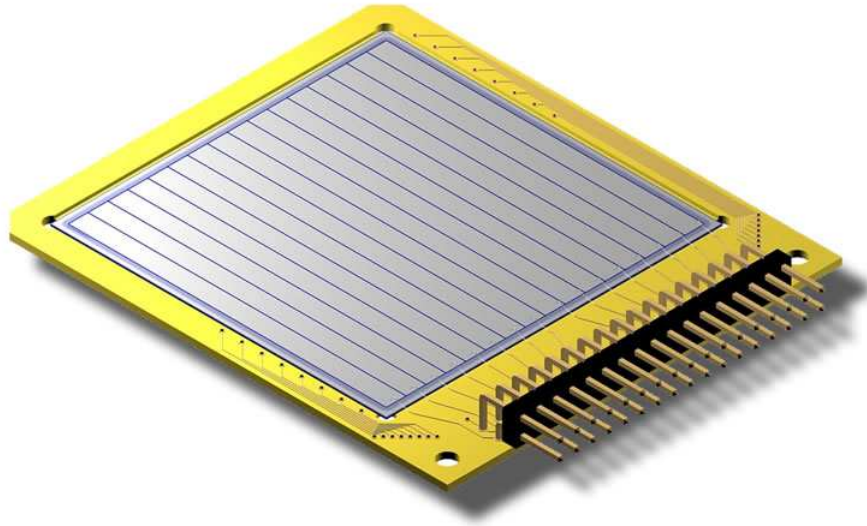


**Figure 2.3** The front side of a typical Micron-make W1-type silicon strip detector.

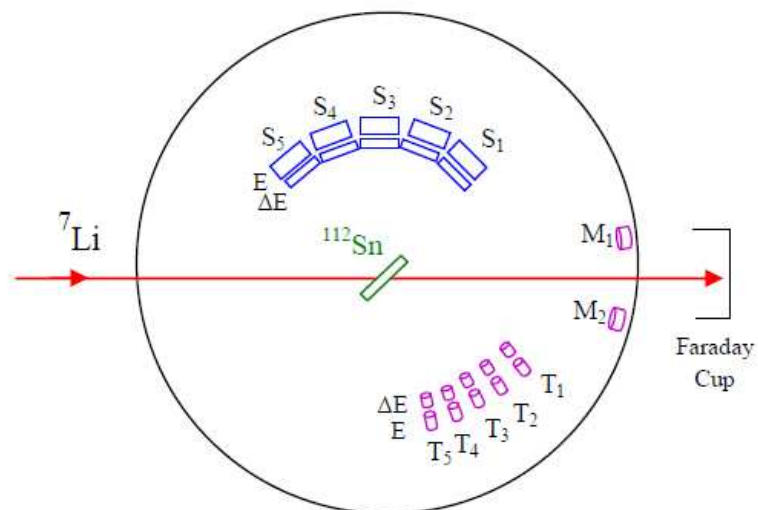


**Figure 2.4** The schematic diagram of the experimental setup showing strip detector array, single telescopes and monitors inside the scattering chamber.

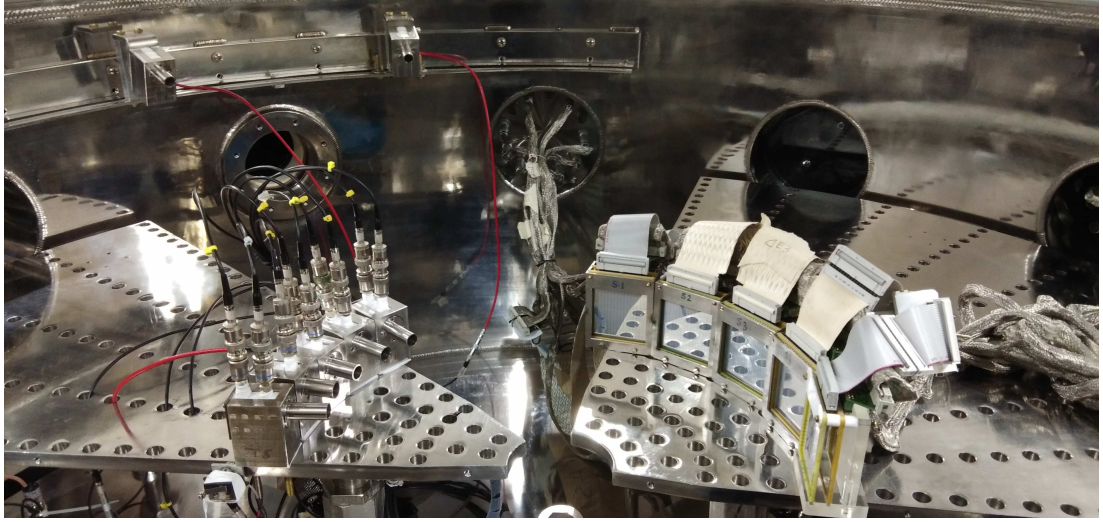


**Figure 2.5** The photograph of double-sided silicon strip detector array along with surface barrier telescopes at BARC-TIFR Pelletron-LINAC facility, Mumbai, India.

depending on the excitation energy of the projectile like fragment (PLF) before breakup as well as the kinetic energy (K.E) of PLF. As we were interested to detect the different dominant direct, resonant and transfer breakup channels, an array of maximum five silicon telescopes with large angular coverage was used for all our experiments. Each strip telescopes consists of two Si strip detectors (Micron semiconductor W1 type), with typical thickness of  $\sim 60 \mu\text{m}$  and  $\sim 1500 \mu\text{m}$  respectively. Each detector has 16 vertical strips in its front side and 16 horizontal strips in its back side (with 256 pixels) covering an active area of  $50 \text{ mm} \times 50 \text{ mm}$ , with length and breadth of each strip  $50 \text{ mm}$  and  $3.1 \text{ mm}$  respectively. Five such sets of strip telescopes placed side by side cover a total angular range of about  $\sim 93^\circ$ . Two Si surface barrier detectors (of thicknesses  $\sim 1000 \mu\text{m}$ ) kept at  $\pm 20^\circ$  were used to monitor the incident flux by measuring the Rutherford scattering. In addition, there were five single telescopes ( $T_1$ - $T_5$ ) of silicon surface barrier detectors (with  $\Delta E \sim 50 \mu\text{m}$ ,  $E \sim 1000$ - $2000 \mu\text{m}$ ) placed on the second rotatable arm of the scattering chamber to measure the elastic scattering angular distribution covering larger angular range. The schematic diagram of the experimental setup is shown in Fig. 2.4 and the actual picture is displayed in Fig. 2.5.

## 2.5 Electronics for signal processing and DAQ

Any electrical signal produced from the detector has two branches, the energy branch and the timing branch that needs to be processed through the electronic circuit in order to extract the desired information. The energy branch of the signal is processed through preamplifier, amplifier and then ADC whereas in order to extract the timing information of the signal one needs TFA, CFD, LOGIC-UNIT, GDG etc. The typical schematic diagram is shown in Fig. 2.6. For signal processing from the segmented Si-strip detectors, MPR-16 preamplifier and MSCF-16 shaping time filter modules were used. Both MPR-16 and MSCF-16 modules were developed by the Mesytec GmbH and Co. These compact modules are having 16 channels, designed specially for segmented silicon detectors. Signals from detectors were taken outside the chamber using suitable adapters, cables and feed-through. These signals were then fed to the 16 Channel preamplifier MPR-16. The differential output signals from MPR-16 is further processed by MSCF-16 modules. MSCF-16 is a shaping and timing filter amplifier with constant fraction discriminator and trigger output. The shaper output signal of the module MSCF-16 contains the energy information that were digitized by peak-sensing ADC(Analog to digital converter). In all experiments, CAEN v-785 modules were used as peak sensing ADC. The signals of silicon surface barrier detectors are processed through MSI-8 modules, which serves as preamplifier as well shaping amplifier. The shaper outputs were then digitized via the ADC CAEN v-785.

The trigger signal of the front side of E-detector was taken from the trigger output of MSCF-16. When one of the strip is fired, then trigger output gives signal. The OR of these trigger output for different strip telescopes and the common timing signals from MSI-8 module were stretched to  $4\mu\text{s}$  by using gate and delay generator module. This signal is known as raw-master. The busy signals from ADCs were used to VETO the raw-master to generate actual master. Signals from the DAQ were collected using an in-house data collection program (LAMPS) developed by Chatterjee *et. al* [35]. For offline processing, the data were characterized through ROOT [36] format using newly

written scripts. ROOT is an object oriented data analysis framework, written in C++ and developed by CERN.

## 2.6 Analysis method for breakup fragments in coincidence

Electrical connections from  $\Delta E^{front}$ ,  $E^{front}$  and  $E^{back}$  are taken from strip telescope. The  $\Delta E^{front}$  and  $E^{front}$  together helps to identify the different charged particle through the energy loss formula given by Bethe-Bloch [33]. The  $E^{front}$  and  $E^{back}$  detector together gives the information of the position of the hitted particle. So combinedly  $\Delta E$  (means  $\Delta E^{front}$ ) and  $E$  (means  $E^{front}$  and  $E^{back}$ ) detectors help us to identify the particle and give us the energy as well as position information.

The typical inclusive two-dimensional energy-calibrated spectrum of  $\Delta E$  versus  $E_{total}$  obtained from a strip telescope as shown in Fig. 2.7 shows a good separation of the particles with different masses ( $A=1-7$ ) and charges ( $Z=1-3$ ) produced by different reaction mechanisms for the  ${}^7\text{Li}+{}^{112}\text{Sn}$  system. It was observed that an  $\alpha$  detected in one pixel can be in coincidence with any of  $t$ ,  $d$ ,  $p$  and  $\alpha$  particles in another pixel indicating the presence of direct or resonant,  $-1n$  transfer,  $-2n$  transfer and  $+1p$  transfer breakup, respectively. The  $-1n$  and  $-1p$  transfer reactions that survive post breakup produce  ${}^6\text{Li}$  and  ${}^6\text{He}$  respectively. However, both  ${}^6\text{Li}$  and  ${}^6\text{He}$  can also be produced from the direct breakup of  ${}^7\text{Li}$  into  ${}^6\text{Li}+n$  and  ${}^6\text{He}+p$  fragments respectively.

Experimentally, the vertical strip number in  $E^{front}$  detector and the horizontal strip number in  $E^{back}$  detector where a particular particle hits were identified in event by event mode. Say, the central position of the strip detector is at a distance  $d_0$  from the target center and assigned as the origin (0,0) in the (x,y) plane and also assume that the central portion of the strip detector is at angle  $\theta_0$  with respect to the beam direction. Now if the particle hit is recorded at some  $i^{th}$  vertical strip and  $j^{th}$  horizontal strip then the associated

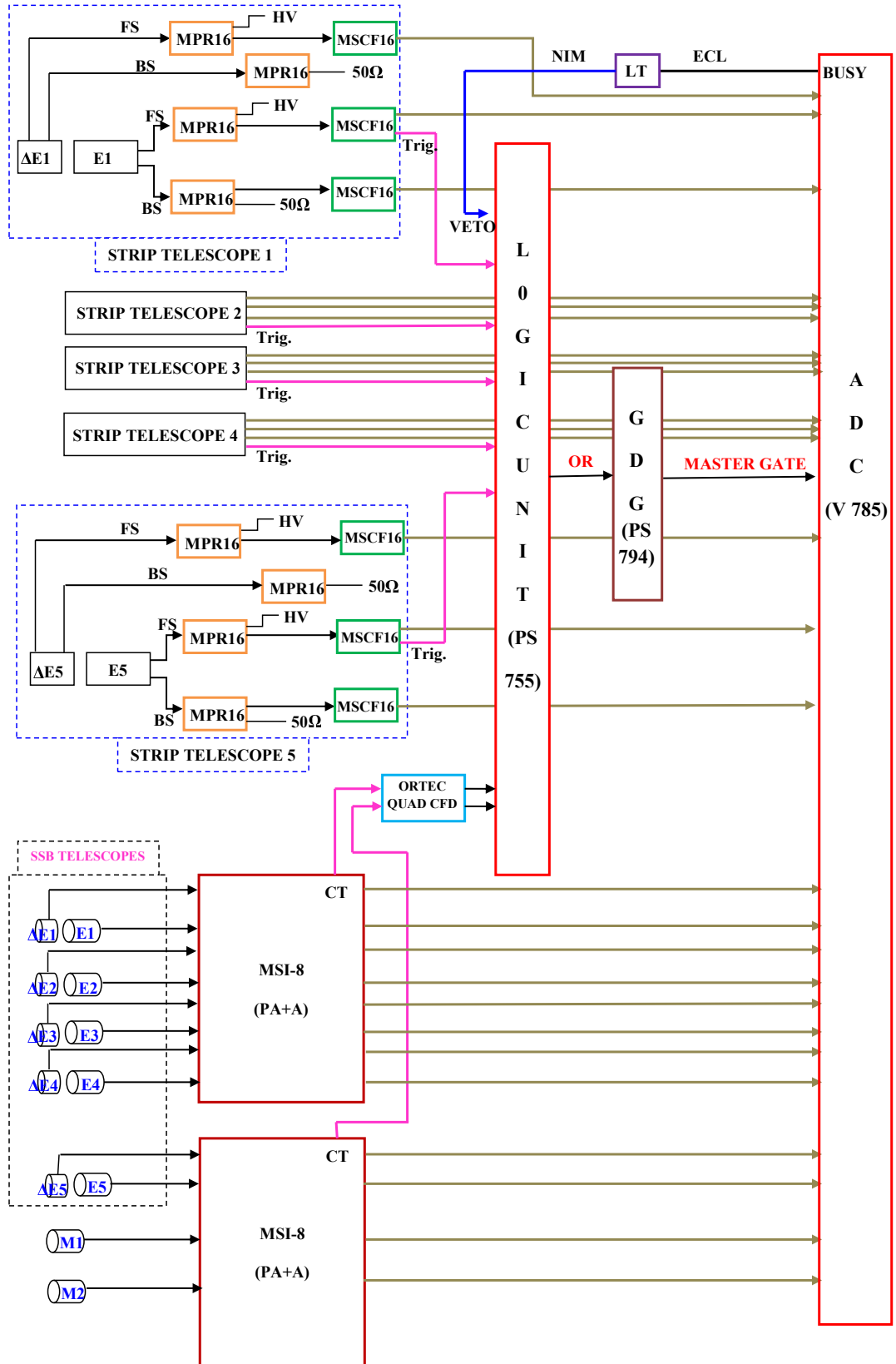
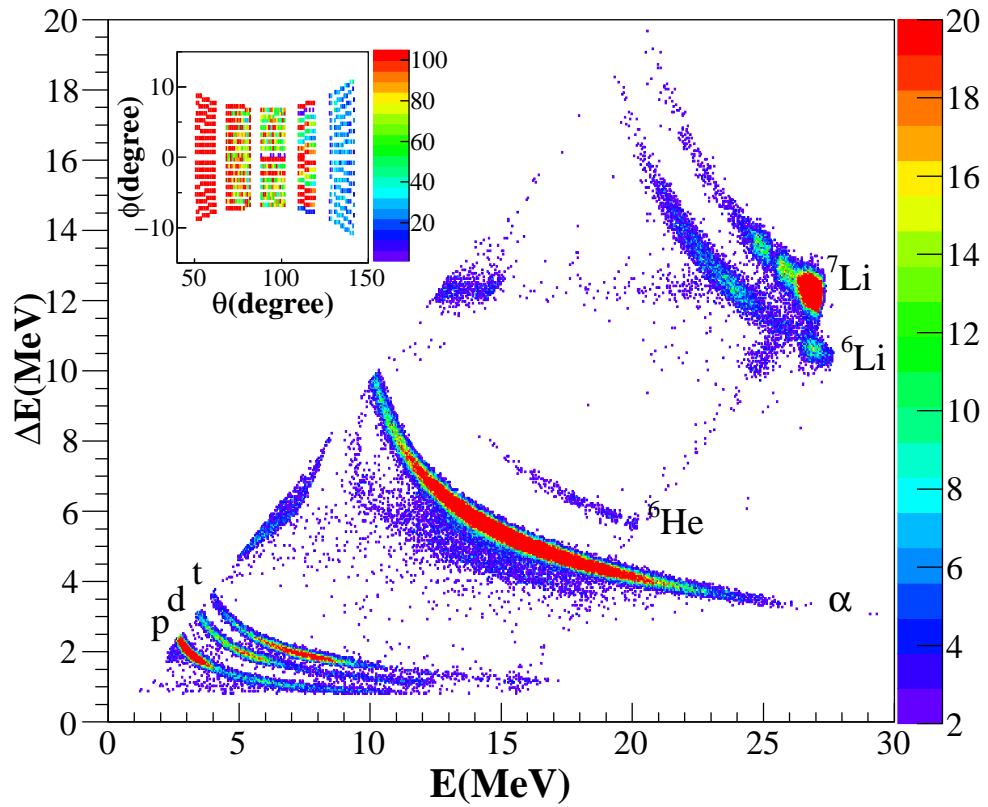
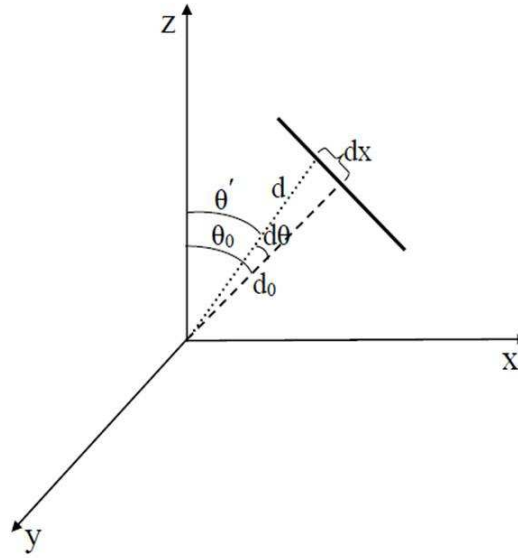


Figure 2.6 Block diagram of the electronics for the measurement of breakup fragments.



**Figure 2.7** Typical two-dimensional ( $\Delta E$  versus  $E_{\text{total}}$ ) energy-calibrated spectrum acquired in one of the vertical strips at  $\theta = 70^\circ$  for a beam energy of 30 MeV. The inset shows the total coverage in  $\theta$  and  $\phi$  by the strip detector array, and the intensity represents the number of  $\alpha$  particles detected in coincidence with  $t$ ,  $d$ , or  $p$  in any two vertical strips.



**Figure 2.8** Schematic of co-ordinate transformation.

pixel position co-ordinate  $(x', y')$  with respect to the central position of the detector can be determined by the equation:

$$x' = (i - 8.5) * \delta d \quad (2.2)$$

$$y' = (j - 8.5) * \delta d \quad (2.3)$$

Where,  $\delta d$  is the inter-pixel distance and for our case it is 0.312 c.m. The central position of the hitted vertical strip is say at an angle of  $\theta'$  with respect to the beam direction.

Then,

$$\theta' = \theta_0 - d\theta \quad (2.4)$$

One can further simplify the above equation to:

$$\theta' = \theta_0 - \tan^{-1}\left(\frac{x'}{d_0}\right) \quad (2.5)$$

Now, the distance between the central position of the hitted strip and the target center can be found out from the relation :

$$d = \sqrt{d_0^2 + x'^2} \quad (2.6)$$

By knowing  $d$  and  $\theta'$ , one can easily able to find out the position information:

$$z = d \cos(\theta') \quad (2.7)$$

$$x = d \sin(\theta') \quad (2.8)$$

$$y = y' \quad (2.9)$$

By co-ordinate transformation one can find out the  $(r, \theta, \phi)$  from the following relation:

$$r = \sqrt{x^2 + y^2 + z^2} \quad (2.10)$$

$$\theta = \cos^{-1}\left(\frac{z}{r}\right) \quad (2.11)$$

$$\phi = \tan^{-1}\left(\frac{y}{x}\right) \quad (2.12)$$

The data analysis of the events gathered in our Double Sided Silicon Strip Detector array is to associate each event in a pixel with the above coordinate  $(r, \theta, \phi)$  on the sphere. All the kinematic reconstruction relies on these co-ordinates.

Using the laboratory detection positions of two breakup fragments of each coincident event, the values of ' $\theta, \phi$ ' of outgoing  ${}^7\text{Li}$  (for  $\alpha + t$  breakup and  ${}^6\text{He} + p$  breakup) or  ${}^6\text{Li}$  (for  $\alpha + d$  breakup) or  ${}^5\text{Li}$  (for  $\alpha + p$  breakup) have been obtained. The inset of Fig. 2.7

shows the effective range of  $\theta(\sim 51^\circ - 142^\circ)$  and  $\phi(\sim \pm 7^\circ - \pm 11^\circ)$  coverage of the strip detector array used in the present setup. The distribution of events shown in the inset figure correspond to the number of  $\alpha$  particles detected in coincidence with either  $t$  or  $d$  or  $p$  in any two vertical strips out of all five strip-telescopes.

## 2.7 Coincidence efficiency of Double Sided Silicon Strip Detector (DSSD) array

Consider a primary two body reaction  $A(a,b)B$ , where projectile ‘a’ is incident on target ‘A’, forming ejectile ‘b’ and recoil ‘B’. The laboratory and center of mass of frame for this two body reaction is labeled as LAB and C.M respectively and presented in Fig. 2.9. Assume that the nucleus ‘b’ is quasi-bound, that means it will subsequently decays into say particle ‘c’ and ‘d’, which are emitted in opposite direction in the center of mass frame of projectile like fragment(PLF) ‘b’ isotropically. Their velocity vectors constructs a center-of-mass breakup sphere that is prescribed by the dashed circle in the Fig. 2.9. The mean lifetime of the quasi-bound nuclei decides the location of the breakup that means whether the breakup is far away from the nuclear interaction region or not. Depending on the location, the breakup is referred to as asymptotic breakup or near target breakup.

For isotropic distribution of breakup in the center-of-mass frame of PLF, the magnitude of the velocity of the fragment ‘d’ is given by,

$$v_{c.m}^d = \sqrt{\frac{2Q}{m_d(1 + \frac{m_d}{m_c})}} \quad (2.13)$$

and, then  $v_{c.m}^c$  can be found out from the following relation

$$v_{c.m}^c = \frac{m_d}{m_c} v_{c.m}^d \quad (2.14)$$

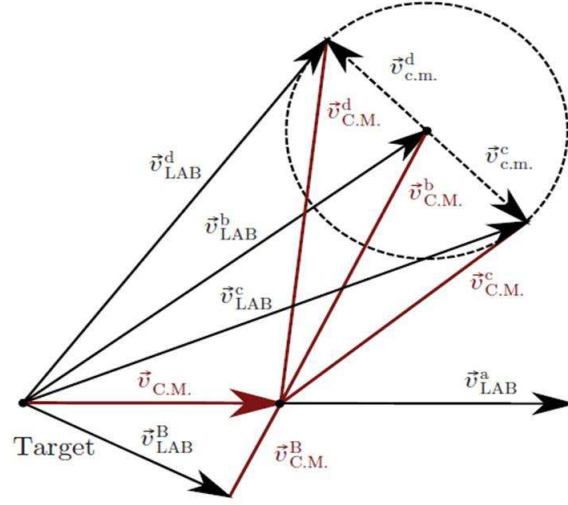


**Figure 2.9** Velocity diagram displaying the laboratory and center-of-mass frames for decay of projectile-like fragment [37].

From the velocity vector diagram, it is clear that

$$\vec{v}_{LAB}^{c,d} = \vec{v}_{LAB}^b + \vec{v}_{c.m.}^{c,d} \quad (2.15)$$

Now,  $\vec{v}_{c.m.}^{c,d} = \{v_1^{c,d}, v_2^{c,d}, v_3^{c,d}\}$ , where  $v_1^{c,d}$ ,  $v_2^{c,d}$ ,  $v_3^{c,d}$  are the x, y and z components of the vector  $\vec{v}_{c.m.}^{c,d}$ . We considered isotropic breakup  $b \rightarrow c + d$  in center of mass frame and randomly selected the breakup direction  $\theta$ ,  $\phi$  for ‘c’, such that  $\theta$  lies between  $[0, \pi]$  and  $\phi$  lies between  $[-\pi, \pi]$ , then automatically the conservation of linear momentum suggests that the direction of ‘d’ will be  $\pi - \theta$  and  $\phi + \pi$  for each trial. The velocity vector of products ‘c’ and ‘d’ in the lab frame  $\vec{v}_{LAB}^c$  and  $\vec{v}_{LAB}^d$  are then reconstructed from the equation 2.15 for each possible values of  $\theta_{LAB}^b$ ,  $\phi_{LAB}^b$ , Q-value and  $E_{rel}$ . The intersection points of the two vectors with the detector plane were then determined. A trial was treated as unsuccessful when (i) any of the two intersecting points (IP) lies out of the detector boundary, (ii) both IP are found to lie on a same vertical strip and (iii) any of the energy for c and d lies below the detection threshold. The efficiency thus provides the no. of successful events out of total no. of events. The conversion of the energy and

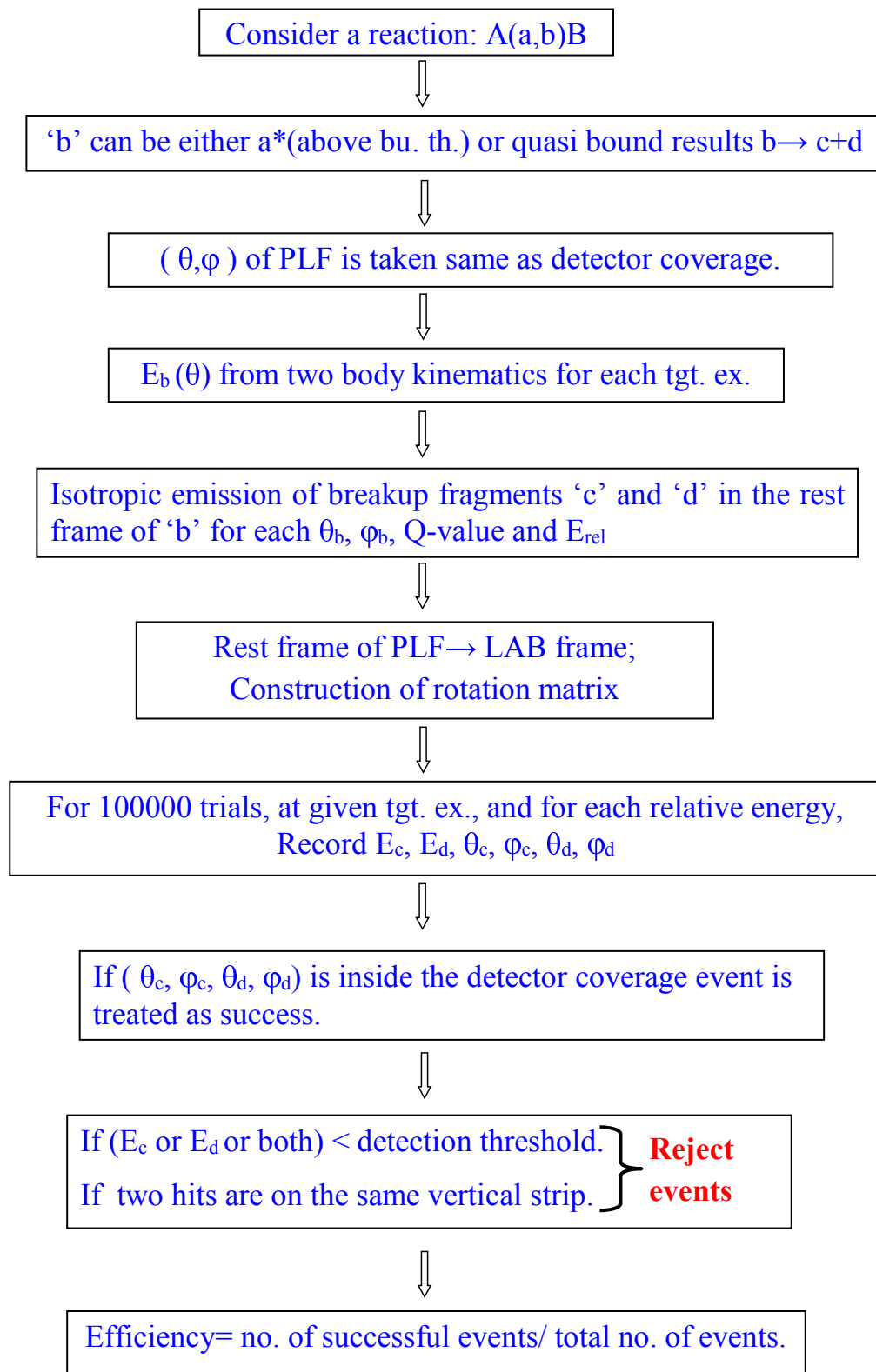


**Figure 2.10** The flow chart for the simulation of 3-body kinematics using Monte Carlo technique.

scattering angle from the laboratory frame to the c.m. frame of the projectile-target in event-by-event mode automatically takes care of the Jacobian of the transformation.

The estimated detection efficiency of different coincidence events depend on relative energy of the breakup fragments, energy of the projectile-like fragment prior to breakup, mass asymmetry of the breakup fragments, detection threshold, and geometric solid angle of the detection setup. Since the energy of the projectile-like fragment prior to breakup depends on the reaction Q-value and the loss of kinetic energy due to the excitation of the target, detection efficiency will also be affected by these parameters.

The data reduction procedure and results are presented in following chapters.

# Chapter 3

## Coupled reaction channels formalism

### 3.1 Introduction

When a projectile approaches towards the static target in LAB frame, the interaction between them takes place in several ways. If we assume that they are nothing but the cluster of nucleons, then mainly their primary interaction results from the two-body inter-nucleon force. However, this assumption is not true always, one or more rearrangement process may take place during collision. Elastic scattering as well as several non-elastic interaction will take place as a result of their interaction. Depending on the time-scale of interaction, the interaction of nuclear process is categorized into two sub parts: (i) direct reaction process and (ii) compound nuclear process. When a nuclear reaction takes place directly from the initial state to the final state without the forming of intermediate nucleus within a time scale of  $\sim 10^{-22}$  sec., the reaction process is known as direct reaction process. Now if the nuclear reaction takes place through the formation of intermediate nucleus (i.e complete equilibration) then that process is known as compound nuclear process with typical time scale of  $\sim 10^{-16}$  sec.. As the time scale of direct reaction process is fast compared to the compound nuclear process, only a few modes (degrees of freedom) are involved in direct nuclear process. So one can assume that direct reaction process to be peripheral.

For instance, inelastic excitations may happen, when either of the nuclei are deformed or deformable. As a result, higher-energy states of the nuclei may become populated. Single-particle excitations are another kind of inelastic process, when a particle in one of the nuclei is excited during the reaction from its initial bound state to another state which may be bound or unbound. Inelastic excitations of the projectile to the unbound state above breakup threshold leads to the dissociation into its cluster components. Nucleons may likewise exchange from one nucleus to the other, either independently, or as the concurrent exchange of two nucleons as a particle cluster. Sometimes it may also happen that after transfer the quasi-bound nucleus is formed resulting into breakup. These kinds of reactions fall into the category of direct reaction process.

In this chapter the main focus is to understand the direct reaction process involved in a nuclear collisions and to portray the method of determination of cross-section associated with each process. Before going to start the discussion on nuclear model involving direct reaction channels, let us emphasize some of the important features of a nucleus. As this thesis deals with the collision of two nuclei near the Coulomb barrier, the kinetic energy of the projectile is negligible as compared to its rest mass energy, leading to the assumption of non-relativistic approach to be able to describe the nuclear reaction. But if we look deep inside, the scenario will be different. The estimated velocity of such nucleon will be  $\sim 0.3c$  and corresponding de Broglie wavelength will be  $\sim 4.0$  fm, which is comparable to nuclear radius ranging from 1.2 fm to 1.4 fm, leading to the fact that quantum effect must have to be incorporated in case of nuclear interaction. So in order to get the information regarding direct reaction channels, the framework of the theory will be based on Schrödinger equation. But one can not separately solve the Schrödinger equation for each channel, as there is effect due to the other channels also. In the following section I will discuss the framework where one can solve the equation for different reaction channels simultaneously to get the reaction cross-section for each individual channel.

## 3.2 Coupled-channels method

During any nuclear collision, many reaction channels are opened up. Each reaction channel can be represented by their basis states. The total wave-function can then be written as a superposition of the basis states.

If there are  $N$  reaction channels, one can write the total wave-function as:

$$|\Psi_{tot}\rangle = \sum_{i=1}^N a_i |\psi_i\rangle \quad (3.1)$$

The total space of the complete wave-function can be assumed as a combination of direct reaction space and compound nuclear reaction space. As our focus is on direct reaction channels, in order to get the information regarding the different direct reaction channels one has to project out the complete wave-function on to direct reaction space.

If we construct the projection operator  $\hat{P}$  responsible for projecting out the total wave-function on to model space (contain the channels of interest), then

$$\hat{P}|\Psi_{tot}\rangle = |\Psi\rangle = \sum_{i=1}^N a_i |\phi_i(\zeta)\chi_i(\vec{R})\rangle \quad (3.2)$$

where,  $|\phi_i\rangle = |\phi_{ip}\phi_{it}\rangle$ ,  $\phi_{ip}$  and  $\phi_{it}$  are the states (bound or continuum) of the projectile and target respectively for the  $i^{th}$  channel and  $\chi_i(\vec{R})$  represents the wave-function depending on the relative separation between them for that channel.

For a complete Hamiltonian  $\bar{H}$  and total energy  $E$ , Schrödinger's equation  $[\bar{H} - E]|\Psi_{tot}\rangle = 0$  becomes  $[H - E]|\Psi\rangle = 0$  in the model space with [38]

$$H = P\bar{H}P - P\bar{H}Q \frac{1}{Q\bar{H}Q - E - i\epsilon} Q\bar{H}P \quad (3.3)$$

where  $Q = 1 - P$  and  $\epsilon$  is a positive infinitesimal quantity whose presence ensures that the excluded channels have a time-retarded propagator, and hence only remove flux from the model space. The second term as a whole describes the effects of the excluded channels

on the model subspace  $P\Psi_{tot}$ . So in order to get the information about the direct reaction channels on model space one has to construct the effective Hamiltonian from equation 3.3.

If our interest is only on the elastic channel, then  $P$  contains only elastic channel and all other inelastic channels will be absorbed in  $Q$ . In elastic scattering both the projectile and the target remain in their ground state. Depending on the bombarding energy and charges of the interacting nucleus, the scattering process can be of different types.

- (i) Rutherford scattering ( $E$  is well below the Coulomb barrier).
- (ii) Fresnel Scattering ( $E$  is around or near the Coulomb barrier).
- (iii) Fraunhofer Scattering ( $E$  is well above the Coulomb barrier).

The total Hamiltonian of the system in the model space can then be written as:  $\hat{H} = \hat{T}_R + \hat{U}(R)$ , where  $U(R)$  is the optical model potential that represents the effective projectile-target interaction.

$$U(R) = U_{nuc}(R) + U_{coul}(R) \quad (3.4)$$

where,

$$U_{coul}(R) = \begin{cases} \frac{Z_p Z_t e^2}{2R_c^3} (3R_c^2 - R^2) & \text{when, } R \leq R_c \\ \frac{Z_p Z_t e^2}{R} & \text{when, } R > R_c \end{cases} \quad (3.5)$$

$$U_{nuc}(R) = V(r) + iW(r) = -\frac{V_0}{1 + \exp(\frac{R - R_0}{a_0})} - i\frac{W_0}{1 + \exp(\frac{R - R_i}{a_i})} \quad (3.6)$$

The optical model potential has two parts, the real part represents the elastic scattering and the imaginary part describes the all other non-elastic channels.

From Schrödinger equation, one can write:

$$[\hat{H} - E]\Psi(\vec{R}) = 0. \quad (3.7)$$

The total wave-function  $\Psi(\vec{R})$  can be written as a superposition of incident and scattered waves.

$$\Psi(\vec{R}) = e^{i\vec{K}\cdot\vec{R}} + \Psi^{(+)}(\vec{R}) \rightarrow e^{i\vec{K}\cdot\vec{R}} + A(\theta)\frac{e^{iKR}}{R} \quad (3.8)$$

Where,  $A(\theta)$  is the scattering amplitude and it is related to the differential scattering cross-section as :

$$\frac{d\sigma}{d\Omega} = |A(\theta)|^2 \quad (3.9)$$

So, in order to get the differential cross-section one has to calculate the scattering amplitude.

Now if we decompose the wave-function into the radial and spherical harmonics part, then:

$$\Psi(\vec{R}) = \sum_{LM} C^{LM} \frac{f^L(R)}{R} Y_{LM}(\hat{R}). \quad (3.10)$$

$f^L(R)$  is the radial part of the wave-function and can be found out by the solving the equation:

$$\left[ -\frac{\hbar^2}{2\mu} \frac{d^2}{dR^2} + \frac{l(l+1)\hbar^2}{2\mu r^2} + U(R) - E \right] f^L(R) = 0. \quad (3.11)$$

Analytical solution of  $f^L(R)$  is very difficult to find out, therefore one has to rely on the numerical procedure. In general, to get the complete solution, one has to integrate the radial wave-function  $f^L(R)$  up-to infinity. But it requires large computation time. As we know that Coulomb field is proportional to  $1/R$ , therefore at large distances its effect decreases and also the nuclear field being short ranged, at large distances, there would be no effect due to nuclear field. Keeping that in mind one has to fix a matching radius,  $R_m$ , up-to which the  $f^L(R)$  should be integrated.  $R_m$  should be sufficiently large such that beyond  $R_m$  the field is incapable to change the wave-function practically. Hence, in order to solve the eqn. 3.11 one need to impose the following boundary conditions:

- (i) The wave-function should be finite at  $R \rightarrow 0$ , so  $\lim_{R \rightarrow 0} f^L(R) = 0$ .
- (ii)  $f^L(R)|_{R=R_m} \rightarrow I_L(R) - S_L O_L(R)$  where,  $S_L$  is the scattering matrix.  $I_L$  and  $O_L$

are the ingoing and outgoing waves respectively.

$$I_L(R) = \frac{1}{\sqrt{v}}(KR)h_L^*(KR) \propto e^{-i(KR-\eta\log 2KR)} \quad (3.12)$$

$$O_L(R) = \frac{1}{\sqrt{v}}(KR)h_L(KR) \propto e^{i(KR-\eta\log 2KR)} \quad (3.13)$$

$S_L$  is the coefficient of the scattering matrix.  $S_L$  is related to the phase shift  $\delta_L$  by  $S_L = e^{2i\delta_L}$ . One can notice that

- (i) When  $U(R) = 0$  then,  $\Psi_{out} = \Psi_{in} \Rightarrow S_L = 1 \Rightarrow \delta_L = 0$ .
- (ii)  $U$  real  $\Rightarrow |S_L| = 1 \Rightarrow \delta_L$  real.
- (iii)  $U$  complex  $\Rightarrow |S_L| < 1 \Rightarrow \delta_L$  complex.
- (iv) For very very large  $L$  i.e when  $L \gg 1$ , then  $S_L \rightarrow 1$ .

The total wave-function can then be written as,

$$\Psi(\vec{R}) = \sum_{LM} C^{LM} \frac{f^L(R)}{R} Y_{LM}(\hat{R}) \rightarrow \sum_{LM} C^{LM} \frac{[I_L(R) - S_L O_L(R)]}{R} Y_{LM}(\hat{R}). \quad (3.14)$$

In presence of Coulomb and nuclear potential, the expression of scattering amplitude  $A(\theta)$  is given by:

$$A(\theta) = \frac{1}{2ik} \sum_{l=0}^{\infty} (2l+1) [e^{2i\eta_L} - 1] P_l(\cos\theta) \quad (3.15)$$

Here,  $\eta_L$  is the phase-shift corresponding to the combined Coulomb and nuclear potential.

So,  $\eta_L$  can be written as:

$$\eta_L = \sigma_L + \delta_L \quad (3.16)$$

Where,  $\sigma_L$  represents the phase shift corresponding to the Coulomb potential only and  $\delta_L$  is the  $\sigma_L$ -subtracted phase shift.

The above expression of  $A(\theta)$  can be algebraically split as:

$$A(\theta) = \frac{1}{2ik} \sum_{l=0}^{\infty} (2l+1) [e^{2i\sigma_L} - 1] P_l(\cos\theta) + \frac{1}{2ik} \sum_{l=0}^{\infty} (2l+1) e^{2i\sigma_L} [e^{2i\eta_L} - 1] P_l(\cos\theta) \quad (3.17)$$

Once  $A(\theta)$  is known one can able to find out the differential scattering cross-section with the help of the eqn. 3.9.

Suppose let us consider our model space consists of two channels, say  $\alpha$  and  $\alpha'$  are opened during the reaction.

Then the corresponding Hamiltonian would be:

$$H = -\frac{\hbar^2}{2\mu} \nabla^2 + h(\zeta) + V(\vec{R}, \zeta) \quad (3.18)$$

Where,  $R$  and  $\zeta$  are the co-ordinates representing the inter-nucleon separation and the internal states of the nucleus.

The internal wave-functions are the solutions of the following equation:

$$h(\zeta)\phi_\alpha(\zeta) = \epsilon_\alpha\phi_\alpha(\zeta) \quad (3.19)$$

where,  $\epsilon_\alpha$  represents the internal energy of the nucleus.

So the model wave-function can be written as:

$$\Psi(\vec{R}, \zeta) = \phi_\alpha(\zeta)\chi_\alpha(\vec{R}) + \phi_{\alpha'}(\zeta)\chi_{\alpha'}(\vec{R}) \quad (3.20)$$

Then, the required Schrödinger equation is given by:

$$H\Psi(\vec{R}, \zeta) = E\Psi(\vec{R}, \zeta) \quad (3.21)$$

From the eqn. 3.21 after some mathematical treatment, one can reach up-to the coupled

equations:

$$[\nabla^2 - U_{\alpha\alpha} + k_{\alpha}^2] |\chi_{\alpha}(\vec{R})\rangle = U_{\alpha\alpha'} |\chi_{\alpha'}(\vec{R})\rangle \quad (3.22)$$

and,

$$[\nabla^2 - U_{\alpha'\alpha'} + k_{\alpha'}^2] |\chi_{\alpha'}(\vec{R})\rangle = U_{\alpha'\alpha} |\chi_{\alpha}(\vec{R})\rangle \quad (3.23)$$

where,  $U_{ij} = \frac{2\mu V_{ij}}{\hbar^2}$  and  $k_i = \sqrt{\frac{2\mu(E_i - \epsilon_i)}{\hbar^2}}$ .

One can write the eqn. 3.22 as:

$$\left[ \nabla^2 - \left( U_{\alpha\alpha} + U_{\alpha\alpha'} \frac{|\chi_{\alpha'}(\vec{R})\rangle}{|\chi_{\alpha}(\vec{R})\rangle} \right) + k_{\alpha}^2 \right] |\chi_{\alpha}(\vec{R})\rangle = 0 \quad (3.24)$$

The above eqn. can be written like:

$$[\nabla^2 - U_{eff} + k_{\alpha}^2] |\chi_{\alpha}(\vec{R})\rangle = 0 \quad (3.25)$$

Where,  $U_{eff}$  is the effective potential which is the sum of the bare potential plus the dynamical polarization potential. The dynamical polarization potential part originates through the inclusion of other channel. Therefore the effect on elastic scattering because of the other channel can be attributed with the polarization potential. As we are interested to find out the differential cross-section which depends on the interaction potential, our task is to find out the effective interaction potential. But for that case the complete solution of  $|\chi_{\alpha}(\vec{R})\rangle$  and  $|\chi_{\alpha'}(\vec{R})\rangle$  is required. One of the method of solving the above equations are iterative method.

First set the term  $|\chi_{\alpha'}(\vec{R})\rangle = 0$  in eqn. 3.22 and solve  $|\chi_{\alpha}(\vec{R})\rangle$  and afterward putting that  $|\chi_{\alpha}(\vec{R})\rangle$  in eqn. 3.23 in order to get the solution of  $|\chi_{\alpha'}(\vec{R})\rangle$ . Again inserting this  $|\chi_{\alpha'}(\vec{R})\rangle$  in eqn. 3.22 to get modified  $|\chi_{\alpha}(\vec{R})\rangle$  and putting that  $|\chi_{\alpha}(\vec{R})\rangle$  eqn. 3.23 will give corrected  $|\chi_{\alpha'}(\vec{R})\rangle$ . This process will continue until the convergence is reached. This method is known as iterative method used to solve the coupled channel equations.

Now, If the model space consists of several channels e.g.,  $\alpha$ ,  $\alpha'$ ,  $\alpha''$ ,  $\alpha'''$  etc., then one can write the equation 3.22 as:

$$[\nabla^2 - U_{\alpha\alpha} + k_{\alpha}^2]|\chi_{\alpha}(\vec{R})\rangle = \sum_{\alpha' \neq \alpha} U_{\alpha\alpha'}|\chi_{\alpha'}(\vec{R})\rangle \quad (3.26)$$

If all the matrix elements  $U_{\alpha\alpha'}$  are known, then only one can solve these coupled equations and get a complete set of description of the reaction. However, it is very difficult to solve these equation exactly as there are infinite no. of reaction channels, so one has to make an approximation. The approximation is to truncate the infinite no. of channels into a few channels those are expected to be strongly coupled known theoretically or experimentally and neglect the rest of the channels or represent their effect by complex optical potential . This approximation is sometimes known as strong coupling approximation or the coupled channel method.

But though the above approximation is useful for inelastic scattering cross-section but are not well suited for rearrangement collisions [39]. So one has to search for the other methods like Born approximation.

### 3.3 Born approximation and DWBA method

The scattering of particle by a center of force can be written as:

$$[\nabla^2 + k^2]|\chi(\vec{R})\rangle = U(\vec{R})|\chi(\vec{R})\rangle = F(\vec{R}) \quad (3.27)$$

When , the potential  $V = 0$ , this becomes the equation for the free particle of energy  $E$ ,

$$[\nabla^2 + k^2]|\chi_0(\vec{R})\rangle = 0 \quad (3.28)$$

whose solution is plane wave,  $\chi_0(\vec{R}) \sim \exp(i\vec{k} \cdot \vec{R})$ . The presence of the interaction potential  $V$  introduces scattered waves in addition to the incident plane wave.

The general solution of the Schrödinger equation mentioned in eqn. 3.27 takes the form [39]:

$$\chi(\vec{k}, \vec{R}) = e^{i\vec{k} \cdot \vec{R}} - \frac{1}{4\pi} \int \frac{e^{i\vec{k} \cdot |\vec{R} - \vec{R}'|}}{|\vec{R} - \vec{R}'|} U(\vec{R}') \chi(\vec{k}, \vec{R}') d\vec{R}' \quad (3.29)$$

Simplifying the above solution for large  $R$ , one may get

$$\chi(\vec{k}, \vec{R}) \xrightarrow{\text{large } R} e^{i\vec{k} \cdot \vec{R}} - \frac{e^{i\vec{k} \cdot \vec{R}}}{4\pi R} \int e^{-i\vec{k}' \cdot \vec{R}'} U(\vec{R}') \chi(\vec{k}, \vec{R}') d\vec{R}' \quad (3.30)$$

So, the scattering amplitude can have the form:

$$f(\theta, \phi) = -\frac{1}{4\pi} \int e^{-i\vec{k}' \cdot \vec{R}'} U(\vec{R}') \chi(\vec{k}, \vec{R}') d\vec{R}' \quad (3.31)$$

Now if the potential  $V$  is weak, one can approximate the above equation as:

$$f_{BA}(\theta, \phi) = -\frac{1}{4\pi} \int e^{-i\vec{k}' \cdot \vec{R}'} U(\vec{R}') e^{i\vec{k} \cdot \vec{R}'} d\vec{R}' \quad (3.32)$$

The above approximation is known as Born Approximation.

The Born Approximation is not true always for the real case as the interaction potential  $V$  consists of the potential due to elastic scattering part and non-elastic part. So it is better to write the potential  $U$  as a sum of  $U_1 + U_2$  and suppose we know the scattering solution for  $U_1$ , then one can write the above equation of scattering amplitude as:

$$f_{DWBA}(\theta, \phi) = f_1(\theta, \phi) - \frac{1}{4\pi} \int \langle \chi_1^{(-)}(\vec{k}', \vec{R}') | U_2(\vec{R}') | \chi_1^{(+)}(\vec{k}, \vec{R}) \rangle d\vec{R}' \quad (3.33)$$

This approximation can be generalized to inelastic and rearrangement collisions. If one chooses  $U_1$  as the potential for elastic scattering then  $f_1$  would be the elastic scattering amplitude,  $U_2$  would represent the interaction of non-elastic interaction. The validity of

the DWBA then depends upon elastic scattering which being the most important event so that other events can be treated as perturbation. Therefore, for a reaction  $A(a,b)B$  one can write the transition amplitude as:

$$f_{DWBA}(\theta, \phi) = -\frac{1}{4\pi} \int \langle \chi_{\beta}^{(-)}(\vec{k}_{\beta}, \vec{R}_{\beta}) | U_2^{\beta, \alpha} | \chi_{\alpha}^{(+)}(\vec{k}_{\alpha}, \vec{R}_{\alpha}) \rangle d\vec{R}_{\alpha} d\vec{R}_{\beta} \quad (3.34)$$

The function  $\chi_{\alpha}$  describes the elastic scattering in the  $\alpha = a + A$  entrance channel arising from an optical potential  $U_{\alpha}$ , while  $\chi_{\beta}$  describes the elastic scattering in the  $\beta = b + B$  exit channel emerging from the optical potential  $U_{\beta}$ . The potential  $U_{\beta}$  which causes the non-elastic transition depends upon the type of reaction and the model chosen to describe it.

The number of nodes  $N$  and orbital angular momentum  $L$  of the center of mass motion are related by the oscillatory energy relation by,  $2(N - 1) + L = \sum_{i=0}^{n_c} 2(n_i - 1) + l_i$ , where  $n_c$  is the number of particles in the cluster,  $(n_i, l_i)$  corresponds to the quantum numbers of the individual transferred nucleons. Then one can reconstruct the differential cross-section as:

$$\left( \frac{d\sigma}{d\Omega} \right)_{DWBA} = \frac{\mu_{\alpha} \mu_{\beta} K_{\beta}}{2\pi \hbar^2 K_{\alpha}} \frac{1}{(2J_a + 1)(2J_A + 1)} \sum |f_{DWBA}(\theta, \phi)|^2 \quad (3.35)$$

The equation 3.34 is a six dimensional numerical integral over  $R_{\alpha}$  and  $R_{\beta}$ . In case of zero range (ZR) approximation, the particle 'b' is assumed to be emitted at the same point at which particle 'a' is absorbed. The zero range approximation is valid only if the momentum ( $\Delta k$ ) carried by the transferred particle is too weak to give recoil momentum. The finite range (FR) approximation (six-dimensional integration) is more accurate. A comparison between the experimentally measured cross section and the calculated cross section using DWBA for a transfer reaction between two well-defined states gives 'Spectroscopic Factor' giving the structural information of the nucleus studied.

The experimental cross-section is related to theoretical cross-section by

$$\left(\frac{d\sigma}{d\Omega}\right)_{ex} = (C^2S)_1(C^2S)_2\left(\frac{d\sigma}{d\Omega}\right)_{DWBA} \quad (3.36)$$

where, the factors  $(C^2S)_1$  and  $(C^2S)_2$  describes the overlap of initial and final bound state wave functions in the projectile and target respectively. We have used the code FRESKO for finite range DWBA calculations.

### 3.4 Continuum Discretized Coupled Channels method

Now a days, the study of breakup reactions is very popular methods to get the cluster structural information of exotic nuclei. Because of multi-step effects the phenomenon of breakup can not be treated perturbatively. A non perturbative method that treats breakup to all orders, and includes Coulomb and nuclear effects on equal footing is the Continuum discretized coupled channel method (CDCC). From our knowledge of Quantum mechanics, it is known that the bound states are discrete, finite and normalizable whereas unbound states are continuous, infinite and non-normalizable. In order to get the solution for unbound states, one has to replace the true continuum by discretized continuum such that wave-function becomes normalizable.

This can be done by: (i) the inclusion of continuum in Coupled channel calculations. and, (ii) represent the continuum by a finite set of square-integrable states.

One of the most popular method of continuum discretization is the bin method, where square-integrable states are constructed from scattering states.

Let us consider a reaction  $p + t \rightarrow v + c + t$ , where an initial bound state of projectile  $p$  breaks into  $v$  and  $c$  under the influence of the target  $t$ . In Fig. 3.1 the relevant co-ordinates are  $(\vec{r}, \vec{R})$  the Jacobi co-ordinates, where,  $\vec{r}$  is a vector that connects the centre of mass

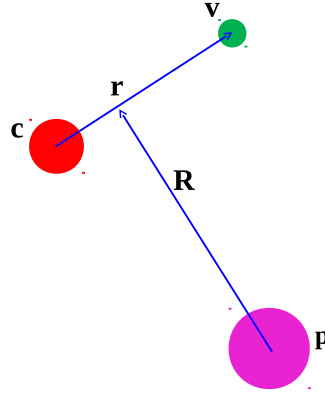


**Figure 3.1** Jacobi-Coordinate used in CDCC method.

between  $v$  and  $c$  and  $\vec{R}$  connects the centre mass of the target and  $(c + v)$  system.

The three body Hamiltonian can be written as:

$$H_{3b} = \hat{T}_r + \hat{T}_R + V_{vc} + V_{vt} + V_{ct} \quad (3.37)$$

Where,  $\hat{T}_r$  and  $\hat{T}_R$  are the kinetic energy operators.  $V_{vc}$  represents the binding potential between  $v$  and  $c$  and that describes the different scattering states of the projectile, hence  $V_{vc}$  is real. But as  $V_{vt}$  and  $V_{ct}$  represents the fragment-target interaction potential, hence they contain real as well as imaginary part.

The three body wave-function can be written as a superposition of bound state wave-function and continuum scattering wave-function:

$$\Psi_{K_0}^{(1)}(\vec{R}, \vec{r}') = \phi_0(\vec{r}')\chi_0(\vec{R}) + \int d\vec{k} \phi_{\vec{k}}(\vec{r}')\chi_{\vec{K}}(\vec{R}) \quad (3.38)$$

Where,  $\vec{k}$  is the momentum between the internal motion of  $(c + v)$  and it is related to the momentum  $\vec{K}$  between the projectile and the target through energy conservation.

As the three body wave-function involves an integral over a continuous variable to infin-

ity, as well as sums over angular momenta  $\int_0^\infty dk \sum_{l_s j_l c I_p} \dots$ , the solution of the Schrödinger equation is impractical. That's why discretization of continuum wave-function into a finite set of square integrable basis is required. In the average method, the radial functions for the continuum bins  $\tilde{u}_p(r)$  (with  $p \geq 1$ ), are a superposition of the scattering eigenstates within a bin  $[k_{p-1}, k_p]$ .

$$\tilde{u}_p(r) = \sqrt{\frac{2}{\pi N_p}} \int_{k_{p-1}}^{k_p} w_p(k) u_k(r) dk \quad (3.39)$$

Where,  $w_p(k)$  is the weight function and  $N_p$  is the normalization constant so chosen that  $\tilde{u}_p(r)$  form an orthonormal set.

Now the total wave-function can be written in terms of the wave-function of each bin:

$$\Psi(\vec{R}, \vec{r}') = \sum_{p=0}^N \tilde{\phi}_p(\vec{r}') \chi_p(\vec{R}) \quad (3.40)$$

where,  $p = 0$  refers to the bound state and  $p \geq 1$  represents the scattering states.

Now, one can solve Schrödinger wave-function and by using partial wave-decomposition and proper boundary condition will able to get the S-matrix elements. The cross-section for exclusive breakup channels can be obtained from the S-matrix elements.

The methods described in the above chapter have been used for the theoretical calculations in this thesis work.

# Chapter 4

## Direct, resonant and transfer breakup of ${}^6\text{Li}$

### 4.1 Introduction

The study of nuclear reactions involving weakly bound projectiles has been drawing tremendous interests due to the observation of many new features compared to the ones involving strongly bound projectiles. Suppression in complete fusion (CF) cross sections [40], breakup threshold anomaly in the optical potentials obtained from elastic scattering [41] and high yield in  $\alpha$  particle production [42] are some of the interesting features. The presence of projectile breakup channels in addition to other non-elastic channels and their coupling to the elastic channel are the prime factors behind the above differences. Several measurements in the literature have focused on identifying different breakup channels and estimating their cross sections.

In a systematic work by Pfeiffer *et al.* [43], it has been observed that the yield of  $\alpha$ -particles measured in reactions involving a  ${}^6\text{Li}$  beam with several targets ( ${}^{58}\text{Ni}$ ,  ${}^{118,120}\text{Sn}$ , and  ${}^{208}\text{Pb}$ ) is unexpectedly large and the production cross section at an energy normalized to the Coulomb barrier is independent of the target. The observation of smaller cross sec-

tions for deuteron compared to  $\alpha$  particles suggested the existence of other competing processes with  $\alpha$  particles in the exit channel, such as transfer reactions leading to  $\alpha$ -unstable  ${}^5\text{He}$  or  ${}^5\text{Li}$  or excitation of quasi-continuously neighbored states by multi-nucleon transfer. It was also concluded that these additional processes are more important at sub- and near-barrier energies than anticipated. Particle-particle correlation measurements in  ${}^6\text{Li}+{}^{208}\text{Pb}$  [44] and  ${}^6\text{Li}+{}^{118}\text{Sn},{}^{208}\text{Pb}$  [45] reactions at near barrier energies confirmed the presence of not only the direct breakup of  ${}^6\text{Li}\rightarrow\alpha+d$  but also the sequential breakup via one of its resonance states [i.e.,  ${}^6\text{Li}\rightarrow{}^6\text{Li}^*(3^+)\rightarrow\alpha+d$ ] and transfer induced breakup like  ${}^6\text{Li}\rightarrow{}^5\text{Li}\rightarrow\alpha+p$  and  ${}^6\text{Li}\rightarrow{}^8\text{Be}\rightarrow\alpha+\alpha$ . In a detailed investigation by Castaneda *et al.* for the  ${}^6\text{Li}+{}^{197}\text{Au}$  reaction [7], the sequential breakup via first resonant state of  ${}^6\text{Li}$  (i.e.,  $3^+$ , 2.18 MeV) and  $1n$  transfer followed by breakup (i.e.,  ${}^6\text{Li}\rightarrow{}^5\text{Li}\rightarrow\alpha+p$ ) was again observed. A similar observation was made by Signorini *et al.* [8,46] in  ${}^6\text{Li}+{}^{208}\text{Pb}$  reaction. In reactions  ${}^7\text{Li}+{}^{197}\text{Au}$  [47] and  ${}^7\text{Li}+{}^{65}\text{Cu}$  [6],  $1n$  stripping transfer followed by breakup of  ${}^6\text{Li}$  via its first resonance state ( $3^+$ , 2.18 MeV) was observed. While, in the case of the  ${}^6\text{Li}+{}^{65}\text{Cu}$  reaction [6], the breakup of  ${}^6\text{Li}$  via its first ( $3^+$ , 2.18 MeV) as well as second resonance ( $2^+$ , 4.31 MeV) states were observed. These studies show that the probability of breakup of the clustered projectiles or projectile like fragments such as  ${}^{6,7}\text{Li}$  into two or more fragments proceeding through their resonance states is quite large. Therefore, for the  ${}^6\text{Li}$  case, one can expect its breakup through all three resonance states corresponding to  $L=2$ , i.e., ( $3^+$ , 2.18 MeV), ( $2^+$ , 4.31 MeV) and ( $1^+$ , 5.65 MeV) [23,24].

So far there is no study available in the literature on the experimental breakup cross sections for  ${}^6\text{Li}$  via its  $1^+$  resonance state. Since the excitation energy and width of this state is very large the cross section is expected to be less compared to other two ( $2^+$  and  $3^+$ ) resonance states. Also, the relative energy of the breakup fragments proceeding via this resonance state being large (4.18 MeV) the detection cone angle is expected to be large requiring bigger detector system. However, it would be interesting and challenging to measure the breakup cross section via this state along with other two states using a

detector setup covering a large solid angle and find their relative contributions.

In a recent study on breakup reactions in  ${}^7\text{Li}+{}^{93}\text{Nb}$  system [48], at energies around the Coulomb barrier, the importance of transfer breakup, viz.  $1p$  pickup and  $1n$  stripping, to unbound states of the ejectile followed by its breakup compared to direct breakup of the projectile have been explored. In the measurements by Luong *et al.* [9] for  ${}^6\text{Li} + {}^{208}\text{Pb}, {}^{209}\text{Bi}$  reactions at sub-barrier energy it has been observed that the probability of  $1n$  transfer followed by breakup, i.e.,  ${}^6\text{Li} \rightarrow {}^5\text{Li} \rightarrow \alpha + p$ , is always greater than the inelastic breakup, i.e.,  ${}^6\text{Li} \rightarrow {}^6\text{Li}^*(3^+) \rightarrow \alpha + d$ , for both the reactions. These breakup phenomena can be further probed involving  ${}^6\text{Li}$  as a projectile with a different target ( ${}^{112}\text{Sn}$ ) to confirm the target independence if any. It would also be interesting to see the energy dependence of these breakup probabilities.

This chapter presents the results of exclusive measurements of different breakup channels in the  ${}^6\text{Li}+{}^{112}\text{Sn}$  reaction at two beam energies. Continuum-discretized-coupled-channels (CDCC) and coupled-reaction-channels (CRC) calculations are performed to understand the experimental cross sections for both direct as well as sequential breakup (through resonance states of  ${}^6\text{Li}$  and transfer reactions). Experimental and/or theoretical cross sections have been compared to disentangle the individual contributions to inclusive  $\alpha$  production and understand the underlying reaction mechanism.

## 4.2 Identification of breakup modes : Relative energy distribution

In the event by event mode off-line analysis, the coincidence yields in any two strips with  $\alpha$  particles in one strip and dominant fragments like deuteron or proton or  $\alpha$  particles in any other strip have been extracted independently by employing two-dimensional gates in respective particle bands obtained from the strip telescopes. The coincidence spectra have been built as a function of relative energies of two breakup fragments as defined in

Ref. [21] and shown in Fig. 4.1(a), (b) and (c) in order to find out excitation energies above the breakup threshold of the intermediate projectile like particles like  ${}^6\text{Li}$ ,  ${}^5\text{Li}$ ,  ${}^8\text{Be}$ , etc. The breakup yield of  ${}^6\text{Li} \rightarrow \alpha + d$  at  $E_{\text{beam}}=30$  MeV is found to peak at relative energies equal to excitations corresponding to the resonance states of  ${}^6\text{Li}$  (see Fig. 4.1 (a)). This confirms not only the dominance of sequential  $\alpha + d$  breakup but also the observation of breakup via the  $1^+$  resonance state of  ${}^6\text{Li}$  along with its  $3^+$  and  $2^+$  resonance states. For  ${}^6\text{Li} \rightarrow {}^5\text{Li} \rightarrow \alpha + p$  breakup, as shown in Fig. 4.1(b), the yield has a broad peak for  $\alpha + p$  relative energy  $E_{\alpha p} \sim 1.97$  MeV which is equal to the g.s.  $Q$ -value in  ${}^5\text{Li} \rightarrow \alpha + p$  breakup. In the case of  ${}^6\text{Li} \rightarrow {}^8\text{Be} \rightarrow \alpha + \alpha$  breakup, as shown in Fig. 4.1(c), the yield is maximum at  $E_{\alpha\alpha}=0.092$  MeV (the g.s.  $Q$ -value in  ${}^8\text{Be} \rightarrow \alpha + \alpha$  reaction). A small peak in the  $\alpha + \alpha$  breakup yield at  $E_{\alpha\alpha} \sim 3.2$  MeV corresponds to the excitation energy due to breakup via the first excited state ( $2^+$ ) of  ${}^8\text{Be}$ .

In order to find the beam energy dependence of the direct and sequential breakup contributions, the above measurements were repeated at another beam energy,  $E_{\text{beam}}=22$  MeV, around the Coulomb barrier. The relative energy spectra for  $\alpha + d$ ,  $\alpha + p$  and  $\alpha + \alpha$  breakup for both the beam energies i.e., 22 and 30 MeV, have been compared in Fig. 4.1. It is interesting to observe that the breakup of  ${}^6\text{Li} \rightarrow \alpha + d$  at  $E_{\text{beam}} = 22$  MeV now proceeds only through direct breakup. No sequential  $\alpha + d$  breakup peak is observed. This may be due to lower beam energy (22 MeV) which is slightly higher than the Coulomb barrier ( $V_b \sim 21$  MeV) but less than the breakup threshold. In the case of  $\alpha + p$  breakup, as shown in Fig. 4.1(b), the shapes of the relative energy spectra at two beam energies are similar, implying that this channel proceeds through the same ground states of  ${}^5\text{Li}$  at both energies. Finally, for the  $\alpha + \alpha$  case, as shown in Fig. 4.1(c), the breakup of  ${}^8\text{Be}$  at 22 MeV is found to proceed mainly through its ground state ( $0^+$ ). However, at 30 MeV, the breakup proceeds through both the ground state as well as the first excited state ( $2^+$ ) of  ${}^8\text{Be}$ .

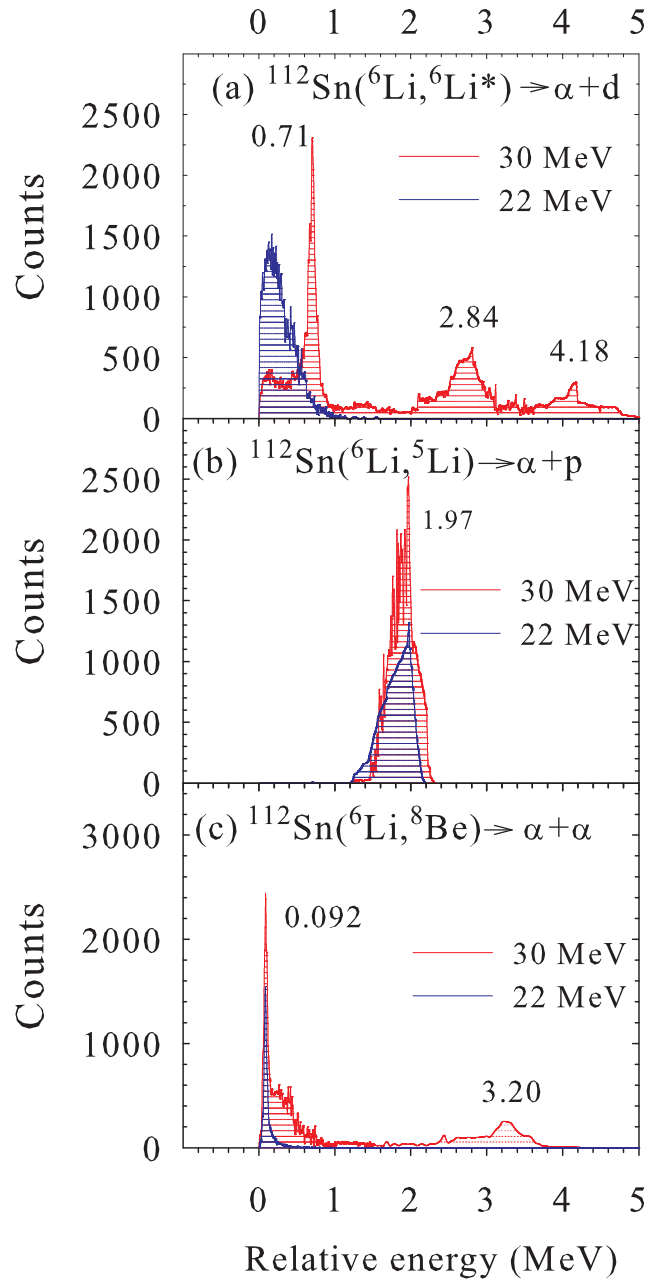


**Figure 4.1** Comparison of the yield distributions of  $\alpha - d$ ,  $\alpha - p$ , and  $\alpha - \alpha$  breakup as a function of relative energy at two different beam energies, i.e., 22 and 30 MeV.

## 4.3 Breakup cross sections

### 4.3.1 Determination of experimental breakup cross-section from coincidence spectra

Experimental cross sections for the breakup channels were obtained by strictly following the formulations described in the review article by R. J. de Meijer and R. Kamermans, [21] and the article by H. Fuchs, Nucl. Instrum. Methods [49]. The generalized expression for cross section in center-of-mass frame can be obtained as follows.

Consider the breakup reactions,



as well as,



Where, ‘a’ is the weakly bound nucleus ( ${}^6\text{Li}$ ) and ‘A’ is the target nucleus ( ${}^{112}\text{Sn}$ ). The projectile ‘a’ while moving in the field (Coulomb as well as nuclear) of the target may either directly break into fragments ‘1’ and ‘2’ or before breaking, it may either get excited to some resonant state  $12^*$ , or exchange nucleon(s) with the target. The nucleus ‘3’ is the corresponding residual in each case.

When a particle is detected in a detector of solid angle  $d\Omega$  in singles mode, then the yield (count) corresponding to the particle energy in the range of  $E$  and  $E + dE$  can be obtained using the relation,

$$Y_{\text{coin}} = N_p N_t \frac{d^2\sigma}{d\Omega dE} d\Omega dE \quad (4.3)$$

Where,  $N_p$  is the total no. of incident projectiles,  $N_t$  is no. of target nuclei/unit area and  $\frac{d^2\sigma}{d\Omega dE}$  represents the double differential breakup cross-section in the lab frame. The

energy bin for these spectra is denoted by  $dE$ .

When two particles ‘1’ and ‘2’ are detected at detector ‘ $D_1$ ’ and ‘ $D_2$ ’ of solid angles  $d\Omega_1$  and  $d\Omega_2$ , respectively in coincidence, then the coincidence yield corresponding to the fragment particle energy between  $E_i$  and  $E_i + dE_i$ , where  $i=1$  or  $2$ , can be written as,

$$Y_{coin} = N_p N_t \frac{d^3\sigma}{d\Omega_1 d\Omega_2 dE_i} d\Omega_1 d\Omega_2 dE_i \quad (4.4)$$

where,  $\frac{d^3\sigma}{d\Omega_1 d\Omega_2 dE_i} d\Omega_1 d\Omega_2 dE_i$  represents the triple differential breakup cross-section in the lab frame. The energy bin for these spectra is denoted by  $dE_i$ . In our calculation the bin size ( $dE_1 = dE_\alpha$ ) was taken to be 60 KeV.

As usual, the values of  $N_p N_t$  can be found from the yield of the monitor detector M which is fixed at an angle  $\theta_M = 20^\circ$  in the present case. The monitor yield  $Y_M$  is given by the relation

$$Y_M = N_p N_t \frac{d\sigma^{ruth}}{d\Omega_M} d\Omega_M \quad (4.5)$$

where,  $d\Omega_M$  represents the solid angle subtended by the monitor and  $\frac{d\sigma^{Ruth}}{d\Omega_M}$  is the differential cross-section for Rutherford scattering at given  $\theta_M$  which is calculated from the following relations:

$$\frac{d\sigma^{Ruth}}{d\Omega_M} = \left( \frac{Z_p Z_t e^2}{4E} \right)^2 \frac{1}{\sin^4 \left( \frac{\theta_M}{2} \right)} \quad (4.6)$$

Therefore, one can find out the triple differential breakup cross-section in lab frame using the Equations 4.4 and 4.5.

$$\frac{d^3\sigma}{d\Omega_1 d\Omega_2 dE_i} = \frac{Y_{coin}}{Y_M} \frac{d\sigma^{ruth}}{d\Omega_M} \frac{d\Omega_M}{d\Omega_1 d\Omega_2 dE_i} \quad (4.7)$$

This is the general procedure to convert raw spectrum of ‘coincident counts versus energy’ into absolute triple differential cross section in terms of ‘ $\frac{d^3\sigma}{d\Omega_1 d\Omega_2 dE_i}$ ’ in laboratory frame at a particular detector angle.

Now, the above laboratory cross-section is transformed into center-of-mass frame using the formula as described in Ref. [21] ,

$$\frac{d^3\sigma}{d\Omega_1 d\Omega_2 dE_1} = J \frac{d^3\sigma}{d\Omega_{3-12} d\Omega_{1-2} d\epsilon} \quad (4.8)$$

Where  $d\Omega_{1-2}$  is the solid angle of the relative motion of fragments ‘1’ and ‘2’ with respect to their center-of-mass and  $d\Omega_{3-12}$  the solid angle for the center-of-mass system ‘12’, with respect to the center-of-mass system ‘123’ of the total reaction.

Here,  $d\epsilon$  represents the differential of the relative energy ( $\epsilon$ ) between breakup fragments ‘1’ and ‘2’.

The Jacobian for this transformation is given by Fuchs [49] ,

$$J = \frac{\partial(\Omega_{3-12}, \Omega_{1-2}, \epsilon)}{\partial(\Omega_1, \Omega_2, E_1)} = \frac{J_1}{J_2} \quad (4.9)$$

where,

$$J_1 = \frac{m_1 m_2 m_3 p_1 p_2}{\mu_{1-2} \mu_{3-12} p_{1-2} p_{3-12}} \quad (4.10)$$

and,

$$J_2 = m_2 + m_3 + m_2 (\vec{p}_1 - \vec{P}) \cdot \frac{\vec{p}_2}{p_2^2} \quad (4.11)$$

Here,  $\mu_{1-2}$  and  $\mu_{3-12}$  are the reduced masses and  $p_{12}$ ,  $p_{3-12}$  are the associated momenta for 1-2 and 3-12 systems respectively,  $p_1$  and  $p_2$  are the momenta associated with the breakup fragments ‘1’ and ‘2’ respectively and  $\vec{P}$  is the total momentum. Assuming the isotropic emission of breakup fragments in their own center of mass system, eqn. 4.8 leads to

$$\frac{d^2\sigma}{d\Omega_{3-12} d\epsilon} = \frac{4\pi}{J} \frac{d^3\sigma}{d\Omega_1 d\Omega_2 dE_1} \quad (4.12)$$

The desired breakup cross section in the center-of-mass frame can now be obtained as

(see Eqn (2.14) of Ref. [21]),

$$\frac{d\sigma}{d\Omega_{3-12}} = \int_{\epsilon_1}^{\epsilon_2} \frac{4\pi}{J} \frac{d^3\sigma}{d\Omega_1 d\Omega_2 dE_1} d\epsilon \quad (4.13)$$

where,  $\epsilon_1$  and  $\epsilon_2$  are, respectively, the lower limit and the higher limit of the desired relative energy range for a particular breakup process, e.g. for the  $3^+$  resonant state of  ${}^6\text{Li}$  (breakup into  $\alpha + d$ ) with relative energy peak at 0.71 MeV, the lower limit is chosen as  $\epsilon_1$  as 0.65 MeV and the higher limit  $\epsilon_2$  as 0.75 MeV, in accordance with experimental observation.

### 4.3.2 Reconstruction of emission angle of projectile like fragment

Once the energy and angle information of the breakup fragments are known, then one can reconstruct the emission angle of projectile like fragment from the following relations:

$$\theta_{lab} = \tan^{-1} \left( \frac{\theta_a}{\theta_b} \right) \quad (4.14)$$

Where,

$$\theta_a = p_1 \sin(\theta_1) + p_2 \sin(\theta_2) \quad (4.15)$$

and,

$$\theta_b = p_1 \cos(\theta_1) + p_2 \cos(\theta_2) \quad (4.16)$$

Where,  $p_1$  and  $p_2$  are the momentum associated with breakup fragments '1' and '2' respectively and  $\theta_1$  and  $\theta_2$  are the azimuthal angle of the fragments.

Now  $\theta_{cm}$  can be converted from  $\theta_{lab}$  from the following relation:

$$\theta_{cm} = \theta_{lab} + \sin^{-1}(x \sin(\theta_{lab})) \quad (4.17)$$

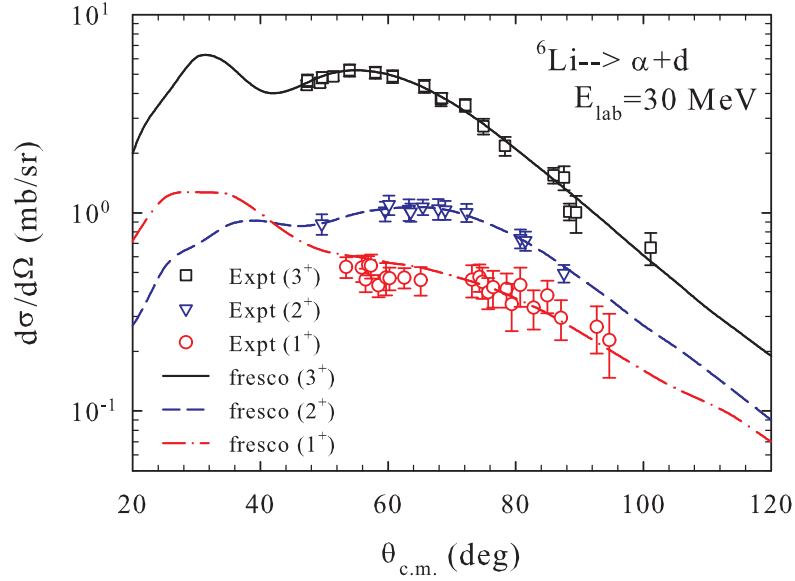


**Figure 4.2** Sequential  $\alpha + d$  breakup cross section in center-of-mass frame measured at 30 MeV.

where,  $x = \sqrt{\frac{m_a m_{12}}{m_A m_3} \frac{E_{cm}}{E_{cm} + Q}}$ .  $E_{cm}$  is the center of mass energy and  $Q$  represents the total reaction Q-Value.

### 4.3.3 Direct and Resonant breakup of ${}^6\text{Li} \rightarrow \alpha + d$

Similar to the observation earlier [5], the yields of the two peaks [7, 45] corresponding to the sequential  $\alpha + d$  breakup through a particular resonance state of  ${}^6\text{Li}^*$  are also found to be asymmetric for the present reaction. The  $\alpha$ - $d$  coincidence yields under the two peaks corresponding to the same relative energy have been used separately to calculate the differential breakup cross sections in the center-of-mass system at various angles using the formulation discussed above. The two peaks in each of  $\alpha$  or  $d$  coincident spectra correspond to two center-of-mass angles of  ${}^6\text{Li}^*$  [7, 45] which are slightly different in the case of  $3^+$  and  $2^+$  resonant breakup. An average of the cross sections obtained from the two (low and high energy) peaks of particular coincidence spectrum has been obtained for each of  $3^+$  and  $2^+$  breakup and the results are shown in Fig. 4.2.

However, for  $1^+$  breakup, the cross sections obtained for each of the two coincidence peaks have been plotted independently as the difference in center-of-mass angles corresponding to two peaks is large ( $12^\circ$ - $22^\circ$ ). Differential cross sections for sequential  $\alpha+d$  breakup via  $3^+$ ,  $2^+$ , and  $1^+$  resonances shown in Fig. 4.2 are represented by squares, triangles, and circles, respectively. Although the resonant breakup cross sections via  $3^+$  and  $2^+$  states of  ${}^6\text{Li}$  in reactions involving a few targets have been measured and described earlier, the cross section for  $1^+$  state is measured for the first time in the present reaction. The lines plotted in the above figure, representing theoretical calculations as described in chapter 3, explain the experimental cross sections very well and thus support the observation of above resonant breakups.

Using the same formulation and assuming isotropic emissions of the fragments, the experimental differential cross sections for direct breakup of  ${}^6\text{Li} \rightarrow \alpha + d$  have been extracted and shown in Fig. 4.3(a) and (b).

At  $E_{\text{beam}} = 30$  MeV, the coincident  $\alpha + d$  breakup yields with relative energies in the range of  $E_{\alpha d} = 0 - 2$  MeV, excluding the contributions of sequential breakup of the resonant states, are used. For  $E_{\text{beam}} = 22$  MeV, no significant contribution from the resonant states has been observed experimentally. So, the  $\alpha + d$  breakup yields covering the measured range of relative energies i.e.,  $E_{\alpha d} = 0$  to 1.4 MeV, have been considered for direct breakup cross section estimations. The results of FRESKO calculations including projectile inelastic excitations up to the same limit as measured in the experiment, represented by solid lines, explain the experimental data very well. Calculations for direct breakup with  $\alpha d$  excitations up to a maximum of 8 MeV which is included in full CDCC calculations are represented by dashed lines for both beam energies. The elastic scattering cross sections calculated simultaneously using the same cluster-folded potential with breakup couplings, represented by dash-dotted lines are also compared with the experimental data (diamonds) in Fig. 4.3(c) and (d) for 30 and 22 MeV respectively.

The CDCC method was used to calculate the cross sections for elastic and breakup

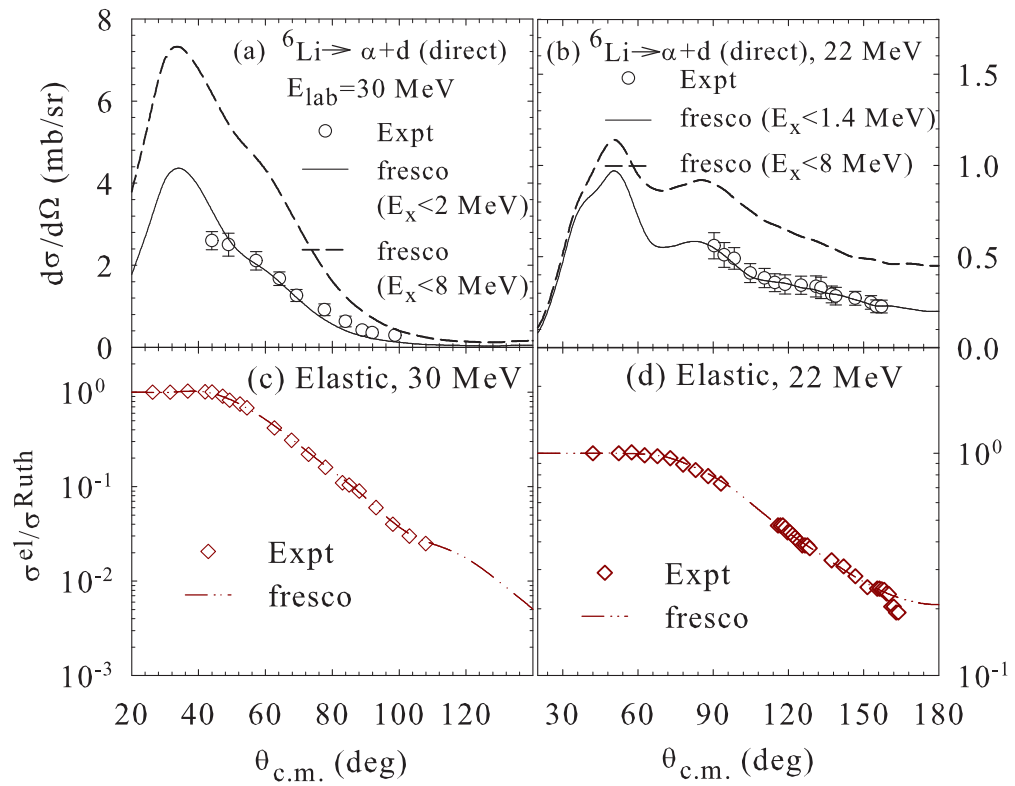


**Figure 4.3** Differential cross sections for direct breakup of  ${}^6\text{Li} \rightarrow \alpha + d$  in center-of-mass frame measured at  $E_{\text{beam}}$  of (a) 30 MeV and (b) 22 MeV. Corresponding experimental elastic scattering angular distribution (diamonds) along with the results of CDCC calculations (dash-dot-dotted lines) are shown in (c) and (d).

channels with the code FRESKO [50].  ${}^6\text{Li}$  was taken as a cluster of  $\alpha + d$  for its bound as well as continuum states. The breakup of the projectile into its fragments ( $\alpha$  and  $d$ ) is considered to be caused by inelastic excitations to different partial waves in the continuum, induced by interactions of the projectile fragments with the target by Coulomb as well as nuclear forces. For  ${}^6\text{Li}$ , couplings to the  $3^+$  (Ex = 2.18 MeV),  $2^+$  (Ex = 4.31 MeV), and  $1^+$  (Ex = 5.65 MeV) resonant states as well as couplings to the non-resonant continuum were included. The continuum up to an excitation energy of 8 MeV with  $\alpha d$  relative momentum  $L = 0, 1$  and  $2$  was included in the coupling. For  $s$  and  $p$  waves, the continuum was discretized into 10 bins of equal width in the energy of  $\alpha d$  relative motion. In the presence of resonances for  $d$ -waves, the discretization of the continuum was slightly modified in order to avoid double counting. Three resonant states, with widths corresponding to 0.1 MeV, 2.0 MeV and 3.0 MeV, respectively, were also treated as energy bins, but with finer steps.

The couplings of the ground state to the continuum as well as continuum to continuum have been included. Reorientation coupling, i.e., the coupling of the quadrupole term of the projectile fragment-target potentials was also incorporated. No target excitation was included in the CDCC calculation.

The CDCC calculations were performed using cluster-folded (CF) interaction [51], where  $\alpha$ -target ( $V_{\alpha+S_n}$ ) and deuteron-target ( $V_{d+S_n}$ ) optical potentials were evaluated at  $E_\alpha \approx \frac{2}{3}E_{6\text{Li}}$  and  $E_d \approx \frac{1}{3}E_{6\text{Li}}$  respectively. Once a certain set of potential parameters for  $V_{\alpha+S_n}$  and  $V_{d+S_n}$  are chosen, there is no free parameter remaining in the model, except a possible overall renormalization factor. The cluster-folded (CF) interaction with  $V_{\alpha+S_n}$  potential from [52] at  $E_{beam} = 19.5$  MeV and  $V_{d+S_n}$  potential at  $E_{beam} = 10$  MeV from the global fit [53] have been used. The real part of the of ( $\alpha+S_n$ ) potential have the Woods-Saxon volume form and the parameters are:  $v_0 = 163.30$  MeV,  $r_0 = 1.281$  fm,  $a_0 = 0.664$  fm, and the imaginary part have both the volume and surface term and the parameters are :  $w=9.70$  MeV,  $r_w=1.57$  fm,  $a_w=0.618$  fm and  $W_d=8.00$  MeV,  $r_d=1.49$  fm,

$a_d=0.372$  fm. Similarly, for  $V_{d+S_n}$  potential, with real parameters are  $v_0 = 96.136$  MeV,  $r_0 = 1.1530$  fm,  $a_0 = 0.7780$  fm, and the surface imaginary parameters are  $w_d = 10.524$  MeV,  $r_d = 1.366$  fm,  $a_d = 0.825$  fm. The spin-orbit potential also have the Woods-Saxon form, the parameters are:  $V_{s.o.}=3.557$ ,  $r_{s.o.}=0.972$  and  $a_{s.o.}=1.011$ .

The  $\alpha + d$  binding potential in  ${}^6\text{Li}$  was also of Woods-Saxon shape and the parameters were taken from [23]. The  $\alpha - d$  binding potential parameters are:  $V_{\alpha+d}=78.46$  MeV,  $r_0=1.15$  fm,  $a_0= 0.7$  fm for the g.s and for the continuum the depth of the potential is suitably modified to 80.0 MeV to reproduce the resonances. The  $\alpha - d$  spin orbit interaction potential are  $V_{s.o.}=2.5$  MeV,  $r_{s.o.}=1.15$  fm and  $a_{s.o.}=0.7$  fm. Results of the CDCC calculations for two beam energies, 30 and 22 MeV, are shown in Figs. 4.2 and 4.3. In Figs. 4.3(c) and 4.3(d), the calculated elastic scattering angular distributions (lines) reproduce the experimental data (diamonds) well. The breakup cross sections calculated for three resonant states ( $3^+$ ,  $2^+$ , and  $1^+$ ) shown, respectively, as solid, dashed, and dash-dotted lines in Fig. 4.2 explain the experimental data very well.

#### 4.3.4 Transfer breakup

As observed in Fig. 4.1, the two major channels of transfer reactions followed by breakup are  ${}^6\text{Li} \rightarrow {}^5\text{Li} \rightarrow \alpha + p$  and  ${}^6\text{Li} \rightarrow {}^8\text{Be} \rightarrow \alpha + \alpha$ . The yields in  $\alpha$ - $p$  and  $\alpha$ - $\alpha$  coincidences are of the same order as that of  $\alpha$ - $d$  coincidence for any particular energy. Thus these two breakup channels along with the  $\alpha + d$  channel are expected to have significant contributions to the total alpha particle production in the reaction. Assuming isotropic emission of the breakup fragments in the center-of-mass frame and using the formulation of Ref. [21], experimental cross sections for  $\alpha + p$  and  $\alpha + \alpha$  breakup have been extracted and shown in Fig. 4.4(a) and (b) respectively.

Coupled reaction channels (CRC) calculations using FRESKO for  $1n$  stripping and  $1d$  pickup reactions have been compared with the measured  $\alpha + p$  and  $\alpha + \alpha$  breakup cross sections. The ejectiles  ${}^5\text{Li}$  and  ${}^8\text{Be}$  formed in the above transfer reactions being unstable

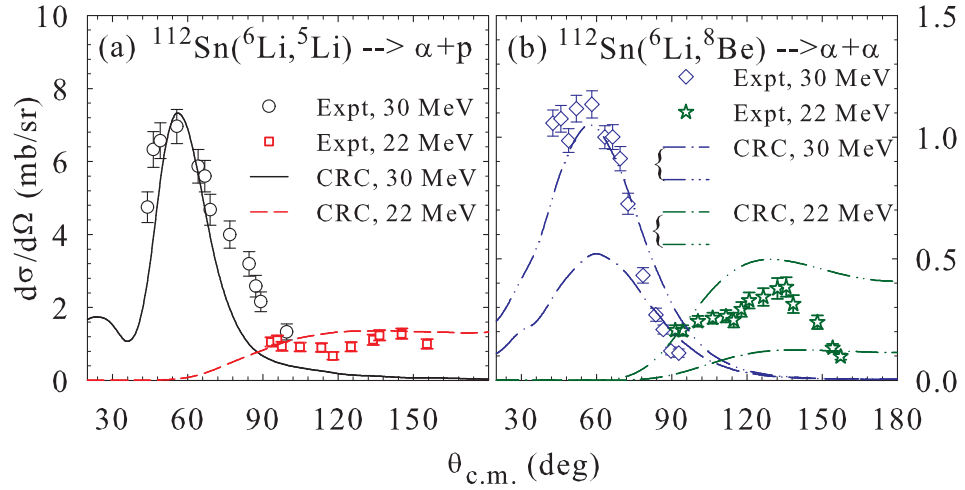


**Figure 4.4** Differential cross sections in center-of-mass frame for sequential breakup of (a)  ${}^6\text{Li} \rightarrow {}^5\text{Li} \rightarrow \alpha + p$ , and (b)  ${}^6\text{Li} \rightarrow {}^8\text{Be} \rightarrow \alpha + \alpha$  measured at  $E_{\text{beam}} = 30$  MeV and 22 MeV. Lines represent CRC calculations.

to the above breakup channels, the transfer cross sections are assumed to be equal to breakup cross sections. For the entrance and exit channels of CRC calculations, the real potential obtained from the fit to measured elastic scattering was used. But the imaginary potentials were of short range and Woods-Saxon square form. In the case of the  $1n$  stripping reaction, the ground state of  ${}^5\text{Li}$  and ground plus six excited states of  ${}^{113}\text{Sn}$  have been included. Spectroscopic factors for  $\langle {}^{112}\text{Sn}+n | {}^{113}\text{Sn} \rangle$  corresponding to seven states ( $E_x = 0 - 1.556$  MeV) of  ${}^{113}\text{Sn}$  are taken from Ref. [54]. Spectroscopic factors for  $\langle {}^6\text{Li} | {}^5\text{Li}+n \rangle$  is assumed to be 0.56 to reproduce the experimental data. Results are shown in Fig. 4.4(a) as solid and dashed lines corresponding to 30 and 22 MeV respectively. In the case of the  $1d$  pickup reaction, the possibility of both single step transfer as well as double step ( $1p$  followed by  $1n$  or vice-versa) transfers have been considered. The  $0^+$  and  $2^+$  state of  ${}^8\text{Be}$  and ground plus first two excited states of  ${}^{110}\text{In}$  have been coupled. These are only a few representative states out of many excitations of  ${}^{110}\text{In}$ . Spectroscopic factors for  $\langle {}^6\text{Li}+p | {}^7\text{Be} \rangle$  are taken to be the same as  $\langle {}^6\text{Li}+n | {}^7\text{Li} \rangle$  [55] and those for  $\langle {}^{111}\text{Sn}+n | {}^{112}\text{Sn} \rangle$  are taken from Ref. [56]. The other overlaps which are not available

**Table 4.1** Experimental and calculated cross sections for various channels at  $E_{\text{beam}} = 30$  and 22 MeV.

Reaction channel	$\sigma_{30}(\text{mb})$		$\sigma_{22}(\text{mb})$	
	(expt.)	(theory)	(expt.)	(theory)
Inclusive breakup- $\alpha$	$592 \pm 35$	-	$309 \pm 16$	-
${}^6\text{Li}^* \rightarrow \alpha + d$ (resonant)	$34 \pm 4$	34.6	-	15.2
${}^6\text{Li} \rightarrow \alpha + d$ (direct)	$12 \pm 2.0^a$	$12^a$	$6 \pm 1^b$	$6.1^b$
	-	$25.9^c$	-	$9.3^c$
${}^6\text{Li} \rightarrow \alpha + d$ (total)	$46 \pm 4.5$	60.5	$6 \pm 1^b$	24.5
${}^6\text{Li}^* \rightarrow {}^5\text{Li} \rightarrow \alpha + p$	$28.1 \pm 4.0$	19.2	$6.8 \pm 1.0$	7.9
${}^6\text{Li}^* \rightarrow {}^8\text{Be} \rightarrow \alpha + \alpha$	$4.2 \pm 0.8$	4.79	$2.3 \pm 0.5$	2.75
Reaction	$1364 \pm 20$	1344	$521 \pm 15$	493

in the literature are assumed to be 1.0. Calculated cross sections with only g.s. (dash-dot line) and ground plus excited states of  ${}^{110}\text{In}$  (dash-dot-dot line) shown in Fig. 4.4(b) reproduce the peak positions of the experimental data.

## 4.4 Summary and conclusions

In summary, the major projectile-breakup channels observed in the  ${}^6\text{Li} + {}^{112}\text{Sn}$  reaction at  $E_{\text{beam}} = 30$  and 22 MeV are (i) direct and sequential breakup of  ${}^6\text{Li} \rightarrow \alpha + d$ , (ii) sequential breakup via  $1n$  stripping followed by breakup into  $\alpha + p$ , and (iii) sequential breakup via  $1d$  pickup followed by breakup into  $\alpha + \alpha$  [57]. Sequential  $\alpha + d$  breakup cross sections of  ${}^6\text{Li}$  via its resonant state ‘ $1^+$ ’ along with ‘ $2^+$ ’, and ‘ $3^+$ ’ in the continuum have been measured for the first time. Breakup via the  $3^+$  state of  ${}^6\text{Li}$  in the continuum, dominates the total  $\alpha + d$  breakup cross section at  $E_{\text{beam}} = 30$  MeV. However, at  $E_{\text{beam}} = 22$  MeV, only direct breakup of  ${}^6\text{Li}$  into  $\alpha + d$  is observed. The breakup channels proceeding via  $1n$  and  $1d$  transfer reactions are observed at both the energies. The relative energy spectra show that  $\alpha + p$  breakup proceeds via the same excitations at both the beam energies. However, for the  $\alpha + \alpha$  channel, the breakup at  $E_{\text{beam}} = 22$  MeV proceeds only through the  $0^+$  state of  ${}^8\text{Be}$  whereas at  $E_{\text{beam}} = 30$  MeV it proceeds through both  $0^+$  and  $2^+$  states of  ${}^8\text{Be}$ . Excellent agreement between CDCC calculations and experimental  $\alpha + d$

breakup cross sections via three resonance states of  ${}^6\text{Li}$  further confirms the observation of sequential breakup via the resonance state of  $1^+$  along with  $3^+$  and  $2^+$  states. A comparison of breakup cross sections at two energies reveals that the cross sections for  $\alpha+d$  breakup are more than  $\alpha+p$  as well as  $\alpha+\alpha$  breakup at above barrier energies but at around barrier, the cross-sections are of similar order. All the breakup channels observed in the present measurements produce  $\alpha$  as one of the two fragments and contribute to total inclusive  $\alpha$  yield. Two additional channels, i.e.,  $\alpha+d$  breakup followed by  $d$  capture and  $1p$  transfer followed by  $\alpha+n$  breakup are expected to have significant contributions in inclusive  $\alpha$ .

The elaborate set of experimental data and theoretical calculations presented here on different breakup channels including the newly found resonant breakup via  $1^+$  state provides a deep insight of the reaction mechanisms involving a weakly bound projectile like  ${}^6\text{Li}$ . Understanding the above reaction mechanisms is an important step in exploring similar reactions involving light radioactive ion beams from upcoming facilities.

# Chapter 5

## Direct, resonant and transfer breakup of ${}^7\text{Li}$

### 5.1 Introduction

In the previous chapter, a systematic measurement on direct as well as sequential breakup cross sections for different outgoing channels in a reaction involving  ${}^6\text{Li}$  with a medium mass target  ${}^{112}\text{Sn}$  are discussed. In addition to several well known breakup channels, a new breakup channel for  ${}^6\text{Li}$  breaking into  $\alpha$  and  $d$  via its third resonance state ( $1^+$ , 5.65 MeV) was observed [57]. The use of large detector array with wide angular coverage has made it possible to measure the higher resonance states. With similar motivations and using even a bigger detector array, a reaction involving the same  ${}^{112}\text{Sn}$  target but with a different weakly bound projectile i.e.,  ${}^7\text{Li}$  was chosen for the present work.

The cluster structure of a light nuclei plays an important role in predicting possible breakup channels. The  ${}^7\text{Li}$  as a cluster of  $\alpha$  and  $t$  with a binding energy of only 2.47 MeV is very well known. Direct breakup of  ${}^7\text{Li}$  into  $\alpha + t$  and sequential breakup via the first resonance state ( $7/2^-$ , 4.63 MeV) of the cluster have been measured for several systems. But, there is no measurement available on the sequential breakup corresponding

to the second resonance state ( $5/2^-$ , 6.68 MeV). The study of this state is however very important as various studies on elastic scattering show a significant effect of coupling of the  $5/2^-$  state of  ${}^7\text{Li}$  [25, 26]. So, it would be interesting to measure this new channel to better understand the mechanism of  $\alpha + t$  resonance breakup.

Cluster models of the structure of the light nuclei frequently provide a rather simple description of some of the energy levels which are difficult to access in the usual shell model framework. The model described in Ref. [27] is used to study the low-lying energy levels of  ${}^7\text{Li}$ , whose structure is treated as a superposition of the clusters ' $\alpha+t$ ' and ' ${}^6\text{Li}+n$ ' with binding energies of 2.47 and 7.25 MeV respectively. Other possible cluster structures like  ${}^6\text{He} + p$  were not considered because of its high binding energy ( $\sim 9.96$  MeV). Investigation of the breakup channel  ${}^7\text{Li} \rightarrow {}^6\text{He} + p$  will shed light on the possibility of an additional cluster structure of  ${}^7\text{Li}$ .

In addition, the transfer breakup channels are known [42] to play a very important role in understanding the large cross sections for inclusive  $\alpha$  particles. Apart from  $\alpha + t$  breakup, the  $\alpha$  particles can be produced in several sequential breakup, mainly the transfer followed by breakup, reactions. For example, the transfer reactions of  $1n$  stripping ( ${}^7\text{Li}, {}^6\text{Li}$ ),  $2n$  stripping ( ${}^7\text{Li}, {}^5\text{Li}$ ),  $1p$  pickup ( ${}^7\text{Li}, {}^8\text{Be}$ ) and  $1d$  stripping ( ${}^7\text{Li}, {}^5\text{He}$ ) followed by breakup into  $\alpha + d$ ,  $\alpha + p$ ,  $\alpha + \alpha$  and  $\alpha + n$  can contribute individually to the inclusive alpha production. The importance of the  $2\alpha$  cluster structure of  ${}^8\text{Be}$  at its ground state ( $0^+$ ) as well as other two resonance states at 3.12 MeV ( $2^+$ ) and 11.35 MeV ( $4^+$ ) is well reflected by the values of the spectroscopic factors for  $\langle {}^8\text{Be} | \alpha + \alpha \rangle$  overlaps:  $S(\text{g.s.})=0.84$ ,  $S(2^+)=0.83$ , and  $S(4^+)=0.75$  [28]. Since the third resonance state ( $4^+$ ), like other two states, has a good overlap between two  $\alpha$ -particles in the cluster [29], the breakup of  ${}^8\text{Be}$  into two  $\alpha$  via this state is also possible at favorable excitation energies. However, there is no experimental evidence reported so far on the observation of  ${}^8\text{Be}$  breakup via the  $4^+$  resonance state. So it would be interesting to investigate experimentally the existence of  ${}^8\text{Be}$  breakup via its third resonance state and compare with the breakup probabilities via

its  $0^+$  and  $2^+$  states. Secondly, if the breakup via  $4^+$  state exists, finding its proximity to the target nucleus at the time of dissociation would be important to understand its effect on complete and incomplete fusion cross sections.

In this chapter, the results of experimental investigation on the existence of (i)  ${}^7\text{Li}$  breakup into  $\alpha+t$  via its second as well as first resonance state along with its direct breakup and (ii) the direct breakup  ${}^7\text{Li}$  into  ${}^6\text{He}+p$  are discussed. In addition, the breakup induced by (i)  $+1p$  transfer channel i.e.,  ${}^7\text{Li} \xrightarrow{+1p} {}^8\text{Be} \rightarrow \alpha + \alpha$  breakup via three resonance states of  ${}^8\text{Be}$ , (ii)  $-1n$  transfer channel i.e.,  ${}^7\text{Li} \xrightarrow{-1n} {}^6\text{Li} \rightarrow \alpha + d$  breakup via three resonance states of  ${}^6\text{Li}$  and (iii)  $-2n$  transfer channel i.e.,  ${}^7\text{Li} \xrightarrow{-2n} {}^5\text{Li} \rightarrow \alpha + p$  breakup are also investigated. Experimental differential cross sections for the above breakup channels have been compared with the results of coupled-channels calculations.

## 5.2 Identification of breakup modes

### 5.2.1 Relative energy distributions

The relative energy ' $E_{rel}$ ' of two breakup fragments and 'Q-value' of each reaction event were reconstructed using the measured energies and positions of two breakup fragments. The corresponding efficiencies of the detector array have been obtained by a Monte-Carlo simulation. The relative energy distribution between two breakup fragments infer about the excitation energy of the projectile-like nuclei above their break-up threshold through which the breakup occurs. The relative energy between the fragments of masses  $m_1$  and  $m_2$  has been calculated from their individual energies  $E_1$  and  $E_2$  and the opening angle of their velocity vectors  $\theta_{12}$ , using the expression given in Ref. [21].

Monte Carlo simulations have been performed to find the efficiency of detecting two breakup fragments detected in coincidence by any two strips of the present strip detector array as a function of  $E_{rel}$ . The breakup fragments were assumed to be emitted isotropically in the rest frame of outgoing cluster particle which was broken. In simula-

tion, the events with two breakup fragments falling on the same strip has been rejected. The relative energy and efficiency of the detector have been determined event by event. This efficiency distribution was applied to the raw data to obtain the efficiency corrected relative energy distribution.

For  ${}^7\text{Li}$  breaking into  $\alpha$  and  $t$ , the relative energy distribution without efficiency correction, the relative energy dependent efficiency of the detector array and the relative energy distribution with efficiency correction have been shown in Fig. 5.1(a), (b) and (c) respectively. In the relative energy distribution of  $\alpha + t$  breakup, it is interesting to observe that, in addition to the direct breakup at low energy, there are two dominant peaks at  $\sim 2.23$  and  $\sim 4.28$  MeV which correspond to first and second resonance states at  $7/2^-$  (4.63 MeV) and  $5/2^-$  (6.67 MeV) respectively. The comparison of the peak positions and widths of resonance states with literature values in Table 5.1 actually confirms the observation of  ${}^7\text{Li}$  breakup into  $\alpha + t$  via its  $5/2^-$  resonance state for the first time along with  $7/2^-$  resonance and direct breakup [58]. Similarly, the relative energy, efficiency and efficiency corrected relative energy for  $\alpha + \alpha$  is displayed in Fig. 5.2(a),(b) and (c) respectively. It is observed from the efficiency corrected relative energy distribution that the breakup yields of  ${}^8\text{Be} \rightarrow \alpha + \alpha$  peaks around 0.09 MeV, 3.5 MeV and 11.3 MeV corresponding to  $0^+$ ,  $2^+$  and  $4^+$  states of  ${}^8\text{Be}$  respectively. The observed peak positions and widths of all the three resonances ( $0^+$ ,  $2^+$  and  $4^+$ ) obtained by Gaussian fits (dotted lines) are in reasonable agreement with the ones from the literature values [59] as compared in Table 5.1. Although the breakup modes of  ${}^8\text{Be}$  through its  $0^+$  and  $2^+$  states were observed [57, 60], the breakup via its  $4^+$  resonance state is observed for the first time in the present measurement [61].

Using the same procedure as above, the efficiency corrected relative energy distributions have been obtained for  $\alpha + d$ ,  $\alpha + p$  and  ${}^6\text{He} + p$  breakup as shown in Fig. 5.3(a), (b) and (c) respectively. It can be observed that the probability of  $1n$  stripping followed by breakup i.e.,  ${}^7\text{Li} \xrightarrow{-1n} {}^6\text{Li} \rightarrow \alpha + d$ , the breakup mainly proceeded with three relative energies

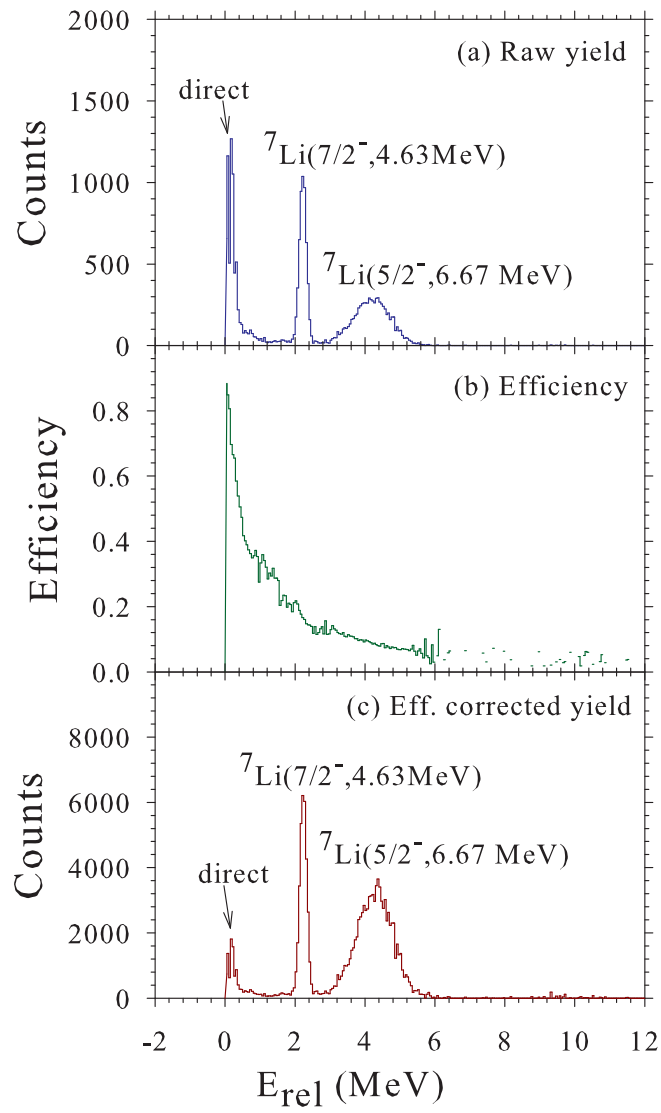


**Figure 5.1** (a) Relative energy distribution without efficiency correction, (b) efficiency of the detector array and (c) efficiency corrected relative energy distribution corresponding to  $\alpha + t$  breakup.

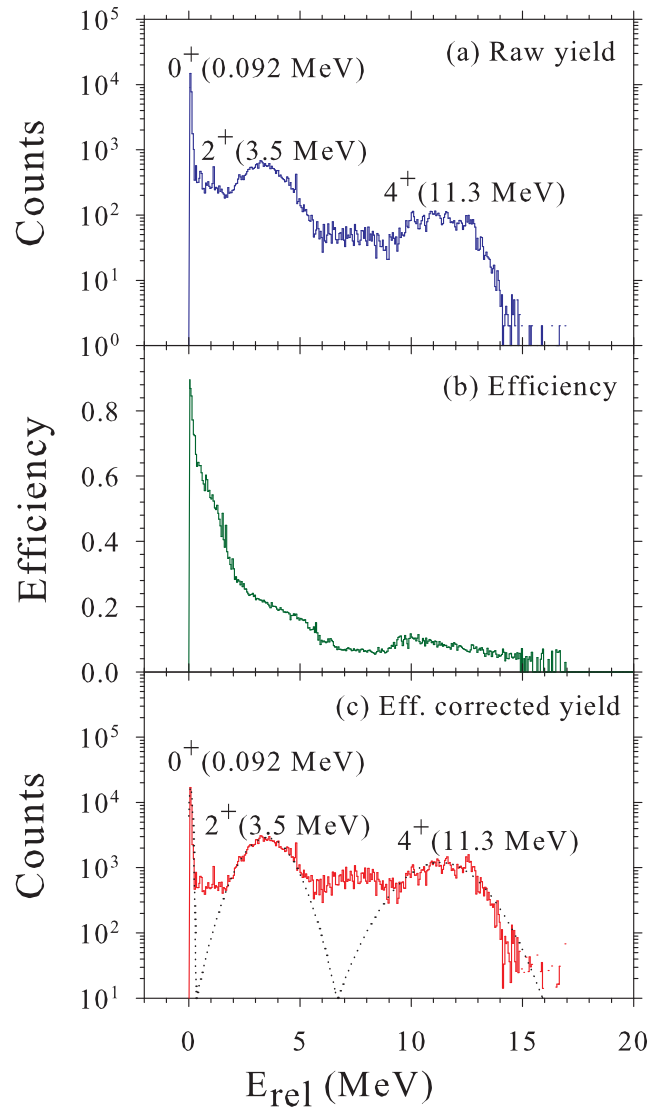


**Figure 5.2** (a) Relative energy distribution without efficiency correction, (b) efficiency of the detector array and (c) efficiency corrected relative energy distribution corresponding to  $\alpha + \alpha$  breakup.

**Table 5.1** Comparison of the observed energies and widths of the resonance peaks in relative energy distributions with the ones available from the literature [24, 59].

State	Present work		Literature	
	$E_{\text{rel}}$ (MeV)	$\Gamma$ (MeV)	$E_{\text{rel}}$ (MeV)	$\Gamma$ (MeV)
${}^7\text{Li} (7/2^-)$	2.23	0.20	2.16	0.09
${}^7\text{Li}(5/2^-)$	4.28	1.20	4.20	0.88
${}^8\text{Be}(0^+)$	0.09	0.05	0.092	0.0057
${}^8\text{Be} (2^+)$	3.5	2.2	3.12	1.513
${}^8\text{Be}(4^+)$	11.3	3.5	11.35	3.5
${}^6\text{Li}(3^+)$	0.68	0.14	0.71	0.024
${}^6\text{Li} (2^+)$	2.93	1.06	2.84	1.30
${}^6\text{Li}(1^+)$	4.50	1.29	4.18	1.50
${}^5\text{Li}(3/2^-)$	2.15	1.50	1.97	1.23

around 0.71 MeV, 2.84 MeV and 4.18 MeV which actually correspond to three resonances ( $3^+$ ,  $2^+$  and  $1^+$  states) of  ${}^6\text{Li}$  (see Table 5.1). In the relative energy distribution shown in Fig. 5.3(b) corresponding to  $2n$  stripping triggered breakup, i.e., ( ${}^7\text{Li}, {}^5\text{Li} \rightarrow \alpha + p$ ) reaction, it was observed that the breakup has proceeded only with  $E_{\text{rel}} \sim 1.97$  MeV which is equal to the  $Q$ -value of  ${}^5\text{Li}_{\text{gs}} \rightarrow \alpha + p$  reaction. The measured positions and widths of the peaks in relative energy distributions corresponding to the breakup of  ${}^7\text{Li}$ ,  ${}^6\text{Li}$  and  ${}^5\text{Li}$  have been compared with the literature data [24] as shown in Table 5.1 to identify the respective resonance states.

Despite a very high breakup threshold ( $\sim 10$  MeV) for  ${}^7\text{Li} \rightarrow {}^6\text{He} + p$  channel, it was interesting to observe a significant number of  ${}^6\text{He} - p$  events in the present measurement as shown in Fig. 5.3(c). For this breakup channel, the relative energy distribution does not have any well defined peak and hence it can be taken as a direct (non-resonant) breakup. The  ${}^7\text{Li}$  structure as a cluster of  ${}^6\text{He} + p$  is not well investigated. However, there is evidence of this structure in the observation of transfer or capture of  ${}^6\text{He}$  from  ${}^7\text{Li}$  by the target nuclei [62]. So, the present exclusive measurement of  ${}^6\text{He}$  in coincidence with a

proton that provides direct evidence of  ${}^6\text{He}+p$  cluster structure of  ${}^7\text{Li}$  is very important in understanding the possible cluster structures of  ${}^7\text{Li}$ .

### 5.2.2 Q-value distributions

Next, to find out the excitations of the residual target nuclei, the Q-value distributions corresponding to each of the above breakup reactions were also obtained. The Q-Value for each event has been obtained by using the following relation [9],

$$Q = E_1 + E_2 + E_{\text{loss}} + E_{\text{recoil}} - E_{\text{beam}} \quad (5.1)$$

where,  $E_1$  and  $E_2$  are the laboratory energies of the two breakup fragments,  $E_{\text{beam}}$  is the beam energy,  $E_{\text{loss}}$  is the energy loss in the target calculated at half-thickness and  $E_{\text{recoil}}$  is the recoil energy of the residual target nucleus in the laboratory frame. Two dimensional plots of  $E_{\text{rel}}$  versus Q-value can reveal the excitations of both projectile-like and target-like nuclei as shown in Fig. 5.4 for  $\alpha + p$ ,  $\alpha + t$  and  ${}^6\text{He}+p$  breakup, in Fig. 5.5 and Fig. 5.6 for  $\alpha + \alpha$  and  $\alpha + d$  breakup respectively. The plot gives the information about the excitations of target-like fragment associated with the particular breakup mode of projectile like fragment. In case of  $\alpha + t$  breakup and  ${}^6\text{He}+p$  breakup, most of the events are centered around Q-value equal to  $\sim -2.5$  MeV and  $\sim -10$  MeV respectively, corresponding to the ground state of  ${}^{112}\text{Sn}$ . However, for  $\alpha + p$  breakup, there are two distinct peaks at  $\sim 7.1$  MeV and  $\sim 5.8$  MeV in Q-value distribution corresponding to ground state and first excited state ( $2^+$ , 1.3 MeV) of  ${}^{114}\text{Sn}$  followed by a broad peak at  $Q \sim 4.3$  MeV corresponding to an average excitation of  $\sim 3$  MeV of  ${}^{114}\text{Sn}$  due to many closely spaced energy levels of  ${}^{114}\text{Sn}$  in this region. The relative energies for these  $\alpha$ - $p$  events with different Q-values are all centered around 1.97 MeV which is same as the energy released in  ${}^5\text{Li}_{\text{g.s.}} \rightarrow \alpha + p$  breakup. It has been observed from the Fig. 5.5 that for  $\alpha + \alpha$ ,  $0^+$  and  $2^+$  states are associated with target excitations up-to 14 MeV but the

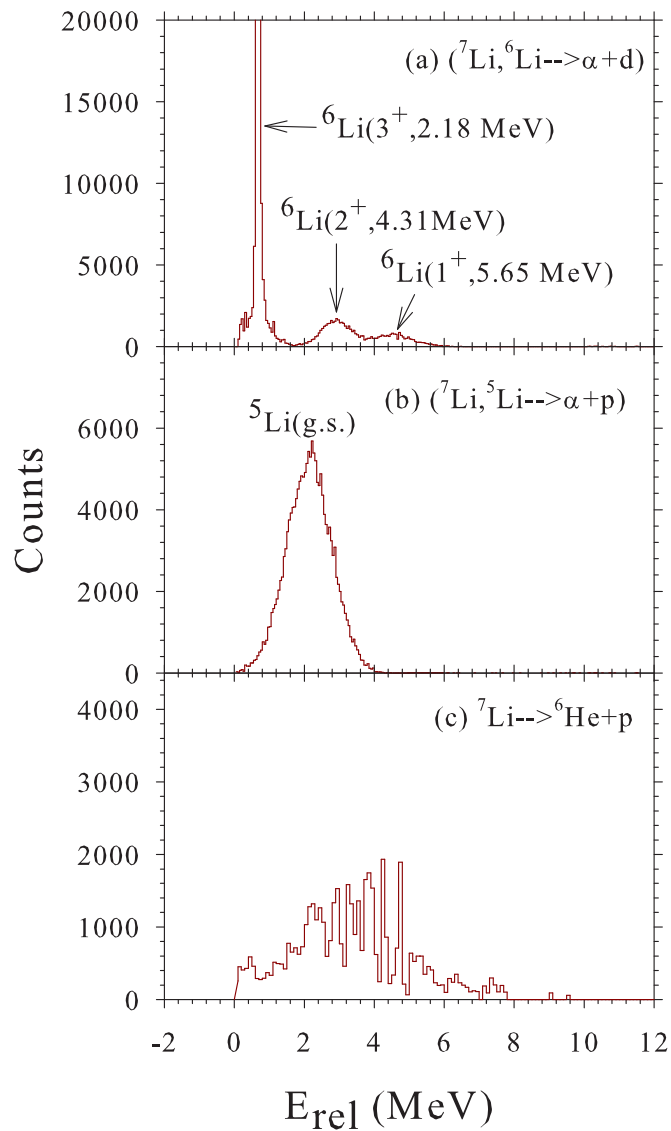


**Figure 5.3** Efficiency corrected relative energy distributions corresponding to (a)  $\alpha + d$  breakup, (b)  $\alpha + p$  breakup and (c)  ${}^6\text{He} + p$  breakup respectively. The relative energy bin size in the histogram (c) is 0.1 MeV which is double of that in (a) and (b).

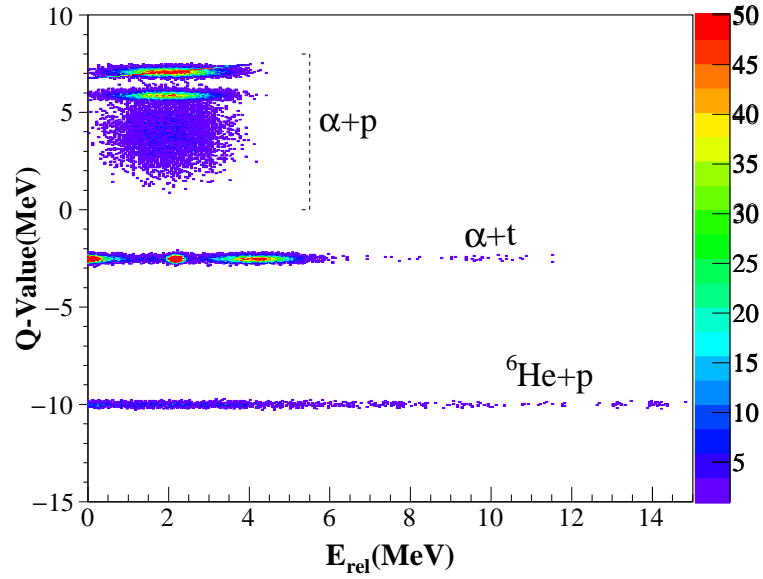


**Figure 5.4** Two dimensional plot of  $E_{\text{rel}}$  versus  $Q$ -value for  $\alpha+p$ ,  $\alpha+t$  and  ${}^6\text{He}+p$  breakup reactions showing the distribution of events with different projectile-like and target-like excitations.

$4^+$  state is associated only with the ground state and low lying excited states of residual target like nuclei.

In case of  $\alpha+d$  breakup (see Fig. 5.6), the maximum events were observed at  $Q \sim -1.0$  MeV corresponding to the ground state of  ${}^{113}\text{Sn}$  accompanied by three resonance states ( $3^+$ ,  $2^+$  and  $1^+$ ) of  ${}^6\text{Li}$ . However, there are events with excitation of  ${}^{113}\text{Sn}$  up to 11 MeV which are accompanied by only the  $3^+$  resonance excitation of  ${}^6\text{Li}$ . In addition there are direct (non-resonant) breakup with relative energies in the range of  $0-0.5$  MeV and  ${}^{113}\text{Sn}$  excitation up to  $\sim 10$  MeV. The breakup via  $2^+$  and  $1^+$  resonances are found to occur only with  ${}^{113}\text{Sn}$  in its ground state.

For  ${}^7\text{Li} \rightarrow {}^6\text{He}+p$  breakup, since the breakup threshold is very high ( $\sim 10$  MeV) the number of breakup events was found to be small and they primarily occur with no excitation of target-like nuclei.

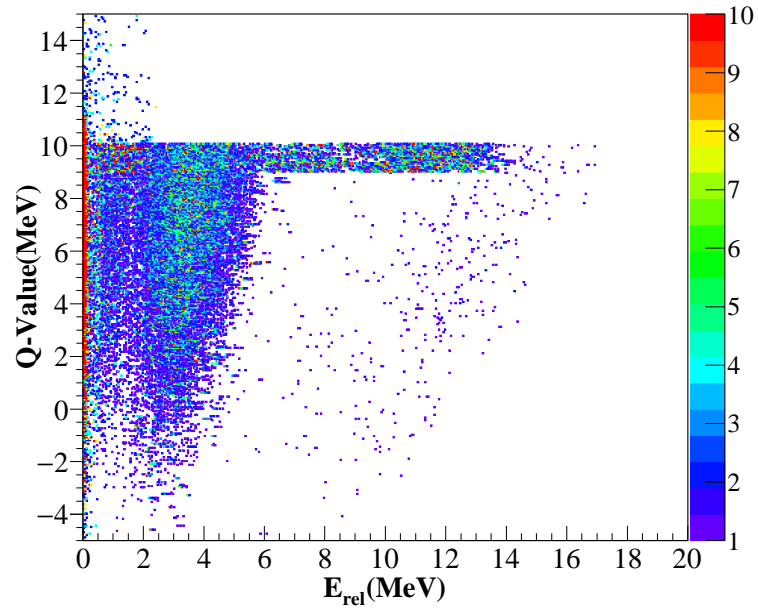


Figure 5.5 Same as Fig. 5.4 but for  $\alpha + \alpha$  breakup.

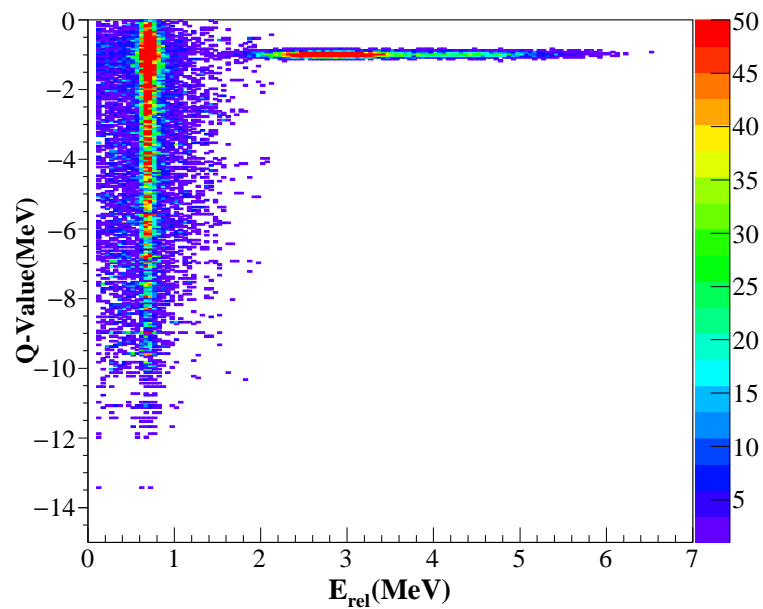


Figure 5.6 Same as Fig. 5.4 but for  $\alpha + d$  breakup.

### 5.3 Determination of breakup cross-section

The differential cross sections for each of the measured breakup channels have been obtained as follows. Consider the following reaction:



Where, ‘ $a$ ’ is weakly bound nucleus moving into the field of target ‘ $A$ ’. ‘ $b$ ’ represents the inelastic states of ‘ $a$ ’ above the breakup threshold or the intermediate quasi-bound projectile-like fragment formed through the exchange of nucleon between projectile and target. Using events reconstruction for a particular breakup channel  $c+d$ , a distribution of events corresponding to different  $\theta, \phi$  of the outgoing cluster particle just before breakup, i.e., ‘ $b$ ’ was generated. Now, for each  $\theta(b)$  bin, the efficiency corrected relative energy distribution ( $Y_i^{eff}(\theta) = Y_i^{raw}(\theta)/\zeta_i$ ) was obtained by summing over all  $\phi(b)$  coverage of detector array corresponding to same  $\theta(b)$  bin. Here,  $Y_i^{raw}(\theta)$  represents the yield of ‘ $i$ ’<sup>th</sup> bin of the relative energy between  $\epsilon_i$  and  $\epsilon_i + d\epsilon_i$  without efficiency correction and  $\zeta_i$  is the efficiency of the detector array for the same relative energy bin. For a particular  $\theta$  bin, the coincidence yields under the peaks corresponding to resonances in relative energy distribution have been extracted individually by integrating  $Y_i^{eff}(\theta)$  in steps of  $d\epsilon_i$  over the respective relative energy range ( $\Delta\epsilon = Nd\epsilon_i$ ). Differential breakup cross-sections for each of the resonance states is extracted from the following relation,

$$\frac{d\sigma^{br}}{d\Omega}(\theta) = \frac{\sum_{i=1}^N Y_i^{eff}(\theta)}{Y_{el}(\theta)} \frac{d\sigma^{el}}{d\Omega}(\theta) \quad (5.3)$$

where,  $Y_{el}(\theta)$  is the yield of elastic scattering in the solid angle corresponding to the element  $\Delta\theta(b)$ ,  $\Delta\phi(b)$  and  $\frac{d\sigma^{el}}{d\Omega}(\theta)$  is the differential elastic scattering cross section. The latter was obtained by normalizing (i)  $Y_{el}(\theta)$  to the monitor yield  $Y_m(\theta_m)$  corresponding to Rutherford scattering and (ii) their solid angles.

### 5.3.1 Direct and resonant breakup of ${}^7\text{Li}$

The differential breakup cross sections for  ${}^7\text{Li} \rightarrow \alpha + t$  breakup proceeding through  $7/2^-$  and  $5/2^-$  resonance states of  ${}^7\text{Li}$  have been obtained using the formulation mentioned above and shown as hollow circles in Fig. 5.7(a) and (b). The cross section for the direct breakup of  ${}^7\text{Li} \rightarrow \alpha + t$  with relative energy in the range of 0 – 0.5 MeV is shown in Fig. 5.7(c). Although the breakup cross-section via  $7/2^-$  resonance has been measured and described earlier using different targets, the cross section for  $5/2^-$  resonance is measured for the first time.

Breakup cross-sections for  ${}^7\text{Li} \rightarrow \alpha + t$  have been calculated by the same continuum discretized coupled channels (CDCC) method using FRESKO [50]. Here,  ${}^7\text{Li}$  is assumed to have a two body cluster structure of  $\alpha + t$  with the breakup threshold of 2.47 MeV. The continuum above this breakup threshold was discretized into momentum bins of widths  $\Delta k = 0.2 \text{ fm}^{-1}$  (up to  $k = 0.8 \text{ fm}^{-1}$ ) for each of the  $\alpha - t$  relative angular momentum  $L = 0, 1, 2, 3$ , where  $\hbar k$  denotes the momentum of their relative motion.

$$k^2 = \frac{2\mu}{\hbar^2} E_x \quad (5.4)$$

The quantity  $E_x$  is the excitation energy of  ${}^7\text{Li}$  above the  $\alpha + t$  breakup threshold and  $\mu$  is the reduced mass of the  $\alpha + t$  cluster system. The cluster wave functions  $\psi(r, k)$  in a bin were averaged over the bin width  $\Delta k$  and normalized to unity according to [63]

$$\Psi(r, k) = \frac{1}{\sqrt{N}} \int_{\Delta k} \psi(r, k) dk. \quad (5.5)$$

where,  $N$  is a normalization factor and  $r$  is the  $\alpha$ - $t$  separation. Each bin was then treated as an excited state of  ${}^7\text{Li}$  represented by a wave-function  $\Psi(r)$  at an energy corresponding to the mean energy of the bin and having spin  $\vec{I}$  and parity  $(-1)^L$ . The angular momenta  $\vec{I}$  and  $\vec{L}$  are related by  $\vec{I} = \vec{L} + \vec{s}$ , where  $\vec{s}$  is the spin of the valence triton

**Table 5.2** The states of the projectile  ${}^7\text{Li}$  included in the model space of the CDCC calculations.  $E_x$ ,  $E_{\min}$  and  $E_{\max}$  respectively represent the mean, minimum and maximum excitation energies of a particular bin state above the  $\alpha$ - $t$  breakup threshold.

$L$	$I^\pi$	$E_x$ (MeV)	$E_{\min}$ (MeV)	$E_{\max}$ (MeV)
0	1/2 <sup>+</sup>	0.2421	0.0021	0.4821
0	1/2 <sup>+</sup>	1.2103	0.4841	1.9365
0	1/2 <sup>+</sup>	3.1470	1.9365	4.3570
0	1/2 <sup>+</sup>	6.0520	4.3570	7.7460
1	3/2 <sup>-</sup>	-2.4700 (ground state)	-	-
1	3/2 <sup>-</sup>	0.2421	0.0021	0.4821
1	3/2 <sup>-</sup>	1.2103	0.4841	1.9365
1	3/2 <sup>-</sup>	3.1470	1.9365	4.3570
1	3/2 <sup>-</sup>	6.0520	4.3570	7.7460
1	1/2 <sup>-</sup>	-1.9900 (bound inelastic)	-	-
1	1/2 <sup>-</sup>	0.2421	0.0021	0.4821
1	1/2 <sup>-</sup>	1.2103	0.4841	1.9365
1	1/2 <sup>-</sup>	3.1470	1.9365	4.3570
1	1/2 <sup>-</sup>	6.0520	4.3570	7.7460
2	5/2 <sup>+</sup>	0.2421	0.0021	0.4821
2	5/2 <sup>+</sup>	1.2103	0.4841	1.9365
2	5/2 <sup>+</sup>	3.1470	1.9365	4.3570
2	5/2 <sup>+</sup>	6.0520	4.3570	7.7460
2	3/2 <sup>+</sup>	0.2421	0.0021	0.4821
2	3/2 <sup>+</sup>	1.2103	0.4841	1.9365
2	3/2 <sup>+</sup>	3.1470	1.9365	4.3570
2	3/2 <sup>+</sup>	6.0520	4.3570	7.7460
3	7/2 <sup>-</sup>	0.2421	0.0021	0.4821
3	7/2 <sup>-</sup>	1.272	0.4840	2.0600
3	7/2 <sup>-</sup>	2.1600	2.0600	2.2600
3	7/2 <sup>-</sup>	3.2900	2.2600	4.3200
3	5/2 <sup>-</sup>	0.2421	0.0021	0.4821
3	5/2 <sup>-</sup>	1.2103	0.4841	1.9365
3	5/2 <sup>-</sup>	2.3200	1.9370	2.7100
3	5/2 <sup>-</sup>	4.2100	2.7100	5.7100

and  $\vec{L}$  is the relative angular momentum of the  $\alpha + t$  cluster system. The binning of the continuum with  $L = 3$  has been suitably modified to include the resonance states  $\frac{7^-}{2}$  and  $\frac{5^-}{2}$  with average excitation energy of 2.19 MeV and 4.21 MeV, and width of 0.2 MeV and 3.0 MeV respectively. The model space of  ${}^7\text{Li}$  that includes the discretized states with mean excitation energy  $E_x$ , minimum to maximum excitation energy ( $E_{\min}$  to  $E_{\max}$ ) of the corresponding bin are enlisted in Table 5.2.

The CDCC calculations were performed using cluster-folded (CF) interaction, where Sao-Paolo potentials [64] multiplied by 0.65 were used as the real parts of the fragment-target ( $\alpha + {}^{112}\text{Sn}$  and  $t + {}^{112}\text{Sn}$ ) potentials. The imaginary potential for  $\alpha + {}^{112}\text{Sn}$  was taken from Ref. [?] including both volume and surface terms, and for  $t + {}^{112}\text{Sn}$  it has been calculated from global optical model [65] considering only the surface term. The  $\alpha$ - $t$  binding potentials of Ref. [66], suitably modified for resonances, have been used.

The width of the  $5/2^-$  state being much larger ( $\sim 1.2$  MeV) than for the  $7/2^-$  state ( $\sim 0.2$  MeV), the yield under the  $5/2^-$  peak can have some contributions from non-resonant breakup with the same relative energies but different  $L$  values. In addition, the contribution from another  $5/2^-$  resonant state at 7.46 MeV [24,67], though small, could be present. In fact, a larger cross section for the  $5/2^-$  state than for the  $7/2^-$  state has also been observed in the case of resonance scattering of  ${}^4\text{He}$  from  ${}^3\text{H}$  by Spiger and Tombrello [68] and Ivanovich et al. [69].

Similarly, the differential cross sections for direct breakup of  ${}^7\text{Li}$  into  ${}^6\text{He}$  and  $p$ , which is again measured for the first time has been shown in Fig. 5.7(d). The cross section for the ( ${}^7\text{Li}, {}^6\text{He}$ ) transfer reaction corresponding to  $Q_{gg} = -6.9$  MeV has also been shown as an inset to Fig. 5.7(d), and found to be much larger than for the  ${}^6\text{He} + p$  breakup.

### 5.3.2 $-1n$ and $-2n$ transfer breakup of ${}^7\text{Li}$

The differential cross-sections for  $-2n$  transfer followed by immediate breakup i.e.,  ${}^7\text{Li} \xrightarrow{-2n} {}^5\text{Li} \rightarrow \alpha + p$  breakup via the ground state ( $3/2^-$ ) of  ${}^5\text{Li}$  are shown in Fig. 5.8(a).

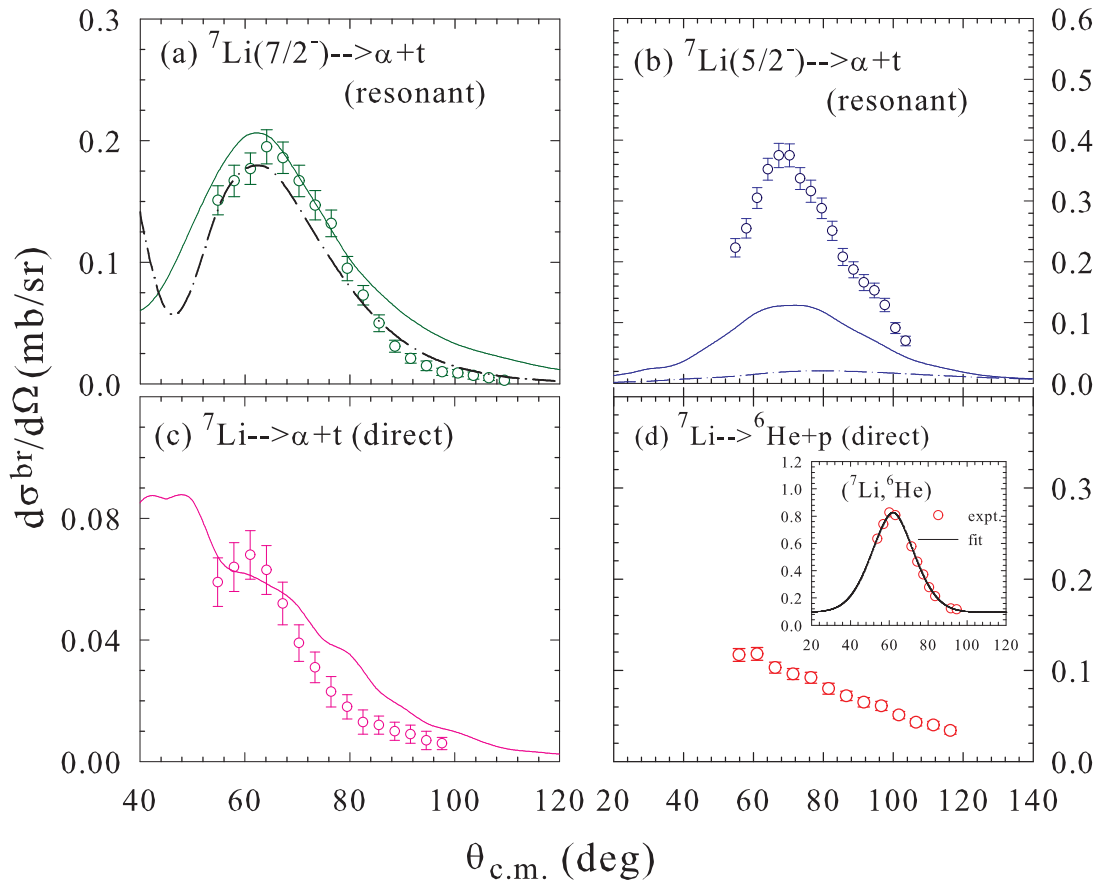


**Figure 5.7** Differential cross sections for (a,b) sequential breakup of  ${}^7\text{Li} \rightarrow \alpha + t$  for its  $7/2^-$  and  $5/2^-$  resonance states respectively, (c) direct breakup of  ${}^7\text{Li} \rightarrow \alpha + t$  and (d) direct breakup of  ${}^7\text{Li} \rightarrow {}^6\text{He} + p$ . The lines represent the results of CDCC calculations.

Similarly, the differential cross-sections obtained for  $1n$  stripping followed by breakup into  $\alpha + d$  through  $3^+$ ,  $2^+$  and  $1^+$  resonance states of  ${}^6\text{Li}$  are shown in Fig. 5.8(b), (c) and (d) respectively. The elastic scattering angular distribution that was used for cross section normalization and for obtaining potential parameters required for coupled-channels calculations has also been shown as an inset of Fig. 5.8(b). The lines in Fig. 5.8 represent the results of the coupled-channels calculations described in the following section.

For  $-1n$  and  $-2n$  transfer induced breakup channels, the coupled reaction channel (CRC) calculations using FRESKO have been compared with the measured  $\alpha + d$  and  $\alpha + p$  breakup cross sections, respectively. After  $1n$  stripping from the projectile  ${}^7\text{Li}$  to the target  ${}^{112}\text{Sn}$ , when  ${}^6\text{Li}$  is formed in an excited state above the  $\alpha - d$  breakup threshold, it immediately breaks up into an  $\alpha - d$  pair. So only the resonance states of  ${}^6\text{Li}$  were considered. For the entrance channel of the CRC calculation scheme, the real and imaginary potentials of the Woods-Saxon volume form with  $V_0 = 25.33$  MeV,  $r_0 = 1.185$  fm,  $a_0 = 0.75$  fm,  $W = 25.38$  MeV,  $r_W = 1.17$  fm, and  $a_W = 0.787$  fm, obtained from the fit to the measured elastic scattering, were used. For the exit channels, the real potentials are the same as above but the imaginary potentials were taken to be of short-range and Woods-Saxon square forms. The  $3^+$  state of  ${}^6\text{Li}$  was coupled to the ground plus six excited states of  ${}^{113}\text{Sn}$ , whereas the  $2^+$  and  $1^+$  states of  ${}^6\text{Li}$  were coupled only to the ground state of  ${}^{113}\text{Sn}$  because experimentally it was observed that the breakups of  $2^+$  and  $1^+$  states are accompanied by only the ground-state excitation of  ${}^{113}\text{Sn}$ . The spectroscopic amplitudes for  $\langle {}^{112}\text{Sn} + n | {}^{113}\text{Sn} \rangle$  corresponding to seven states of  ${}^{113}\text{Sn}$  with  $E_x = 0-1.556$  MeV are taken from Ref. [54]. Spectroscopic amplitudes for  $\langle {}^7\text{Li} | {}^6\text{Li}_{2.18\text{MeV}} + n \rangle$ ,  $\langle {}^7\text{Li} | {}^6\text{Li}_{4.31\text{MeV}} + n \rangle$ , and  $\langle {}^7\text{Li} | {}^6\text{Li}_{5.65\text{MeV}} + n \rangle$  are optimized at 0.605, 0.905, and 1.205, respectively, to reproduce the experimental cross sections.

For dineutron stripping, the ejectile  ${}^5\text{Li}$  being a quasi-bound nucleus breaks into  $\alpha$  and  $p$ . Hence, the cross section for  $-2n$  transfer calculated from CRC calculations is equal to the  $\alpha + p$  breakup cross section. From the Q-value distribution it was observed that a

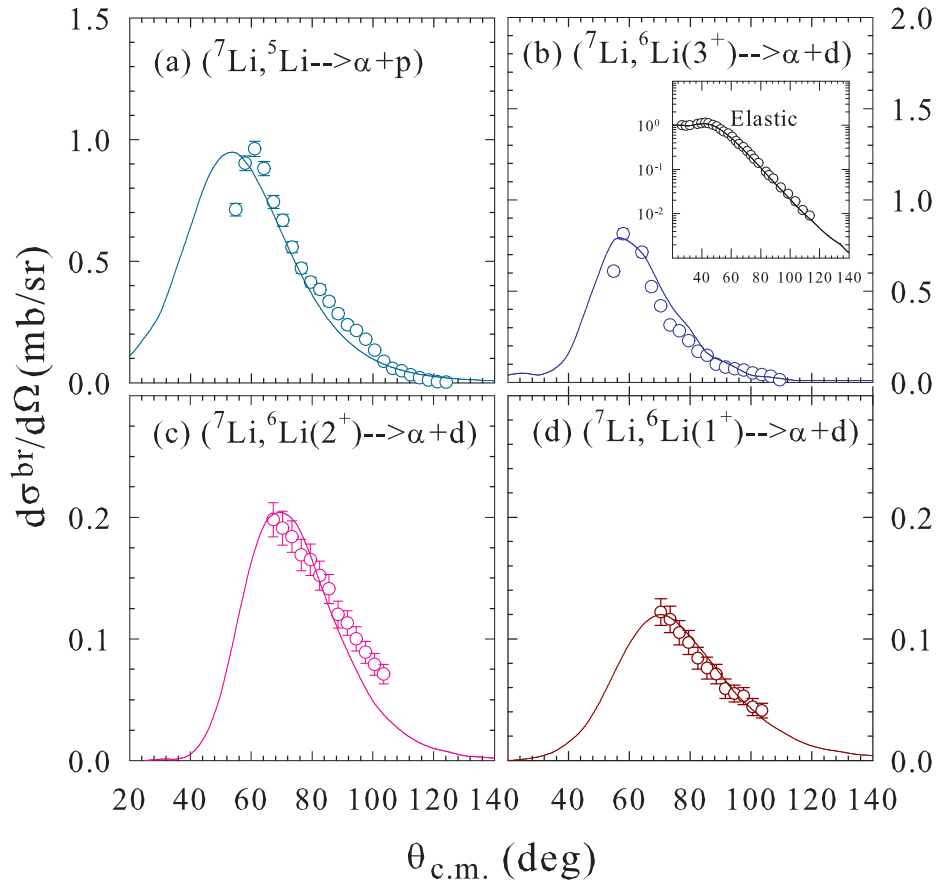


**Figure 5.8** Differential cross sections for (a) sequential breakup of  ${}^7\text{Li} \xrightarrow{-2n} {}^5\text{Li} \rightarrow \alpha + p$  and (b-d) sequential breakup of  ${}^7\text{Li} \xrightarrow{-1n} {}^6\text{Li} \rightarrow \alpha + d$  through  $3^+$ ,  $2^+$  and  $1^+$  resonance states of  ${}^6\text{Li}$  respectively. Solid lines represent the results of CRC calculations.

one-step transfer process is dominating, so only direct stripping of  $2n$  from  ${}^7\text{Li}$  has been considered in the calculations. Again, the entrance and exit channel real potentials are the same. The imaginary potential in the exit channel is short ranged. In the couplings, the g.s. of  ${}^5\text{Li}$  and g.s. plus first excited state of  ${}^{114}\text{Sn}$  have been included. The spectroscopic amplitudes  $\langle {}^7\text{Li} | {}^5\text{Li} + 2n \rangle$  and  $\langle {}^{114}\text{Sn} | {}^{112}\text{Sn} + 2n \rangle$  are taken to be 1.0. The calculations represented by solid lines in Fig. 5.8 reproduce the experimental data reasonably well.

### 5.3.3 +1p transfer breakup of ${}^7\text{Li}$

The differential breakup cross-sections thus obtained for  $0^+$ ,  $2^+$  and  $4^+$  states of  ${}^8\text{Be}$  includes the events corresponding to all possible target excitations and are shown as filled circles in Fig. 5.9(a), (b) and (c) respectively. The breakup cross sections for  $0^+$ ,  $2^+$  and  $4^+$  states are in decreasing order as expected. Although the breakup cross-section via  $0^+$  and  $2^+$  states of  ${}^8\text{Be}$  have been measured and described earlier, the cross section for  $4^+$  state is measured for the first time.

Due to so many closely spaced low lying energy levels of the residual target nucleus  ${}^{111}\text{In}$ , it is possible to have the  $2\alpha$  breakup events associated with large number of target excitations, particularly for  $0^+$  and  $2^+$  breakup. But, it is difficult to identify the events corresponding to individual excitations. It is also difficult to include so many target excitations in the coupled reaction channels (CRC) calculations due to the computation limitation leading to difficulty in comparing the experimental total  $2\alpha$  breakup with the theory. However, the events corresponding to ‘no target excitation’ are identifiable. So, the breakup cross sections for these events have been extracted separately as shown as hollow circles in the respective figures. Dashed lines represent the results of CRC calculations (described in the next section) corresponding to the target being in the ground state. In order to compare the shape of the experimental total breakup cross sections with theory, a few representative states of low lying target excitations have been included in the CRC couplings. Solid lines represent the sum of the cross sections corresponding

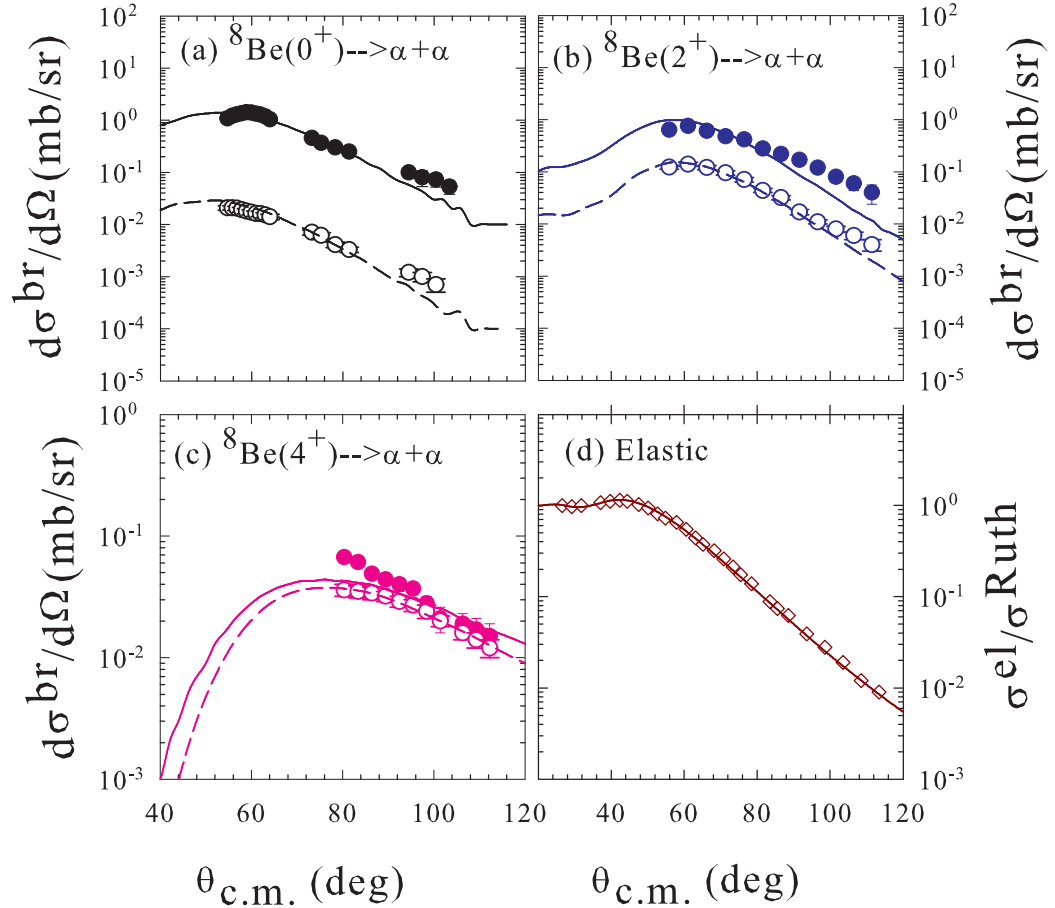


**Figure 5.9** Differential cross sections in center-of-mass frame for sequential breakup of  ${}^7\text{Li} \rightarrow {}^8\text{Be} \rightarrow \alpha + \alpha$  corresponding to (a)  $0^+$ , (b)  $2^+$  and (c)  $4^+$  states of  ${}^8\text{Be}$  along with (d) the elastic scattering, measured at  $E_{\text{beam}} = 30$  MeV. The hollow circles in (a), (b) and (c) represent  $2\alpha$  breakup cross sections corresponding to no target excitation, whereas, the filled circles represent total breakup cross sections corresponding to both ground state as well as excited states of the target like nuclei. Lines represent the results of the CRC calculations using FRESKO. Dashed lines represent theoretical cross sections only for g.s. to g.s. transition and solid lines represent total cross sections for g.s. and excited states of  ${}^{111}\text{In}$ .

to the ground state and all the excitations of the target that have been included in the calculations. The measured elastic scattering angular distribution has been shown as open diamonds in Fig. 5.9(d). The solid lines in Fig. 5.9(a)-(d) represent the results from CRC calculations. The details of the CRC calculations have been given below.

Coupled channels calculations using FRESKO (Version2.9) [50] have been performed to understand the above experimental breakup cross sections of  $\alpha - \alpha$ . Two sets of calculations have been carried out. First, only the CRC calculations have been made where no projectile breakup coupling is considered. However, the optical model potentials, obtained from the fit to the measured elastic scattering angular distribution, has been used for the entrance (elastic) channel. This may be considered as the local equivalent potential (i.e., bare+polarization potential) that has taken care of the effect of couplings of breakup and other direct reaction channels on elastic.

In the second case, both the continuum discretized coupled channels (CDCC) as well as the CRC calculations have been carried out using a bare potential in order to find the effect of couplings of breakup and other direct reaction channels on elastic and perform a simultaneous analysis of projectile breakup and transfer channels. Details of these calculations have been described in two separate sections as follows.

### 5.3.3.1 CRC calculation:

In the present CRC calculations, only two mass partitions (with  ${}^7\text{Li}$  and  ${}^8\text{Be}$  as ejectiles) have been considered. In the elastic-inelastic mass partition, both  ${}^7\text{Li}$  and  ${}^{112}\text{Sn}$  have been considered to be in ground state. The second mass partition corresponds to 1p pickup, i.e., ( ${}^7\text{Li}, {}^8\text{Be}$ ) reaction. In this mass partition, the outgoing channels included in the couplings correspond to  $0^+$ ,  $2^+$  and  $4^+$  states of  ${}^8\text{Be}$ , and the ground state ( $9/2^+$ ) plus twenty five excited states of  ${}^{111}\text{In}$  as listed in Table 5.3. When  ${}^8\text{Be}$  is in g.s., all the target excitations have been assumed to be possible. But, for  $2^+$  and  $4^+$  excitations of  ${}^8\text{Be}$  only the g.s. plus two excitations of  ${}^{111}\text{In}$  have been considered. The details of the

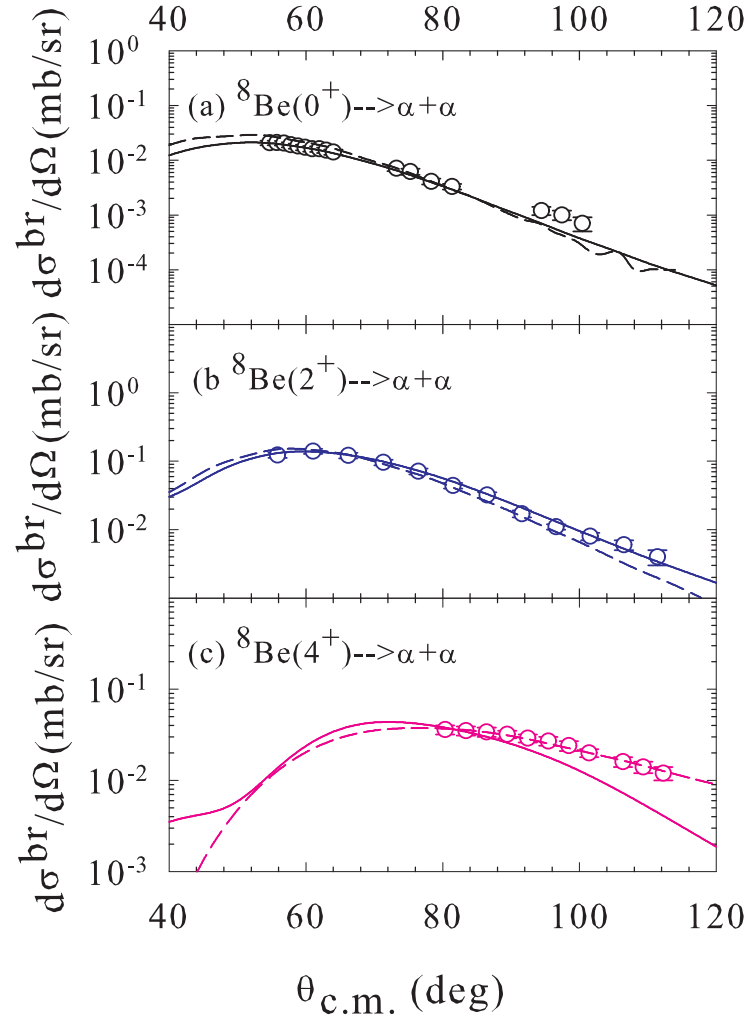


**Figure 5.10** Experimental and theoretical cross sections for sequential breakup of  ${}^7\text{Li} \rightarrow {}^8\text{Be} \rightarrow \alpha + \alpha$  corresponding to (a)  $0^+$ , (b)  $2^+$  and (c)  $4^+$  states of  ${}^8\text{Be}$  corresponding to no target excitation. Dashed and solid lines represent the results of FRESKO calculations using ‘CRC only’ and ‘CDCC+CRC’ formalisms respectively.

states coupled including the spectroscopic information and the spectroscopic amplitudes for the overlaps  $\langle {}^8\text{Be} | {}^7\text{Li} + p \rangle$  and  $\langle {}^{112}\text{Sn} | {}^{111}\text{In} + p \rangle$  used in the CRC calculations are given in Table 5.3.

The real and imaginary potentials of Woods-Saxon volume form with  $V_0=25.33$  MeV,  $r_0=1.185$  fm,  $a_0=0.75$  fm,  $W_0=25.38$  MeV,  $r_w=1.17$  fm and  $a_w=0.787$  fm, obtained from the optical model fit to the measured elastic scattering angular distribution have been used for the elastic-inelastic mass partition. For the transfer mass partition, the real part of the optical potential was same as that of the entrance channel mass partition but the imaginary part was taken to be of short range Wood-Saxon square form with  $W_0=10.00$  MeV,  $r_w=1.00$  fm and  $a_w=0.4$  fm. The binding potentials for  $p+{}^7\text{Li}$  are taken to be real and also of Woods-Saxon volume form with  $V_0=50.0$  MeV,  $r_0=1.15$  fm,  $a_0=0.57$  fm,  $V_{so}=5.5$  MeV,  $r_{so}=1.15$  fm,  $a_{so}=0.57$  fm, where the subscript ‘so’ corresponds to the spin-orbit term. The depth is automatically varied to reproduce the binding energy. Similarly the binding potential parameters used for  $p+{}^{111}\text{In}$  are  $V_0=50.0$  MeV,  $r_0=1.23$  fm,  $a_0=0.65$  fm,  $V_{so}=6.0$  MeV,  $r_{so}=1.23$  fm,  $a_{so}=0.65$  fm.

Due to the presence of so many closely spaced low lying excited states of  ${}^{111}\text{In}$  within the measured energy range the cross sections corresponding to each of the target excitations could not be extracted. Also, in CRC calculations it was not possible to include all these excitations. So, the measured total  $2\alpha$  breakup cross sections corresponding to all these states cannot be compared with the calculations that have included only a limited number of excitations. However, the breakup yields corresponding to  $0^+$ ,  $2^+$  and  $4^+$  states of  ${}^8\text{Be}$  with no target excitation being reasonably clean, the corresponding cross sections have been extracted separately and compared with the CRC results. The dashed lines in Fig. 5.9 represent the calculations assuming target in the ground state and they reproduce the experimental data reasonably well.

### 5.3.3.2 CDCC-CRC calculation:

To investigate the effect of projectile breakup and other direct reaction channels on elastic scattering simultaneously, the CDCC as well as CRC calculations using FRESKO have been carried out. Both, the transfer channels and the inelastic (bound and unbound) excitations of the projectile have been coupled simultaneously. For transfer mass partitions, the real potentials of Woods-Saxon volume form with  $V_0=25.33$  MeV,  $r_0=1.185$  fm and  $a_0=0.75$  fm, obtained from the optical model fit to the measured elastic scattering angular distribution, have been used. Whereas, the imaginary potentials used were of Woods-Saxon square form with  $W_0=10.0$  MeV,  $r_w=1.0$  fm and  $a_w=0.63$  fm. For the  $+1p$  transfer mass partition, the number of outgoing channels included in the couplings is now reduced compared to the previous (CRC only) calculations due to the limitation in total number of channels that can be included at a time. These channels now correspond to  $0^+$ ,  $2^+$  and  $4^+$  states of  ${}^8\text{Be}$ , and ground state ( $9/2^+$ ) plus four excited states i.e., ( $1/2^-$ , 0.537 MeV), ( $3/2^-$ , 0.803 MeV), ( $1/2^+$ , 1.187 MeV) and ( $5/2^+$ , 2.212 MeV) states of  ${}^{111}\text{In}$ . The spectroscopic amplitudes used are same as those given in Table 5.3.

## 5.4 $-1n$ and $-1p$ transfer cross-section of ${}^7\text{Li}$

Apart from the dominant breakup channels,  $-1n$  and  $-1p$  transfer reaction cross-sections has also been measured. A simultaneous description of elastic,  $-1n$  transfer,  $-1p$  transfer and  $+1p$  transfer channels have also been attempted using the same set of potential and coupling parameters using the CDCC-CRC approach via FRESKO [50]. For the  $-1n$  and  $-1p$  transfer mass partitions, the number of outgoing channels included in the couplings are seven and six respectively. The details of these two transfer channels including the spectroscopic amplitudes and structure information on the states included in the couplings are given in Table 5.4.

Typical  $-1p$  transfer cross sections calculated from the CDCC+CRC calculations (solid

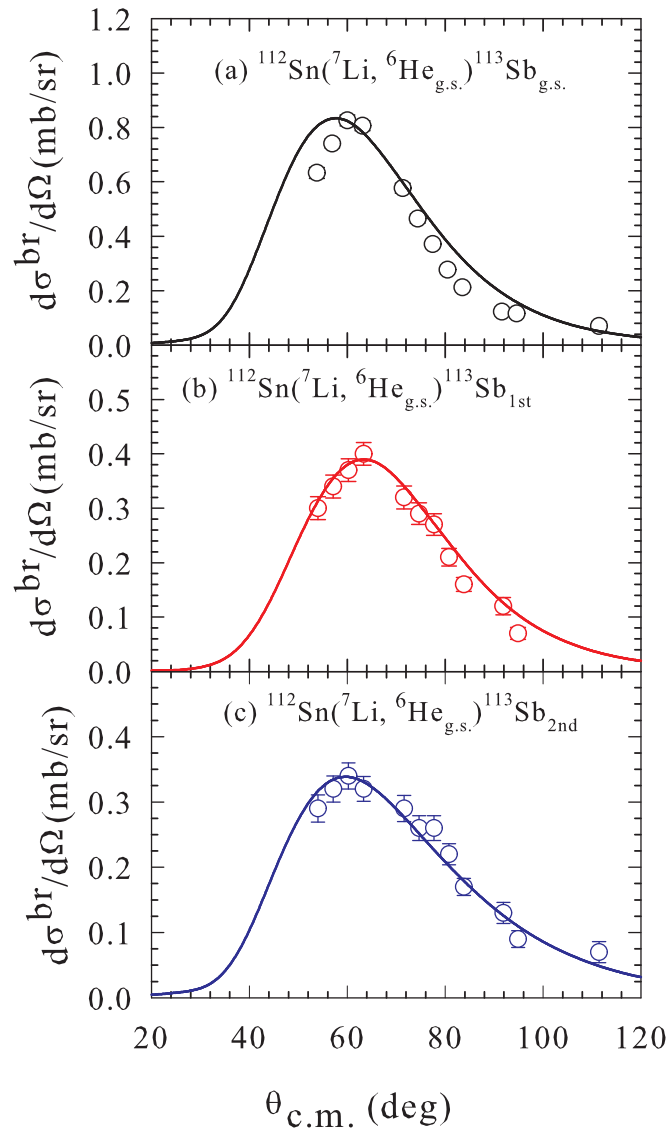


**Figure 5.11** Experimental cross sections for 1p stripping corresponding to g.s. of  ${}^6\text{He}$  and (a) g.s., (b) 1st excited state and (c) 2nd excited state of  ${}^{113}\text{Sb}$ . Solid lines represent FRESKO calculations using ‘CDCC+CRC’ formalism.

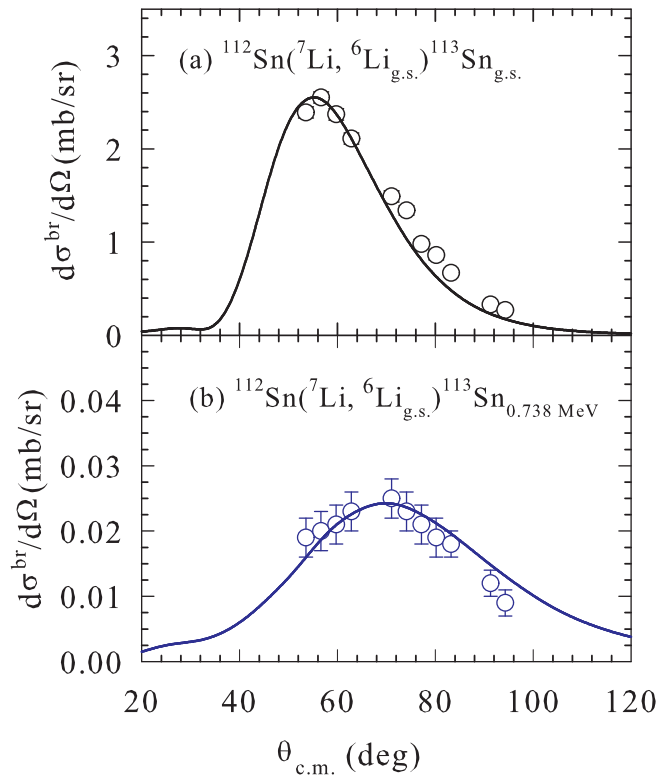


**Figure 5.12** Experimental cross sections for  $1n$  stripping corresponding to g.s. of  ${}^6\text{Li}$  and (a) g.s. and (b) 0.738 MeV excited state of  ${}^{113}\text{Sn}$ . Solid lines represent FRESKO calculations using ‘CDCC+CRC’ formalism.

**Table 5.3** Structure information and spectroscopic amplitudes for the overlaps  $A = C + x$  corresponding to different states of the nuclei  $A$ ,  $C$  and  $x$  used in the CRC calculations for ( ${}^7\text{Li}, {}^8\text{Be}$ ) reaction.

$Nucleus$ ( $A$ )	$C$	$x$	BE (MeV)	$nlj(x)$	SA
${}^8\text{Be}(0^+)$	${}^7\text{Li}(\text{g.s.}, 3/2^-)$	$p$	17.255	$1p_{3/2}$	1.00
${}^8\text{Be}(2^+)$	${}^7\text{Li}(\text{g.s.}, 3/2^-)$	$p$	14.135	$1p_{3/2}$	1.00
${}^8\text{Be}(4^+)$	${}^7\text{Li}(\text{g.s.}, 3/2^-)$	$p$	5.905	$1f_{5/2}$	0.80
${}^8\text{Be}(4^+)$	${}^7\text{Li}(\text{g.s.}, 3/2^-)$	$p$	5.905	$1f_{7/2}$	0.80
${}^{112}\text{Sn}(0^+)$	${}^{111}\text{In}(\text{g.s.}, 9/2^+)$	$p$	7.560	$1g_{9/2}$	0.87
${}^{112}\text{Sn}(0^+)$	${}^{111}\text{In}(0.537 \text{ MeV}, 1/2^-)$	$p$	7.023	$2p_{1/2}$	0.87
${}^{112}\text{Sn}(0^+)$	${}^{111}\text{In}(0.803 \text{ MeV}, 3/2^-)$	$p$	6.757	$2p_{3/2}$	0.87
${}^{112}\text{Sn}(0^+)$	${}^{111}\text{In}(1.185 \text{ MeV}, 1/2^+)$	$p$	6.375	$3s_{1/2}$	0.87
${}^{112}\text{Sn}(0^+)$	${}^{111}\text{In}(1.217 \text{ MeV}, 5/2^+)$	$p$	6.343	$2d_{5/2}$	0.87
${}^{112}\text{Sn}(0^+)$	${}^{111}\text{In}(1.279 \text{ MeV}, 5/2^+)$	$p$	6.281	$2f_{5/2}$	0.87
${}^{112}\text{Sn}(0^+)$	${}^{111}\text{In}(1.345 \text{ MeV}, 3/2^+)$	$p$	6.215	$2d_{3/2}$	0.87
${}^{112}\text{Sn}(0^+)$	${}^{111}\text{In}(1.500 \text{ MeV}, 7/2^-)$	$p$	6.060	$1g_{7/2}$	0.87
${}^{112}\text{Sn}(0^+)$	${}^{111}\text{In}(1.610 \text{ MeV}, 9/2^-)$	$p$	5.950	$1g_{9/2}$	0.87
${}^{112}\text{Sn}(0^+)$	${}^{111}\text{In}(1.752 \text{ MeV}, 9/2^-)$	$p$	5.808	$1g_{9/2}$	0.87
${}^{112}\text{Sn}(0^+)$	${}^{111}\text{In}(1.866 \text{ MeV}, 1/2^+)$	$p$	5.694	$3s_{1/2}$	0.87
${}^{112}\text{Sn}(0^+)$	${}^{111}\text{In}(1.919 \text{ MeV}, 3/2^+)$	$p$	5.641	$2d_{3/2}$	0.87
${}^{112}\text{Sn}(0^+)$	${}^{111}\text{In}(2.085 \text{ MeV}, 1/2^+)$	$p$	5.475	$3s_{1/2}$	0.87
${}^{112}\text{Sn}(0^+)$	${}^{111}\text{In}(2.200 \text{ MeV}, 5/2^+)$	$p$	5.360	$2d_{5/2}$	0.87
${}^{112}\text{Sn}(0^+)$	${}^{111}\text{In}(2.292 \text{ MeV}, 3/2^+)$	$p$	5.268	$2d_{3/2}$	0.87
${}^{112}\text{Sn}(0^+)$	${}^{111}\text{In}(2.361 \text{ MeV}, 9/2^-)$	$p$	5.199	$1g_{9/2}$	0.87
${}^{112}\text{Sn}(0^+)$	${}^{111}\text{In}(2.529 \text{ MeV}, 5/2^+)$	$p$	5.031	$2d_{5/2}$	0.87
${}^{112}\text{Sn}(0^+)$	${}^{111}\text{In}(2.616 \text{ MeV}, 3/2^+)$	$p$	4.944	$2d_{3/2}$	0.87

lines) corresponding to g.s., 1st excited state and second excited state of  ${}^{113}\text{Sb}$ , have been shown in Fig. 5.11 (a), (b) and (c) respectively. Similarly, for -1n transfer reactions the cross sections obtained from the CDCC+CRC calculations (solid lines) have been shown in Fig. 5.12 (a) and (b) corresponding to g.s. and 0.738 MeV excited state of  ${}^{113}\text{Sn}$  respectively. The calculations are found to reproduce the measured data (hollow circles) reasonably well. It implies that the parameters used in the coupled channels calculations are realistic using which it has been possible to describe elastic scattering and several transfer channels simultaneously through a single coupled-channels calculation.

**Table 5.4** Structure information and spectroscopic amplitudes for the overlaps  $A = C + x$  corresponding to different states of the nuclei  $A$ ,  $C$  and  $x$  used in the CRC calculations for ( ${}^7\text{Li}, {}^6\text{Li}$ ) and ( ${}^7\text{Li}, {}^6\text{He}$ ) reactions.

<i>Nucleus</i> ( $A$ )	$C$	$x$	BE (MeV)	$nlj(x)$	SA
${}^7\text{Li}(3/2^-)$	${}^6\text{Li}_{g.s.}$	$n$	7.251	$1p_{1/2}$	0.690
${}^7\text{Li}(1/2^-)$	${}^6\text{Li}_{g.s.}$	$n$	7.739	$1p_{1/2}$	0.657
${}^{113}\text{Sn}(1/2^+)$	${}^{112}\text{Sn}_{g.s.}$	$n$	7.744	$3s_{1/2}$	1.077 [54]
${}^{113}\text{Sn}(7/2^+)$	${}^{112}\text{Sn}_{g.s.}$	$n$	7.667	$1g_{7/2}$	0.556 [54]
${}^{113}\text{Sn}(5/2^+)$	${}^{112}\text{Sn}_{g.s.}$	$n$	7.334	$2d_{5/2}$	0.387 [54]
${}^{113}\text{Sn}(3/2^+)$	${}^{112}\text{Sn}_{g.s.}$	$n$	7.245	$2d_{3/2}$	0.866 [54]
${}^{113}\text{Sn}(11/2^-)$	${}^{112}\text{Sn}_{g.s.}$	$n$	7.005	$1h_{11/2}$	1.140 [54]
${}^{113}\text{Sn}(5/2^+)$	${}^{112}\text{Sn}_{g.s.}$	$n$	6.725	$2d_{5/2}$	0.130 [54]
${}^{113}\text{Sn}(5/2^+)$	${}^{112}\text{Sn}_{g.s.}$	$n$	6.183	$2d_{5/2}$	0.230 [54]
${}^7\text{Li}(3/2^-)$	${}^6\text{He}_{g.s.}$	$p$	9.980	$1p_{3/2}$	0.768 [70]
${}^7\text{Li}(1/2^-)$	${}^6\text{He}_{g.s.}$	$p$	10.458	$1p_{1/2}$	0.768
${}^{113}\text{Sb}(5/2^+)$	${}^{112}\text{Sn}_{g.s.}$	$p$	3.050	$2d_{5/2}$	0.920
${}^{113}\text{Sb}(1/2^+)$	${}^{112}\text{Sn}_{g.s.}$	$p$	2.405	$3s_{1/2}$	0.920
${}^{113}\text{Sb}(7/2^+)$	${}^{112}\text{Sn}_{g.s.}$	$p$	2.236	$1g_{7/2}$	0.920
${}^{113}\text{Sb}(5/2^+)$	${}^{112}\text{Sn}_{g.s.}$	$p$	2.032	$2d_{5/2}$	0.920
${}^{113}\text{Sb}(9/2^+)$	${}^{112}\text{Sn}_{g.s.}$	$p$	1.793	$1g_{9/2}$	0.920
${}^{113}\text{Sb}(11/2^-)$	${}^{112}\text{Sn}_{g.s.}$	$p$	1.702	$1h_{11/2}$	0.920

## 5.5 The effect of breakup and transfer couplings on elastic scattering

Along with the CDCC calculations that includes the projectile excitations described above, the CRC calculations have also been performed simultaneously to include not only the 1p pickup ( ${}^7\text{Li}$ ,  ${}^8\text{Be}$ ) channel but also some of the one-nucleon transfer channels, viz., (i) -1n transfer i.e., ( ${}^7\text{Li}$ ,  ${}^6\text{Li}$ ) reaction and (ii) -1p transfer i.e., ( ${}^7\text{Li}$ ,  ${}^6\text{He}$ ) reaction channels.

The projectile being weakly bound, the direct and resonant breakup of  ${}^7\text{Li}$  into  $\alpha$  and t may play an important role on elastic scattering which in turn will affect on the

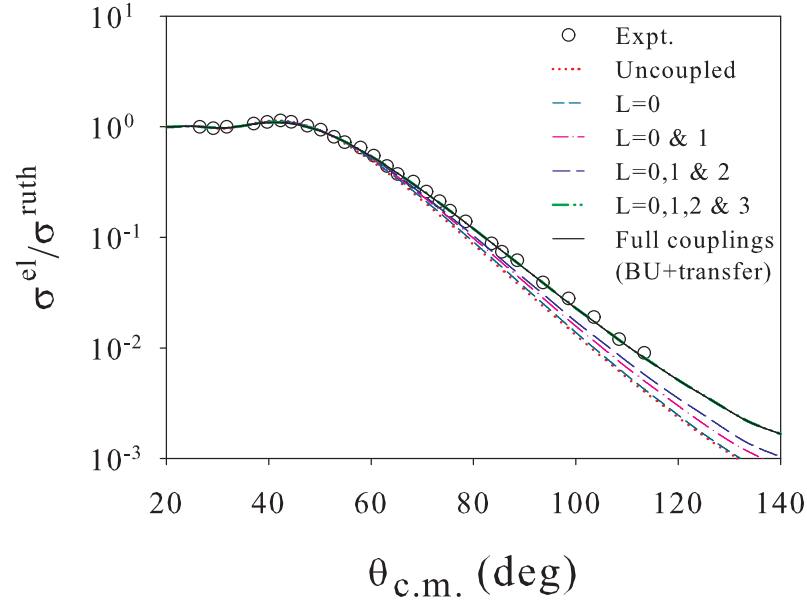


**Figure 5.13** Measured (circles) elastic scattering cross sections have been compared with the FRESKO calculations (lines) showing the effect of coupling of direct and resonant breakup and transfer channels.

+1p transfer channel that we are interested in. The effect of these breakup channels corresponding to different  $\alpha - t$  relative angular momenta on elastic scattering has been demonstrated in Fig. 5.13. The elastic scattering angular distribution calculated using bare CF potential without any breakup or transfer coupling is represented by the dotted line. The calculations with breakup (BU) couplings corresponding to  $\alpha - t$  relative angular momentum (i)  $L=0$  (short-dashed line) (ii)  $L = 0$  and 1 (dash-dot line) (iii)  $L=0, 1$  and 2 (medium dashed line) and (iv)  $L=0, 1, 2$  and 3 (dash-dot-dot line) show that each of these  $\alpha - t$  breakup couplings has reduced the elastic scattering cross sections noticeably at backward angles with respect to the uncoupled cross sections (dotted line). It implies that the couplings have generated a repulsive polarization potential contributing to the effective potential for elastic scattering. Comparison between the results with full couplings, i.e., breakup+transfer couplings (solid line) and the ones with all the  $\alpha + t$  breakup channels (dash-dot-dot line) shows that the effect of transfer coupling on elastic

scattering is unnoticeable. The calculations with full couplings (solid line) provide a good reproduction of the measured elastic scattering angular distribution which is necessary and important while describing the cross sections for non-elastic channels simultaneously using the same set of potential and coupling parameters.

## 5.6 Proximity of breakup to target

To distinguish the breakup events occurring near or far from the target nuclei, two new distributions of the coincidence events have been generated as prescribed by Simpson *et al.* [60]. A direct mapping between the difference of fragment energies  $|E_1 - E_2|$  with their relative energy  $E_{rel}$  and the correlation between the opening angle of the fragments  $\theta_{12}$  and the orientation of their relative velocity of their center of mass  $\beta$  has helped understand the proximity of breakup with respect to the target center. If breakup occurs far from the target both the quantities, i.e.,  $|E_1 - E_2|$  versus  $E_{rel}$  and  $\theta_{12}$  versus  $\beta$  well defined distributions. Any characteristic deviation in the measured distributions compared to the ones expected from these asymptotic behaviors can be utilized to distinguish the breakup events occurring near the target from the ones far from the target. An attempt has been made to investigate the proximity of the breakup for  $2\alpha$  from different resonance states of  ${}^8\text{Be}^*$  to understand the role of transfer breakup on complete fusion suppression and enhancement of incomplete fusion.

### 5.6.1 Distribution of $|E_1 - E_2|$ versus $E_{rel}$

If two breakup fragments have same mass then the maximum difference in energy between the fragments occurs when their relative velocity is aligned with the velocity of their center of mass, such that  $\theta_{12} = 0^\circ$  or  $\theta_{12} = 180^\circ$ . This quantity is given by [60]:

$$|E_1 - E_2| \leq 2\sqrt{E_{rel}(E_1 + E_2 - E_{rel})} \quad (5.6)$$

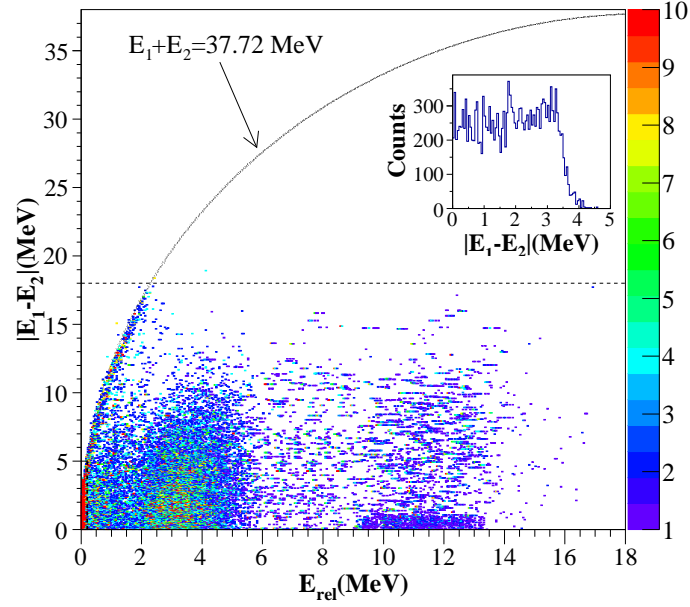


**Figure 5.14** The variation of coincidence events of  $\alpha - \alpha$  with respect to  $|E_1 - E_2|$  versus  $E_{rel}$ . The curved lines represent maximum allowed energy difference  $|E_1 - E_2|$  as a function of relative energy (see text for details). Inset shows the intensity distribution of  $0^+$  state in the range of  $|E_1 - E_2| = 0$  to the maximum allowed  $|E_1 - E_2|^{max} \sim 3.4$  MeV.

If the breakup occurs asymptotically far from the target, the distribution will run from zero to this  $E_{rel}$  dependent maximum. Also, if the decay is isotropic then the intensity of the events is independent of  $|E_1 - E_2|$  for a given relative energy.

The event distributions for  $|E_1 - E_2|$  versus  $E_{rel}$  has been generated from the experimental data and shown in Fig. 5.14. The solid curved line in the figure represents maximum allowed energy difference  $|E_1 - E_2|$  calculated from Eq. 5.6 as a function of relative energy corresponding to  $E_1 + E_2$  with a minimum recoil energy and no excitation of residual target nuclei for both the cases. In Fig. 5.14, the dashed line corresponding to  $|E_1 - E_2| = 18.0$  MeV represents the detection threshold due to detector thickness beyond which no count is expected. From the Fig. 5.14 it is observed that the ground state of  ${}^8\text{Be}$ , with  $E_{rel} \sim 0.092$  MeV, appears in the bottom left corner of the plot and reaches the limiting value of  $|E_1 - E_2|$  and the intensity of these events seems to be independent of  $|E_1 - E_2|$ . Therefore, it can be concluded that the decay of  ${}^8\text{Be}$  into  $2\alpha$  from its ground

state is isotropic and asymptotically far away from the target. For slightly higher value of relative energies it is observed from both the figure that the intensity is no longer constant with  $|E_1 - E_2|$  for a given  $E_{rel}$ . For  $E_{rel}$  in the ranges of  $\sim 2-5$  MeV and  $\sim 9-13$  MeV, the intensity is increasingly focused towards  $|E_1 - E_2|=0$ . As explained in Ref. [60], these events are likely to be from the breakup near the target. Since these  $E_{rel}$  ranges correspond to  $2^+$  and  $4^+$  resonance states of  ${}^8\text{Be}$ , one can conclude that the breakup of  ${}^8\text{Be}$  into  $2\alpha$  from its two resonance states occurs near the target nuclei.

### 5.6.2 Distribution of $\beta$ versus $\theta_{12}$

To further probe the proximity of the breakup events of  ${}^8\text{Be}$ , the correlation between the orientation of the relative velocity  $\beta$  with respect to the opening angle  $\theta_{12}$  has been derived. For a fixed excitation energy  $E^*$ , there is a direct mapping between  $\theta_{12}$  and  $\beta$  [60, 71],

$$\sin\beta = \frac{v_1 v_2 \sin\theta_{12}}{\sqrt{v_2^2 u_1^2 + v_1^2 u_2^2 + 2u_1 u_2 v_1 v_2 \cos\theta_{12}}} \quad (5.7)$$

where,  $v_1$  and  $v_2$  are the velocities in laboratory frame deduced from the measured energies  $E_1$  and  $E_2$ . The fragment velocities in the rest frame of  ${}^8\text{Be}$  are  $u_1$  and  $u_2$ , and they can be deduced from the relation  $E_{rel} = \frac{1}{2}\mu(u_1 + u_2)^2$  and the conservation of momentum, where  $\mu$  is the reduced mass of the breakup fragment pair.

For  $\beta = 90^\circ$ , the opening angle  $\theta_{12}$  is maximum and  $E_1$  is equal to  $E_2$  leading to the symmetric distribution of breakup of  ${}^8\text{Be}$  into two  $\alpha$ , and these events are expected to occur near the target [60, 71]. The smallest  $\theta_{12}$  is generated when  $\beta = 0^\circ$  or  $\beta = 180^\circ$  and for that case the difference of energies  $|E_1 - E_2|$  is maximum.

The experimental fragment angular correlation between  $\beta$  and  $\theta_{12}$  has been shown in Fig. 5.16. It shows three distinct intense bands corresponding to the events of breakup of  ${}^8\text{Be}$  into  $2\alpha$  via its ground,  $2^+$  and  $4^+$  states with  $\theta_{12}$  values in increasing order for any particular  $\beta$  value. The lines plotted in the same figure represent the respective angular correlations obtained from 5.7 assuming  $E_1 = E_2$ , without considering the post Coulomb

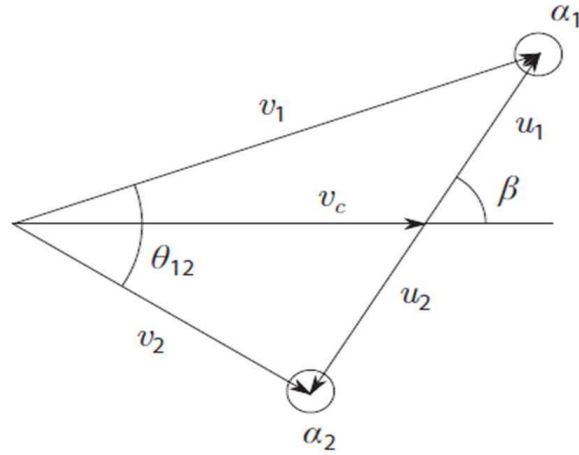


**Figure 5.15** Diagram of orientation of fragment velocities.

acceleration. At smaller  $\theta_{12}$ , the band corresponding to the ground state decay of  ${}^8\text{Be}$  is very close to the asymptotic behavior (shown as a solid line) as expected from 5.7.

However, the second and the third intense bands in the Fig. 5.16, corresponding to  $2^+$  and  $4^+$  states, do not follow the asymptotic trends of disintegration represented by dashed and dotted lines respectively. The experimental distributions are found to peak at  $\beta \sim 90^\circ$ . The spread in  $\theta_{12}$  values corresponding to  $2^+$  state can be understood in terms of multiple excitations of residual target-like nuclei. As suggested in Ref. [60], the contribution in the above spread can also come from (i) different breakup locations relative to the target-like recoil, (ii) the width of the  $2^+$  resonance and (iii) different angular momenta. The long and short dashed line represent expected asymptotic behavior corresponding to g.s. and excited state (14 MeV) of residual target-like nuclei respectively and they cover majority of the second intense band. Thus, the deviation in  $\theta_{12}$  values for  $2^+$  state due to post Coulomb acceleration if any seems to be smaller compared to the above spread.

However, for  $4^+$  state distributions, the  $\theta_{12}$  values ( $\sim 60^\circ$ ) corresponding to majority of the events are smaller than the ones expected from asymptotic breakup (dotted line). Another group of events corresponding to  $4^+$  state, though with small intensity, is observed to have  $\theta_{12}$  values ( $\sim 60^\circ$ ) larger than the ones expected from asymptotic breakup. Such a

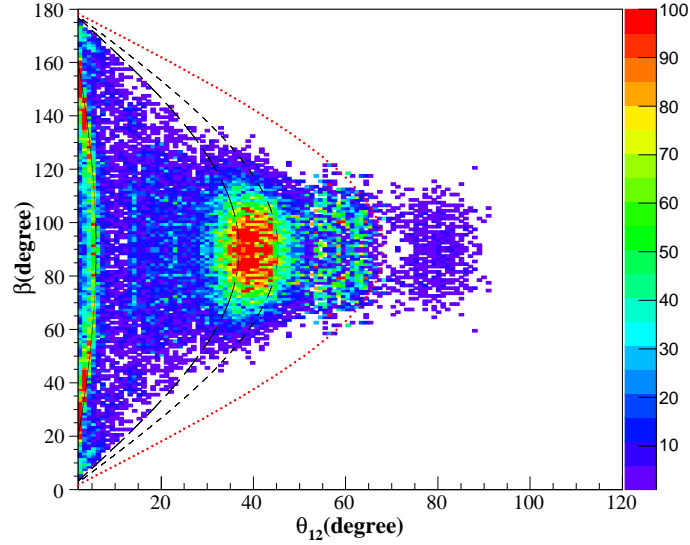


**Figure 5.16** Experimental  $\beta$  versus  $\theta_{12}$  distribution for the breakup of  ${}^8\text{Be}$  into  $2\alpha$ . The lines represent theoretical correlations assuming  $E_1 = E_2$ .

large deviation, i.e., decrease as well as increase, in  $\theta_{12}$  values compared to the asymptotic values are apparently due to the post Coulomb acceleration of breakup fragments for near target breakup events. This is another indication that the breakup of  ${}^8\text{Be}$  via its  $4^+$  resonance state is occurring near the target, where post Coulomb acceleration is modifying the asymptotic correlation. The above deviations visible in the experimental fragment angular correlation from the expected asymptotic behavior makes it an important tool to find the effect of post breakup Coulomb acceleration and distinguish the breakup occurring near to and far from the target.

To understand the experimental events distribution on  $\beta$  further, a Monte-Carlo simulation was performed assuming asymptotic breakup of  ${}^8\text{Be}$  and residual target nuclei at ground state. The fragment angular correlation  $\beta$  versus  $\theta_{12}$  obtained from the simulation for the present detector setup has been shown in Fig. 5.17 for reaction  ${}^{112}\text{Sn}({}^7\text{Li}, {}^8\text{Be} \rightarrow \alpha + \alpha)$ . The projection of the events on  $\beta$  corresponding to  $0^+$ ,  $2^+$  and  $4^+$  events from the simulation has been compared with the experimental data in Fig. 5.18. The smooth continuous line represents a sine curve fitted to the experimental  $\beta$ -distribution. For both experimental and simulated events, the intensity pattern was found to vary as  $\sin\beta$  as

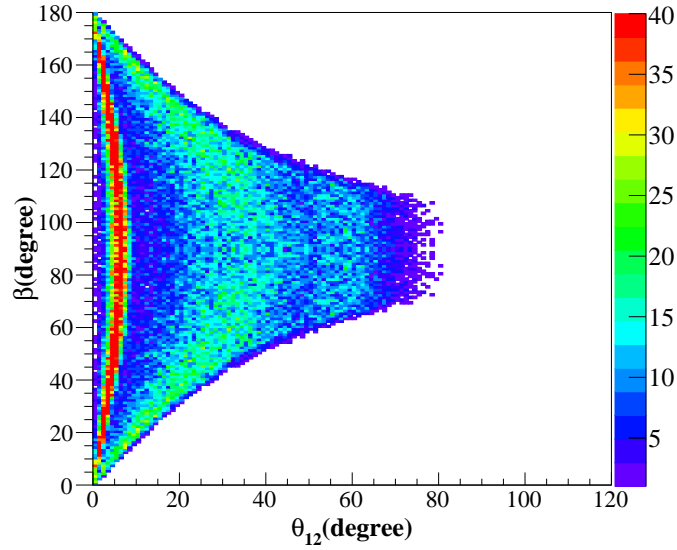


**Figure 5.17** A Monte-Carlo simulation on  $\beta$  versus  $\theta_{12}$  distribution for the breakup of  ${}^8\text{Be}$  into  $2\alpha$  assuming asymptotic breakup for the  ${}^7\text{Li}+{}^{112}\text{Sn}$  reaction, corresponding to the present detector setup.

expected from asymptotic breakup. However for  $2^+$  events, the experimental intensity pattern does not follow  $\sin\beta$  relation but it peaks sharply around  $\beta \sim 90^\circ$ . Due to limited detector coverage for  $4^+$  events, a very small overlapping region of  $\theta_{12}$  could be compared for theory and experiment leading to no definite conclusion on their difference.

## 5.7 Summary and conclusions

In summary, exclusive measurements for various breakup channels consisting of both direct and sequential modes have been carried out using a large strip detector array for  ${}^7\text{Li}+{}^{112}\text{Sn}$  system at a bombarding energy of 30 MeV. The sequential breakup of  ${}^7\text{Li}$  into  $\alpha+t$  through its second resonance state ( $5/2^-$ ) has been measured for the first time along with its first resonance state ( $7/2^-$ ). Exclusive measurement of  $+1p$  transfer breakup channel confirms the observation  $4^+$  resonance breakup state of  ${}^8\text{Be}$  into  $2\alpha$  for the first time along with the well known  $0^+$  and  $2^+$  states.

The measurements of differential cross sections for two more dominating sequential

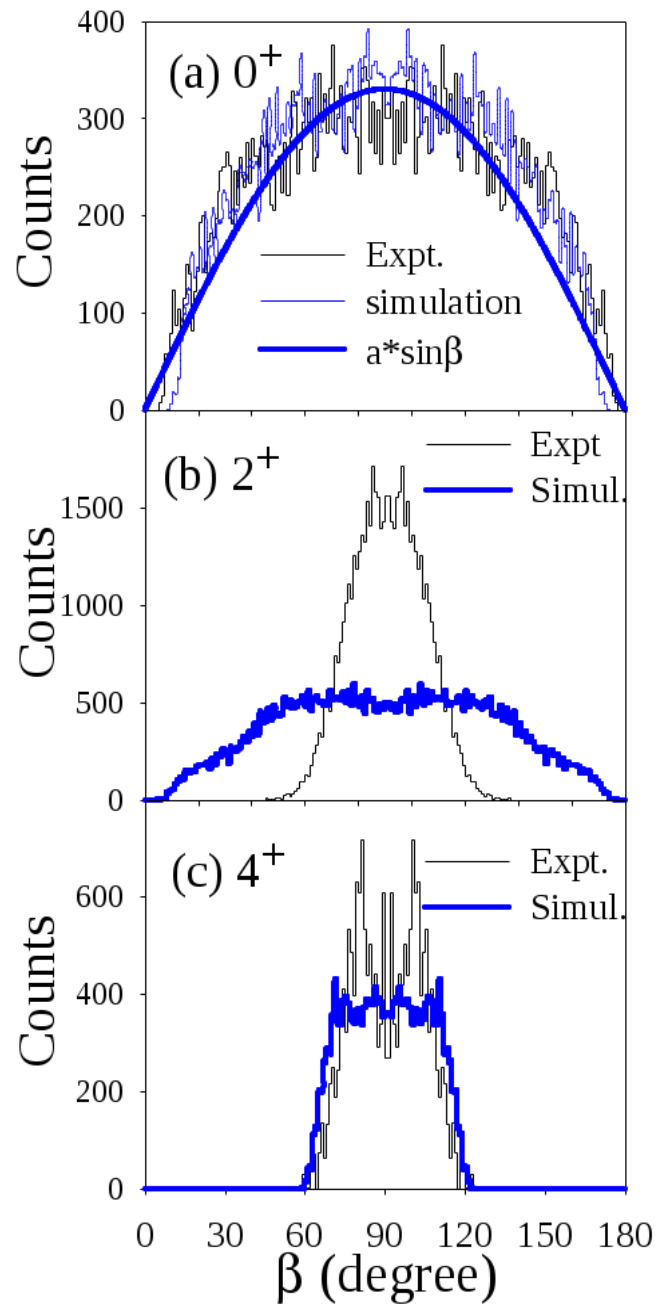


**Figure 5.18** A comparison of simulation with experimental  $\beta$  distribution corresponding to  $0^+$ ,  $2^+$  and  $4^+$  events.

modes proceeding through transfer channels (i)  ${}^7\text{Li} \xrightarrow{-1n} {}^6\text{Li} \rightarrow \alpha + d$  and (ii)  ${}^7\text{Li} \xrightarrow{-2n} {}^5\text{Li} \rightarrow \alpha + p$ , where one of the breakup fragments is  $\alpha$ , show that these channels are very important while calculating the total cross section of the projectile breakup as well as inclusive  $\alpha$ . Thus, the results on (i) direct and resonant breakup of  ${}^7\text{Li}$  into  $\alpha + t$  including the one through the new resonant state ( $5/2^-$ ) of  ${}^7\text{Li}$ , (ii)  $-1n$  transfer followed by breakup into  $\alpha + d$ , (iii)  $-2n$  transfer followed by breakup into  $\alpha + p$  and (iv)  $+1p$  transfer followed by breakup into  $\alpha + \alpha$  presented here provide a good foundation towards the comprehensive understanding of the reaction mechanisms of the projectile breakup as well as the production of large inclusive  $\alpha$  in a reaction involving a weakly bound stable or unstable light projectile.

Further, the observation of direct breakup of  ${}^7\text{Li}$  into  ${}^6\text{He}$  and  $p$  for the first time provides direct evidence of a  ${}^6\text{He}+p$  cluster structure for  ${}^7\text{Li}$ . The present result will initiate refined theoretical modeling by including an additional cluster combination to understand the complete structure of  ${}^7\text{Li}$  and its energy levels.

A simultaneous description of elastic,  $-1n$  transfer,  $-1p$  transfer and  $+1p$  transfer channels have also been attempted using the same set of potential and coupling parameters. The effect of  $\alpha + t$  breakup and transfer couplings on elastic scattering have been investigated. The  $\alpha + t$  breakup channels corresponding to the states with the  $\alpha - t$  relative angular momentum  $L$  ( $=0, 1, 2, 3$ ) are found to increase the elastic scattering at backward angles, though the effect of  $L=3$  is most dominant. The effect of transfer coupling on elastic scattering is found to be negligible. The results of the coupled channels calculations using the CDCC+CRC formalism are found to reproduce simultaneously the experimental cross sections for elastic scattering, transfer and breakup reactions.

An attempt has been made to find out the proximity of  $+1p$  transfer induced breakup to understand the role of transfer breakup of complete fusion suppression and incomplete fusion enhancement if any. From the distributions of  $|E_1 - E_2|$  versus  $E_{\text{rel}}$  and  $\beta$  versus  $\theta_{12}$ , it was observed that the breakup of  ${}^8\text{Be}$  into  $2\alpha$  via its  $0^+$  state occurs far away

from the target-like nucleus whereas the breakup via  $2^+$  and  $4^+$  states occurs close to the target-like nuclei as expected from the lifetime or resonance width of these states [59]. So, it may be concluded that the breakup of  $^8\text{Be}$  through these two states may play a role in CF suppression or ICF enhancement as their occurrences are near the target-like nuclei as well as their breakup time scales are smaller than the collision time scale between the projectile and target. On the other hand, the timescales of breakup through  $0^+$  state being larger and their occurrences are far from the target the incomplete fusion cross sections may not get affected, however, the complete fusion cross section can still be affected depending upon the effect of coupling of this state on interaction potential.

# Chapter 6

## Understanding alpha particle productions in ${}^6\text{Li}+{}^{112}\text{Sn}$ reaction

### 6.1 Introduction

The phenomenon of break-up of weakly bound light nuclei with  $\alpha + x$  cluster structures into its cluster constituents  $\alpha$  and  $x$  while moving in the field of a target nucleus is well-established [5, 9, 37, 48, 57, 58, 60, 71]. It has been observed that the yield of  $\alpha$  particles in such reactions is much higher compared to that of the complementary fragment  $x$ . In an exclusive breakup reaction,  $a + A \rightarrow (b + x) + A$ , the state of the three outgoing fragments ( $b$ ,  $x$  and  $A$ ) is fully determined. But when one or more fragments are not specified, the reaction is said to be inclusive with respect to the unobserved particle(s). The large production of inclusive  $\alpha$  particles compared to  $x$  implies that apart from the process of breaking up of the projectile into two cluster constituents there must exist several additional processes leading to  $\alpha$  productions. However, it is a challenging task to disentangle different reaction channels responsible for such a high yield of inclusive  $\alpha$ . Several attempts [7, 8, 72] have been made to understand the origin of such a large  $\alpha$  cross section but it is far from being fully understood. In the present work, the inclusive  $\alpha$

cross sections for  ${}^6\text{Li}+{}^{112}\text{Sn}$  reaction have been made at several energies and an attempt has been made to disentangle different reaction channels responsible for such large inclusive cross sections by (i) comparing experimental data of different exclusive breakup channels with one of the breakup fragments being  $\alpha$  and (ii) calculating the cross sections for remaining possible  $\alpha$ -producing channels (which are not measured) by the help of the coupled-channels calculations. Another important motivation of the present work is to investigate whether the inclusive- $\alpha$  cross sections for  ${}^6\text{Li}+{}^{112}\text{Sn}$  system follow the same energy dependent systematics as that of the other reactions involving  ${}^6\text{Li}$  projectiles measured earlier. The inclusive cross-sections for other projectile like particles, i.e.,  ${}^3\text{He}$ ,  $t$ ,  $d$  and  $p$  have also been measured. In order to have a consistent coupled-channels calculation with realistic potential and coupling parameters it is desirable to have measured cross sectional data on elastic, inelastic and as many direct reaction channels that can be described simultaneously.

## 6.2 Data analysis and discussion

### 6.2.1 Elastic and inelastic scattering

Typical differential cross sections for the elastic scattering angular distributions normalized to the Rutherford cross sections at  $E_{\text{beam}}=30$  MeV are shown in Fig. 6.1(a). The inelastic cross sections corresponding to  ${}^{112}\text{Sn}(2^+, 1.256$  MeV) and  ${}^{112}\text{Sn}(3^-, 2.355$  MeV) for the same beam energy are shown in Fig. 6.1(b) and (c) respectively. The optical model (OM) analysis using SNOOPY code [73] has been made to fit the elastic scattering data to obtain a total reaction cross section. To include the effect of breakup coupling, continuum discretized coupled channels (CDCC) calculations using the code FRESKO [50] have been performed using cluster-folded (CF) potential in the same way as done in chapter 4. The coupled-channels calculations have been done in two steps to incorporate the effects of both the projectile continuum states and target inelastic excitations. First, the CDCC

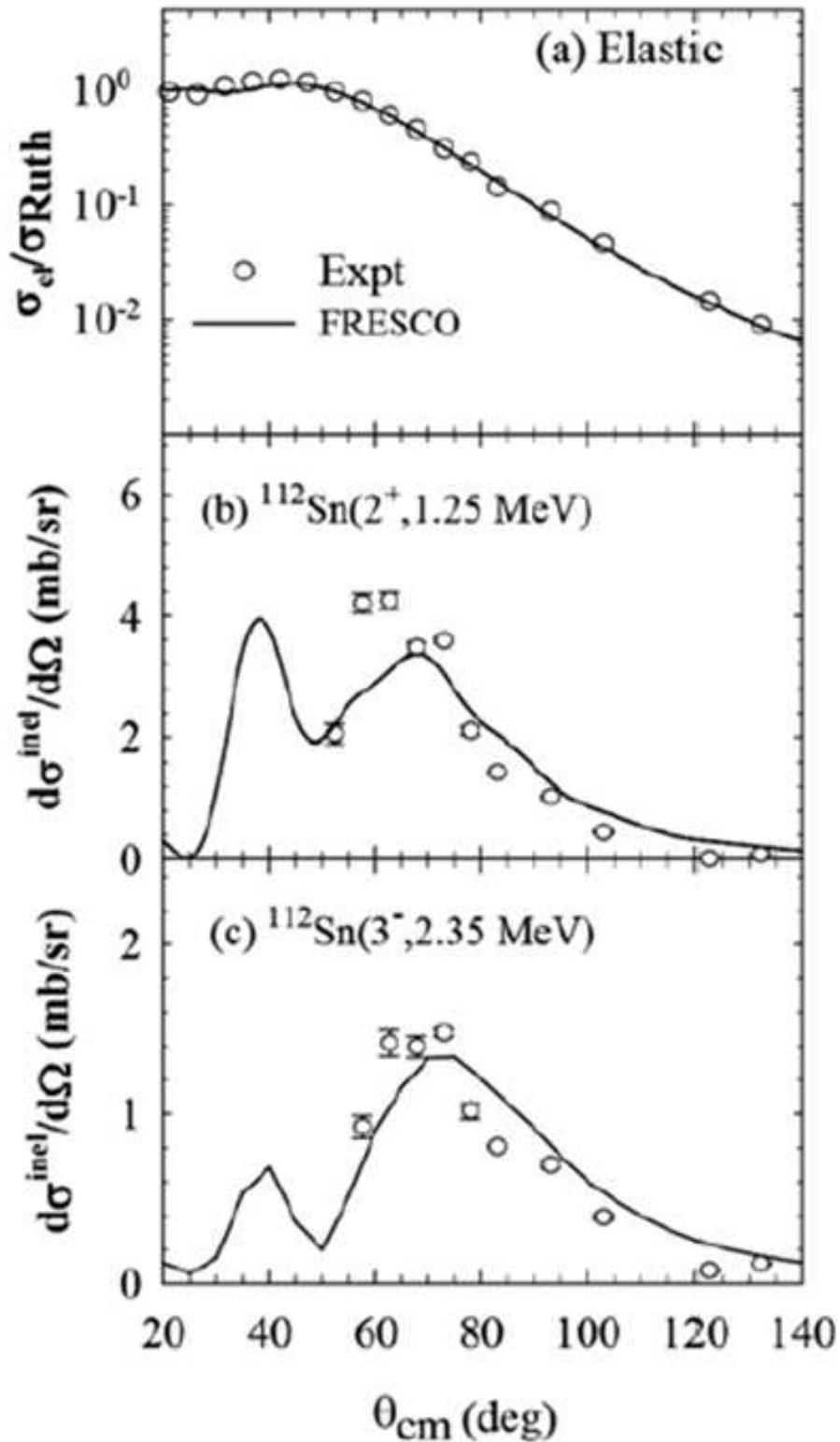


**Figure 6.1** Experimental differential cross sections for (a) elastic scattering and (b, c) inelastic scattering corresponding to  $(2^+, 1.256 \text{ MeV})$  and  $(3^-, 2.35 \text{ MeV})$  excited states of  ${}^{112}\text{Sn}$  respectively. Solid lines correspond to the results of coupled-channels calculations using FRESKO.

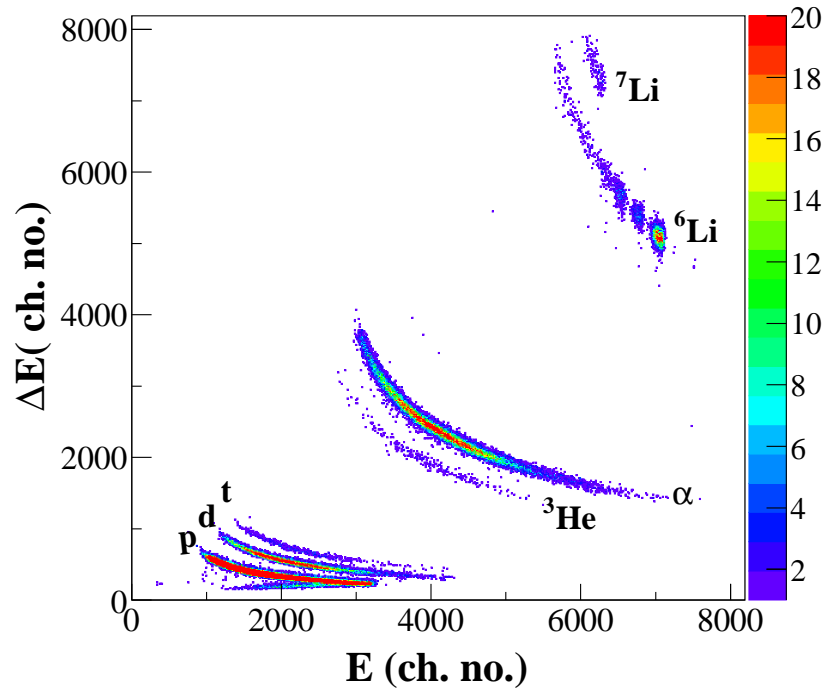


**Figure 6.2** A typical two-dimensional raw spectrum of a telescope placed at  $105^\circ$  and  $E_{\text{beam}} = 30$  MeV.

calculations are performed. Next, CDCC generated polarization potential is added to CF potential to get an effective potential which in turn is used in the coupled reaction channels (CRC) calculations by FRESKO including the elastic and target inelastic states. The coupling parameters available in the literature [74, 75] have been used for the two inelastic states. The results of the fresco calculations along with the measured data are shown in Fig. 6.1 as solid lines. These data on elastic and inelastic scattering cross sections [76] have been used as constraints in the detailed CRC calculations that provide the theoretical estimates of different transfer triggered breakup channels contributing to inclusive  $\alpha$  production. The description on the measured inclusive  $\alpha$  cross section and a study on possible origins of these  $\alpha$  particles are described in the following subsections.

### 6.2.2 Inclusive $\alpha$

The experimental inclusive  $\alpha$  cross sections are derived from the measured  $\alpha$  spectra. Fig. 6.3 shows typical 1D projections of  $\alpha$ -spectra measured at near the grazing angles for several incident beam energies. It can be observed from the Fig. 6.3 that the measured  $\alpha$ -spectra show peaks around two-third of beam energies. This implies that the above particles are mainly produced by projectile breakup mechanisms [7]. A statistical model calculation using PACE shows that the spectra of  $\alpha$  evaporation from complete fusion may contaminate the above spectra but their contributions are much smaller and peak at lower energies as shown by red lines in Fig. 6.3. Yields of  $\alpha$  particles under these peaks have been used to obtain the angular distribution of inclusive  $\alpha$  for five different energies (22, 24, 26, 28 and 30 MeV) as shown in Fig. 6.4 respectively.

The measured angular distribution data are first fitted with arbitrary functions by  $\chi^2$  minimization as shown by lines in Fig. 6.4. The fitted curves are used to obtain the angle integrated cross-sections which are then compared with the total reaction cross-section obtained from the fitting of elastic data using FRESKO. It shows that inclusive breakup  $\alpha$  is one of the major reaction channels at energies near and above the Coulomb barrier. So it would be highly interesting to estimate the  $\alpha$  contribution from all possible channels in order to understand the origin of such a large inclusive- $\alpha$  for the present system.

### 6.2.3 Disentangling $\alpha$ contributions

To disentangle the production of such a large cross-section of  $\sigma_{\alpha}^{incl}$ , the coupled-channels calculations have been performed as described in chapter 4. As the coupled channel calculations successfully explains the experimental breakup data, hence the same set of parameters were used for the other energies to extract the cross-sections of dominant breakup channels that are responsible for high  $\alpha$  production. The contributions of the dominant breakup channels responsible for inclusive  $\alpha$  production are shown in Fig. 6.5. It was identified that the major channels producing  $\alpha$  particles due to non-capture breakup

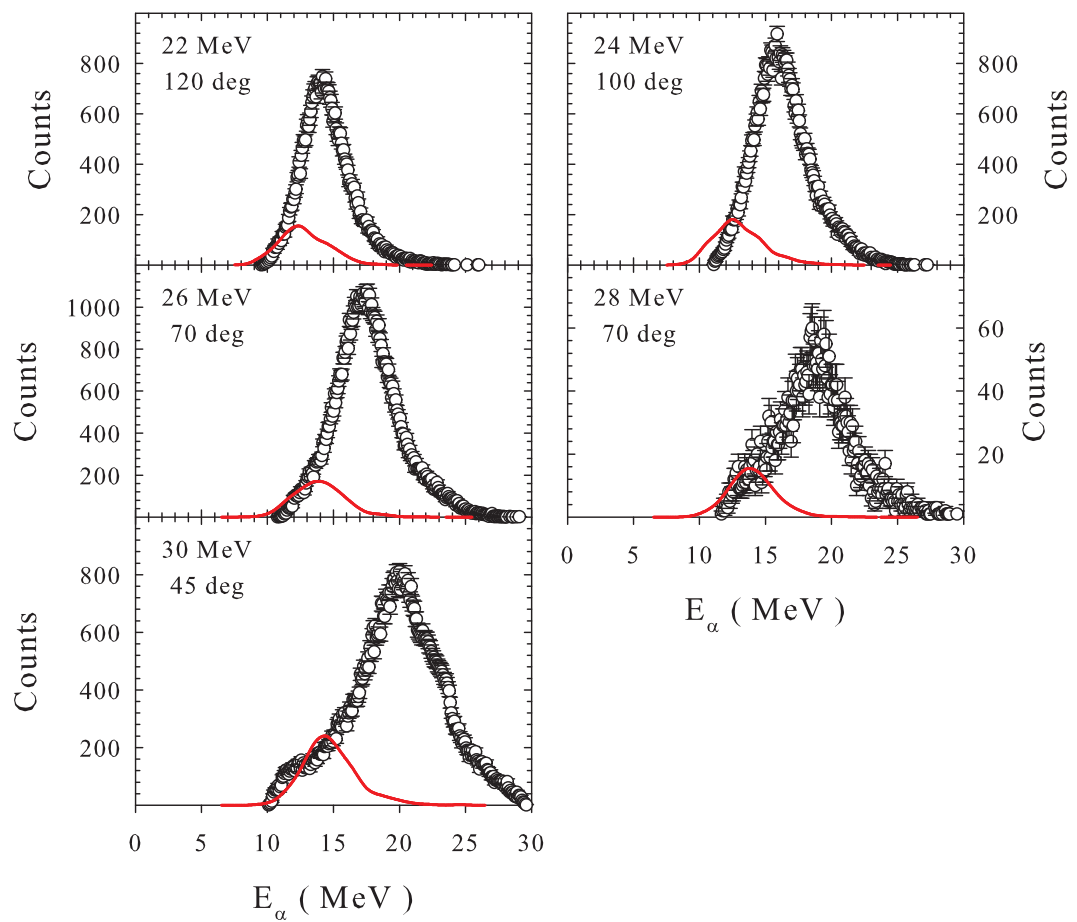


**Figure 6.3** Inclusive  $\alpha$  spectra at  $\theta \sim \theta_{gr}$  for different bombarding energies.

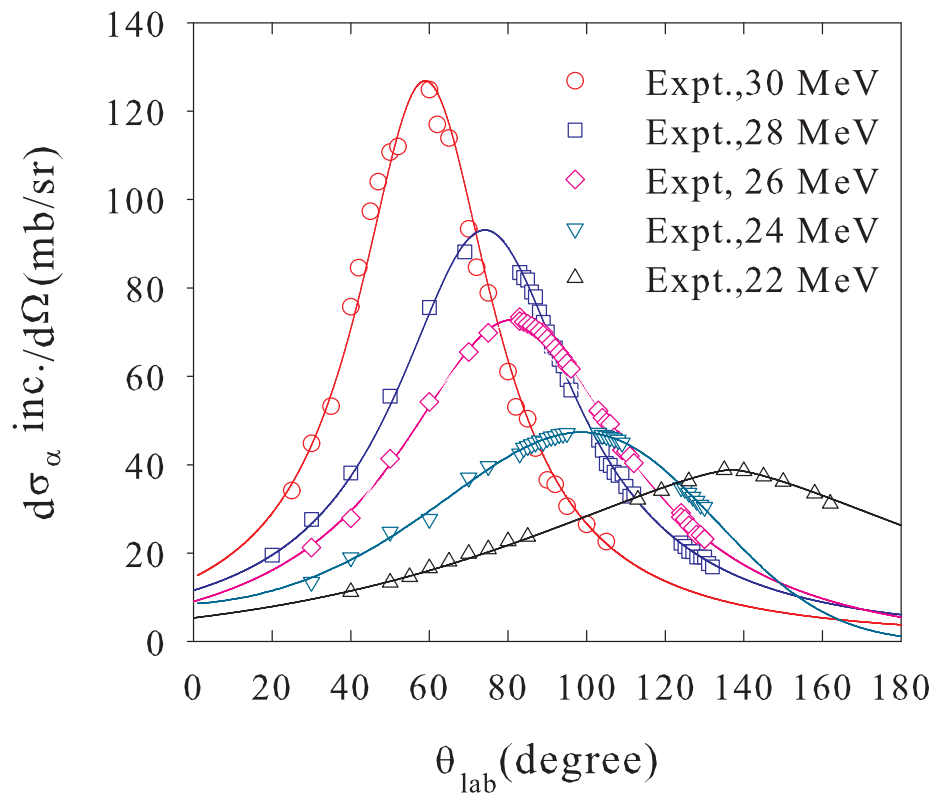


**Figure 6.4** Inclusive  $\alpha$  angular distribution for  ${}^6\text{Li}+{}^{112}\text{Sn}$  at energies  $E_{lab} = 22\text{-}30$  MeV. Lines are  $\chi^2$  minimized fit to the data and used to obtain the angle integrated cross sections.

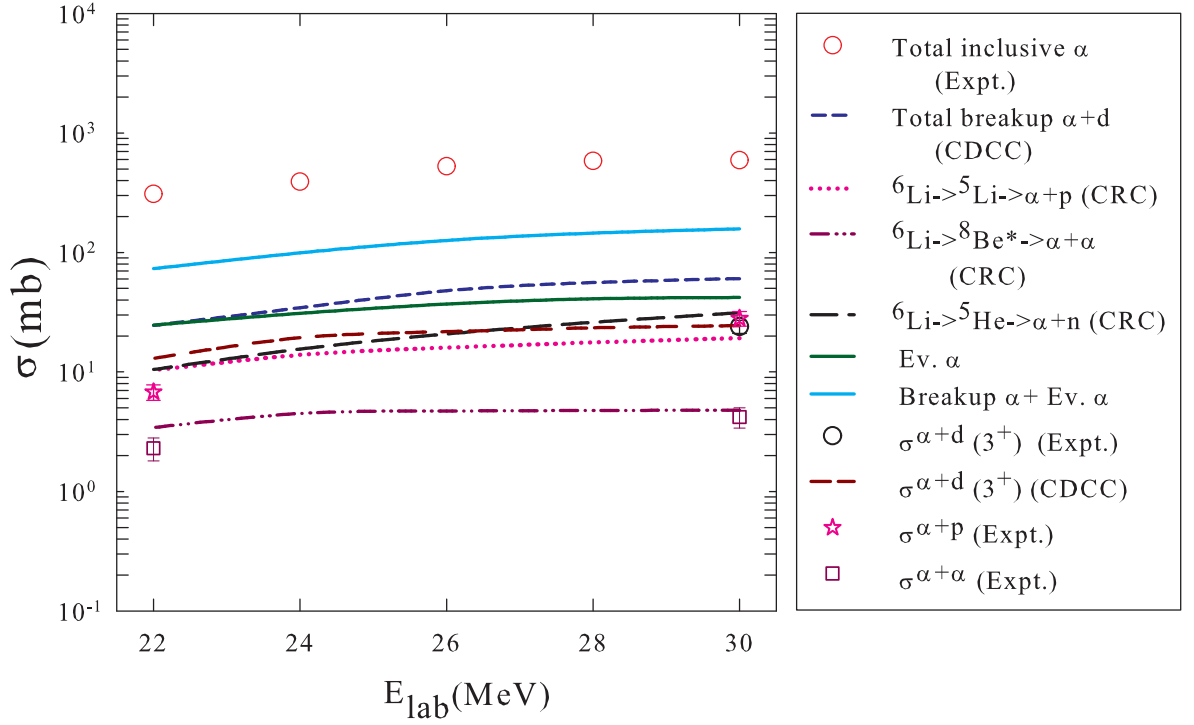


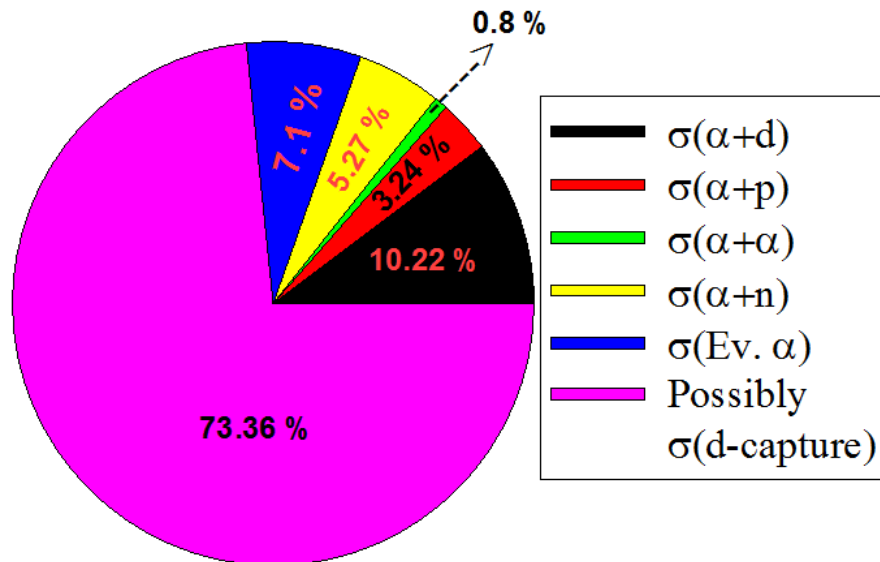
**Figure 6.5** Inclusive  $\alpha$  (circles, present data) and  $\alpha$  contributions from different transfer and breakup channels for different beam energies.

are (i) direct and resonant break-up of  ${}^6\text{Li} \rightarrow \alpha + d$  (ii)  $1n$  stripping ( ${}^6\text{Li}, {}^5\text{Li}$ ) followed by break-up i.e.,  ${}^5\text{Li} \rightarrow \alpha + p$  (iii)  $1d$  pickup ( ${}^6\text{Li}, {}^8\text{Be}$ ) followed by break-up i.e.,  ${}^8\text{Be} \rightarrow \alpha + \alpha$  (iv)  $1p$  stripping ( ${}^6\text{Li}, {}^5\text{He}$ ) followed by break-up i.e.,  ${}^5\text{He} \rightarrow \alpha + n$ . The contribution from  $1n$  pick-up followed by breakup into  $\alpha + t$  is found to be negligible. Apart from the above mentioned channels the inclusive- $\alpha$  can also be produced from the decay of compound nucleus produced by the complete fusion, i.e.,  ${}^6\text{Li} + {}^{112}\text{Sn} \rightarrow {}^{118}\text{I}^* \rightarrow$  subsequent decay. The contribution of evaporated  $\alpha$  has been estimated with the help of statistical model code PACE4 [77]. The comparison of the cross-sections for different beam energies are shown in Fig. 6.5 and also in Table 6.1.

It has been observed that the total breakup  $\alpha$  produced by all the above channels along with the evaporated  $\alpha$  explains only 24% to 27% of the total inclusive- $\alpha$ . Hence, there are other channels responsible for the production of such a large inclusive- $\alpha$ . One of

**Table 6.1** Calculated cross-sections for various channels producing  $\alpha$  at  $E_{\text{beam}} = 22\text{--}30$  MeV.

$E$ (MeV)	$\sigma_{\text{reac}}^{CDCC}$ (mb)	$\sigma_{\alpha}^{\text{incl}}$ (mb)	$\sigma_{\alpha+d}^{CDCC}$ (mb)	$\sigma_{\alpha+p}^{CRC}$ (mb)	$\sigma_{\alpha+\alpha}^{CRC}$ (mb)	$\sigma_{\alpha+n}^{CRC}$ (mb)	$\sigma_{\text{Ev.}\alpha}^{PACE4}$ (mb)
30.0	1344	592 $\pm 35$	60.5	19.2	4.79	31.2	42.0
28.0	1175	584 $\pm 32$	55.9	17.65	4.77	26.0	41.0
26.0	978	527 $\pm 28$	47.8	15.96	4.72	20.75	37.0
24.0	698	392 $\pm 21$	34.4	13.88	4.49	15.52	31.0
22.0	493	309 $\pm 16$	24.5	10.32	3.43	10.45	24.0

**Figure 6.6** The individual contribution of different breakup channels leading to inclusive  $\alpha$  for 30 MeV beam energy.

the major contributions can also come from the breakup of  ${}^6\text{Li}$  into  $\alpha+d$  followed by the capture of the fragment  $d$  by the target as observed in [42]. The individual contribution of different breakup channels leading to inclusive  $\alpha$  for 30 MeV beam energy is depicted in Fig. 6.6 via the pie-chart.

### 6.2.4 Systematics of inclusive breakup $\alpha$

To test the universality of the inclusive breakup  $\alpha$  production in the reactions involving the weakly bound  ${}^6\text{Li}$  projectile and targets with different masses and atomic numbers such as (i)  ${}^6\text{Li} + {}^{28}\text{Si}$  [78] (ii)  ${}^6\text{Li} + {}^{59}\text{Co}$  [79], (iii)  ${}^6\text{Li} + {}^{90}\text{Zr}$  [80], (iv)  ${}^6\text{Li} + {}^{58}\text{Ni}, {}^{118,120}\text{Sn}$  [43], (v)  ${}^6\text{Li} + {}^{112}\text{Sn}$  (present data), (vi)  ${}^6\text{Li} + {}^{208}\text{Pb}$  [46] and (vii)  ${}^6\text{Li} + {}^{209}\text{Bi}$  [42], the corresponding inclusive alpha cross sections have been compared in Fig. 6.7 as a function of normalized energy ' $E_{c.m.}/[Z_p Z_t / (A_p^{1/3} + A_t^{1/3})]$ '. Here  $Z_p$  ( $Z_t$ ) and  $A_p$  ( $A_t$ ) are atomic number and atomic masses of the projectile (target), respectively. Interestingly, it is observed that the inclusive  $\alpha$  cross section with reduced energy for all the above systems follow a universal curve as observed in Refs [42, 78, 80].

Assuming the  $\alpha$  production to be the dominant direct reaction mechanism, in other words all the channels producing  $\alpha$  particles to be the dominant direct reactions, the difference between the total reaction cross section  $\sigma_{\text{reac}}$  obtained from the OM analysis and the inclusive alpha cross section  $\sigma_{\alpha}^{\text{incl}}$ , i.e., " $\sigma_{\text{reac}} - \sigma_{\alpha}^{\text{incl}}$ " should be equal to complete fusion cross section. The above quantity for three different systems i.e.,  ${}^6\text{Li} + {}^{209}\text{Bi}$ ,  ${}^{90}\text{Zr}$ ,  ${}^{59}\text{Co}$ , have been derived and shown in Fig. 6.8 as hollow circles, which indeed found to be close to the experimental complete-fusion cross-sections (filled circles). It suggests that  $\alpha$  production channels are indeed the main contributors to the total direct reaction cross sections.

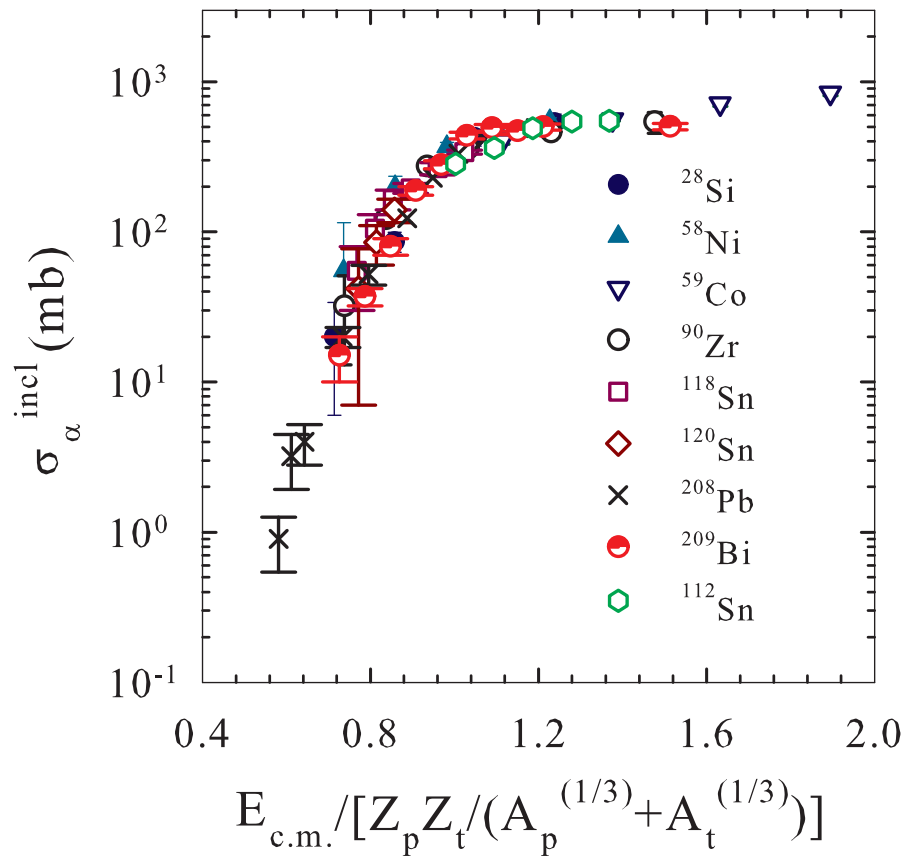


**Figure 6.7** Inclusive breakup  $\alpha$  cross sections involving  ${}^6\text{Li}$  projectile with several different targets including  ${}^{112}\text{Sn}$  (present data) as a function of reduced energy.

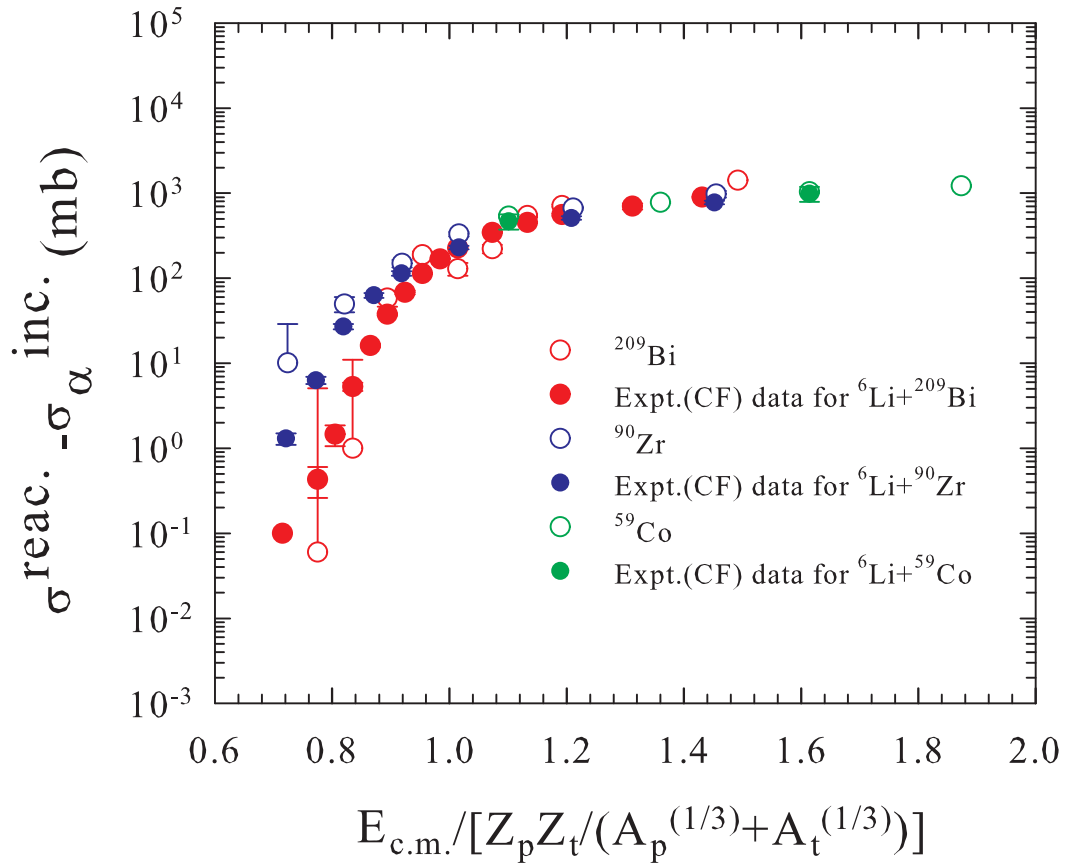


**Figure 6.8** Variation of ' $\sigma^{\text{react.}} - \sigma_{\alpha}^{\text{inc.}}$ ' with normalized energy ' $E_{\text{c.m.}}/[Z_p Z_t / (A_p^{1/3} + A_t^{1/3})]$ ' for  ${}^6\text{Li} + {}^{209}\text{Bi}$ ,  ${}^6\text{Li} + {}^{90}\text{Zr}$  and  ${}^6\text{Li} + {}^{59}\text{Co}$  are represented by red, blue and green hollow circles respectively. The filled circles with same colour represents the CF cross-section for the respective system at that normalized energy.

### 6.2.5 Cross-section of inclusive ${}^3\text{He}$ , $t$ , $d$ and $p$

From the two dimensional ( $\Delta E$  versus  $E_{total}$ ) plot as shown in Fig. 6.2 it is observed that  ${}^3\text{He}$ ,  $t$ ,  $d$  and  $p$  are also produced during the interaction of  ${}^6\text{Li}$  and  ${}^{112}\text{Sn}$ . The particles have also been found to have produced in  $t$ ,  $d$ ,  $p$  can also come in coincidence with  $\alpha$  by the direct or sequential breakup processes. If the breakup processes are non-capture type then both the breakup fragments can be detected in coincidence. It may also happen that after breakup, the fragment  $\alpha$  is getting captured by the target yielding only  $t$ ,  $d$  and  $p$  in outgoing channels.

The dissociation of  ${}^6\text{Li}$  into  ${}^3\text{He}+t$  can be responsible for both  ${}^3\text{He}$  and  $t$  production. It may also happen that the  ${}^3\text{He}$  is produced through the direct transfer of  $t$  from  ${}^6\text{Li}$  to the target, similarly  $t$  can also be produced from the direct transfer of  ${}^3\text{He}$  from  ${}^6\text{Li}$  to the target. It is very difficult to distinguish between the breakup followed by capture and the direct transfer process. As the breakup threshold of  ${}^6\text{Li}$  into  ${}^3\text{He}+t$  is large (approximately 16 MeV) as compared to the fragment-capture, so the production of  ${}^3\text{He}$  and  $t$  are presumed to be from cluster transfer-process [7].

The angular distribution of cross-section for different ejectiles i.e  ${}^3\text{He}$ ,  $t$ ,  $d$  and  $p$  are shown in Fig 6.9 (a), (b), (c) and (d) respectively. The solid lines are the best fitted curve. The angle integrated cross-sections have been given in Table 6.2.

## 6.3 Summary and conclusions

The differential cross sections for elastic, inelastic and inclusive  $\alpha$ ,  ${}^3\text{He}$ ,  $t$ ,  $d$  and  $p$  have been measured for  ${}^6\text{Li}+{}^{112}\text{Sn}$  system at a beam energy of 30 MeV. Coupled-channels calculations are performed to include the effect of projectile breakup and target excitations and transfer channels. The normalized cluster-folded potential that explains simultaneously the elastic and two inelastic states are used to calculate the projectile breakup cross sections.

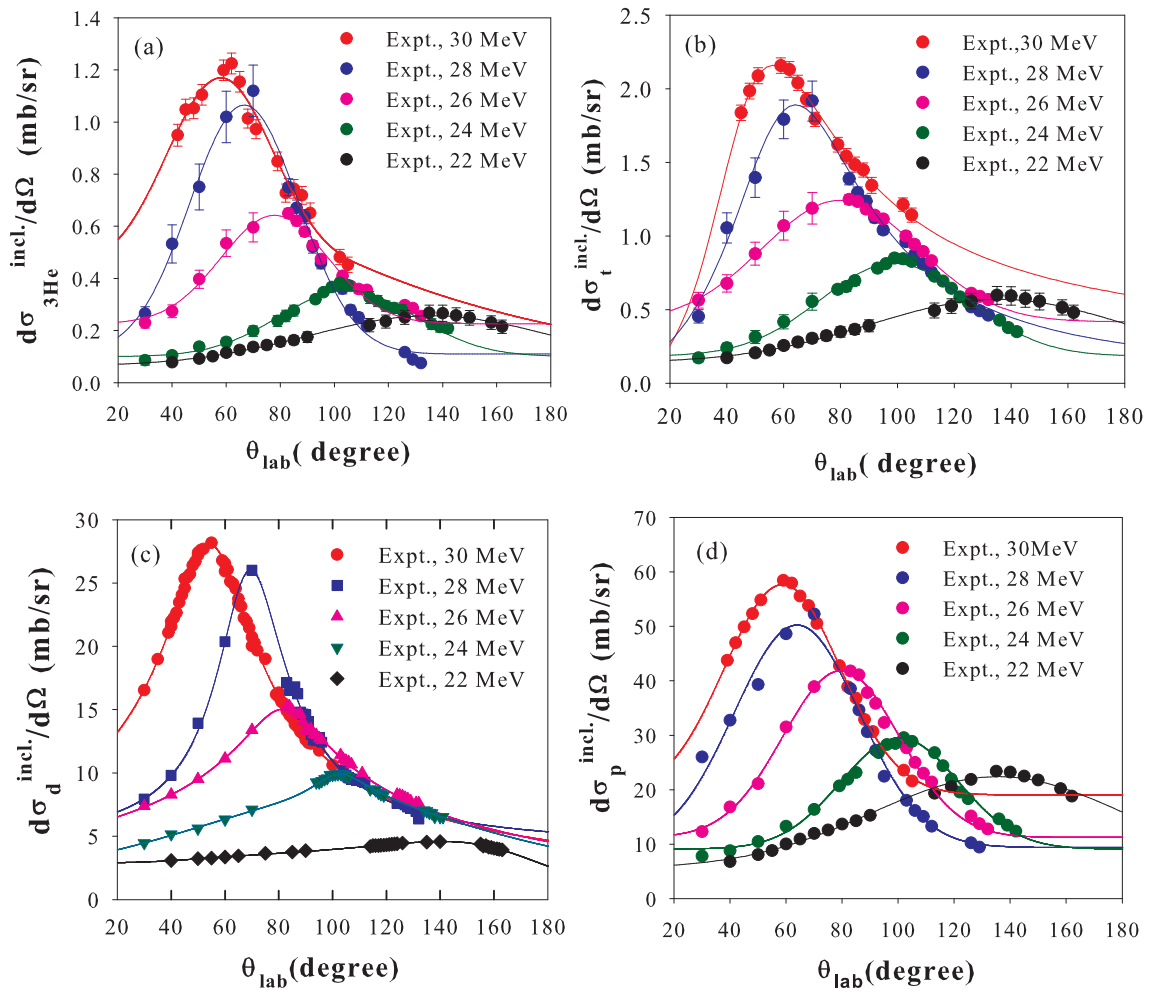


**Figure 6.9** Inclusive (a)  ${}^3\text{He}$ , (b)  $t$ , (c)  $d$  and (d)  $p$  cross-sections at energies  $E_{\text{beam}}=22\text{-}30$  MeV.

**Table 6.2** Experimental integrated cross-sections for  ${}^3\text{He}$ ,  $t$ ,  $d$  and  $p$  at  $E_{beam} = 22-30$  MeV.

$E$ (MeV)	$\sigma({}^3\text{He})$ (mb)	$\sigma(t)$ (mb)	$\sigma(d)$ (mb)	$\sigma(p)$ (mb)
30.0	8.3 $\pm 0.7$	15.8 $\pm 0.6$	178 $\pm 12$	414 $\pm 21$
28.0	5.9 $\pm 0.6$	12.6 $\pm 1.2$	156 $\pm 11$	326 $\pm 16$
26.0	4.9 $\pm 0.5$	10.7 $\pm 1.1$	126 $\pm 9$	302 $\pm 16$
24.0	2.8 $\pm 0.3$	6.34 $\pm 0.6$	88.8 $\pm 6$	222 $\pm 15$
22.0	2.2 $\pm 0.3$	4.82 $\pm 0.5$	46.4 $\pm 4$	189 $\pm 13$

Inclusive breakup  $\alpha$  cross sections for  ${}^6\text{Li}+{}^{112}\text{Sn}$  reaction have been measured at several additional energies (22, 24, 26 and 28 MeV) around the Coulomb barrier. The cross section for the inclusive  $\alpha$  was found to be a significant fraction of the total reaction at all the energies, and at sub-barrier energies it exhausts almost whole of the reaction cross section.

It has been observed that the total breakup  $\alpha$  along with the evaporated  $\alpha$  explains only 24% to 27% of the total inclusive- $\alpha$ . This implies that the dominant contribution may originate from d-capture reaction as observed in [42].

A systematic of inclusive  $\alpha$  cross section for several reactions involving  ${}^6\text{Li}$  as a projectile with different targets reveals that they fall on a universal curve as a function of normalized energy.

# Chapter 7

## Summary and future outlooks

The reaction dynamics involving weakly bound nucleus  ${}^{6,7}\text{Li}$ , populating the non-resonant and resonant continuum states, has been investigated. In the first part of the investigation, we have studied the non-capture breakup reaction processes of  ${}^6\text{Li}$ , where none of the breakup fragments are captured by the target and can be detected in coincidence. In the second part, an investigation similar to the first part but involving  ${}^7\text{Li}$  as the projectile has been studied. In the third part, an attempt has been made to understand the sources of large inclusive  $\alpha$  cross section in the  ${}^6\text{Li}+{}^{112}\text{Sn}$  reaction at several energies by comparing all the experimental breakup cross sections (where  $\alpha$  is one of the breakup fragments) that are measured in the first part of the present thesis work and the theoretical estimations of the remaining possible reaction channels contributing to the  $\alpha$ -yield.

### 7.1 Summary

The present thesis work deals with the understanding of breakup reactions of weakly bound stable projectiles  ${}^{6,7}\text{Li}$  by medium mass nuclei  ${}^{112}\text{Sn}$ . Since  ${}^{6,7}\text{Li}$  nuclei have very low breakup threshold, similar to some of the exotic nuclei near drip lines, the study of the reaction mechanism involving these nuclei will be very useful to understand some of the important features of the reactions involving exotic nuclei. From the present study,

it is observed that  ${}^6\text{Li}$  ( ${}^7\text{Li}$ ) not only breaks into its cluster constituents  $\alpha + d(t)$ , but also exchange some nucleons with the target before forming the quasi-bound nuclei which subsequently break into  $\alpha + y$  particles, where ‘ $y$ ’ can be an  $\alpha$ ,  $d$ ,  $p$ , etc. In order to capture all the breakup fragments a large area silicon strip detector (telescope) array has been setup and used for the experiments at BARC-TIFR Pelletron-LINAC Facility, Mumbai. A Monte Carlo Simulation Code has been developed in C++ to find out the efficiency of the strip detector array. A simulation using GEANT4 has also been performed for the same purpose. Several kinematic correlation techniques are used to identify the breakup fragments in coincidence and compared with the simulation.

Exclusive measurements of all the dominant breakup modes producing charged particles in the outgoing channels have been made. Several interesting results are observed for the first time in the measurements involving both the systems, i.e.,  ${}^6\text{Li}+{}^{112}\text{Sn}$  and  ${}^7\text{Li}+{}^{112}\text{Sn}$ . For the first time, we have observed  $\alpha + d$  breakup through the  $1^+$  resonant state of  ${}^6\text{Li}$  [57],  $\alpha + t$  breakup through  $5/2^-$  resonant state of  ${}^7\text{Li}$  [58], and  $\alpha + \alpha$  breakup through  $4^+$  resonant state of  ${}^8\text{Be}$  [61]. Also, we have observed the breakup of  ${}^7\text{Li}$  into  ${}^6\text{He}+p$  for the first time suggesting the possibility of another cluster structure of  ${}^7\text{Li}$  as  ${}^6\text{He}+p$  apart from its well-known  $\alpha + t$  cluster [58]. The cross-section for each breakup process is evaluated with the help of simulation code and also by using the Jacobian and the results have been compared with the theoretical cross sections calculated using the standard coupled-channels code FRESKO. The detailed study of resonant, direct and transfer induced breakup into fragments via different resonant states provides a good foundation towards understanding the reaction mechanisms of total  $\alpha$  production, the sequential modes of projectile breakup and their impact on fusion cross sections.

## 7.2 Future outlooks

In near future it will be interesting to stretch out the present study to explore the other reaction channels that could not be investigated in this thesis work. The investigation

of these channels may require enhanced detection system. Some of the possibilities are listed below:

**(i) Breakup processes leading to neutron in the outgoing channel:**

The breakup of projectile-like fragment into *neutron* +  $x$  (e.g.  ${}^5\text{He} \rightarrow \alpha + n$ ,  ${}^6\text{He} \rightarrow \alpha + n + n$ ,  ${}^7\text{Li} \rightarrow {}^6\text{Li} + n$ ,  ${}^8\text{Li} \rightarrow {}^7\text{Li} + n$ ) are of particular interest. These reaction processes can be studied from a coincidence measurement between the out going neutrons and charged particles using the segmented large area double sided silicon strip detector array along with the neutron detector array.

**(ii) Study of nuclear astrophysics using breakup study:**

The determination of cross section for charged particle reactions is of particular importance for nuclear astrophysics. Reaction rates serve as input to various astrophysical models such as primordial nucleosynthesis or stellar evolution. Ideally cross sections are measured directly in experiments, however, in most cases a direct measurement is very difficult or even impossible at the relevant small energies since cross sections become very small because of Coulomb repulsion of the interacting particles. Often one has to rely on the extrapolation of the cross section to small energies. Alternative methods have been proposed where the considered reaction is not studied directly but a closely related process can be measured in the laboratory.

In the case of radiative capture reactions the Coulomb dissociation method has been used successfully as an indirect method in recent years. Here, the inverse reaction to radiative capture i.e. the breakup of the nucleus produced in the fusion process, is studied during the scattering on a highly charged target, which supplies the necessary photons through its Coulomb field. From the dissociation cross section the astrophysical  $S$  factor of the capture reaction can be extracted with the help of nuclear reaction theory.

We have performed an experiment recently using  ${}^{6,7}\text{Li}$  as projectiles to find out the astrophysical  $S$  factor from the breakup of  ${}^6\text{Li}$  and  ${}^7\text{Li}$  in the Coulomb field region and also to find out the relative abundances of  ${}^6\text{Li}$  and  ${}^7\text{Li}$  in order to understand the  ${}^{6,7}\text{Li}$

puzzle in Big Bang nucleosynthesis.

**(iii) Study of nuclear reaction using RIB**

We know that the weakly bound stable projectiles; like  ${}^6,7\text{Li}$  and  ${}^9\text{Be}$ , show somewhat similar behaviour (such as low breakup threshold and core+valence cluster structure) as that of the exotic nuclei. So the detection system along with kinematic correlation used for the identification of different resonant states will be useful to in the present thesis work probe the exotic nuclei like  ${}^6\text{He}$ ,  ${}^8\text{Li}$ ,  ${}^{11}\text{Li}$ . The direct study of breakup mechanism of these exotic nuclei with enhanced detection system along with Monte Carlo simulation will further shed light into the possibility of additional cluster structures, new resonances, etc., and provide better understanding of the detailed reaction mechanisms.

# References

- [1] J. D. Cockcroft and E. T. S. Walton , Nature, 129 (3261), 649 (1932).
  
- [2] D. Allan Bromley, Treatise on Heavy Ion Sciences, Volume 1: Elastic and Quasi-elastic scattering, Plenum Press, (1984).
  
- [3] J. F. Miller, J. G. Hamilton, T. M. Purnam, H. R. Haymond, and G. B. Rossi, Phys. Rev **80**, 486 (1950).
  
- [4] D. H. Luong, M. Dasgupta, D. J. Hinde, R. du Rietz, R. Rafiei, C. J. Lin, M. Evers, and A. Diaz-Torres, Phys. Lett. B **695**, 105 (2011).
  
- [5] S. Santra, V. V. Parkar, K. Ramachandran, U. K. Pal, A. Shrivastava, B. J. Roy, B. K. Nayak, A. Chatterjee, R. K. Choudhury, and S. Kailas, Phys. Lett. B **677**, 139 (2009).
  
- [6] A. Shrivastava, A. Navin, N. Keeley, K. Mahata, K. Ramachandran, V. Nanal, V. V. Parkar, A. Chatterjee, and S. Kailas, Phys. Lett. B **633**, 463 (2006).

- [7] C. M. Castaneda, H. A. Smith Jr., P. P. Singh, J. Jastrzebski, H. Karwowski, and A. K. Gaigalas, *Phys. Rev. C* **21**, 179 (1980).
- [8] C. Signorini, A. Edifizi, M. Mazzocco, M. Lunardon, D. Fabris, A. Vitturi, P. Scopel, F. Soramel, L. Stroe *et al.*, *Phys. Rev. C* **67**, 044607 (2003).
- [9] D. H. Luong, M. Dasgupta, D. J. Hinde, R. du Rietz, R. Rafiei, C. J. Lin, M. Evers, and A. Diaz-Torres, *Phys. Rev. C* **88**, 034609 (2013).
- [10] <https://www.nucleonica.com>.
- [11] Sonia Bacca, *Eur. Phys. J. Plus* **131**, 107 (2016).
- [12] Hans Paetz gen. Schieck *Key Nuclear Reaction Experiments Discoveries and consequences* IOP Publishing, Bristol, UK.
- [13] J. S. Vaagen, D. K. Gridnev, H. Heiberg-Andersen, B. V. Danilin, S. N. Ershov, V. I. Zagrebaev, I. J. Thompson, M. V. Zhukov, and J. M. Bang, *Physica Scripta* **2000**, 209 (2000).
- [14] S. Abrahamyan *et al.* (PREX Collaboration), *Phys. Rev. Lett.* **108**, 112502 (2012).
- [15] Adrien Matta. Etude du noyau trs riche en neutrons  $^{10}\text{He}$  par raction de transfert dun proton  $^{11}\text{Li}(d, ^3\text{He})$ . Autre [cond-mat.other]. Universit Paris Sud - Paris XI,

2012. Franais. <NNT :2012PA112032>. <tel-00684544>.
- [16] K. Hagino, I. Tanihata, and H. Sagawa, arXiv:1208.1583v2 [nucl-th] 14 Aug 2012.
- [17] S. Hofmann, Rep. Prog. Phys. **61**, 639 (1998).
- [18] R. Kanungo, A. Sanetullaev, J. Tanaka, S. Ishimoto, G. Hagen, T. Myo, T. Suzuki, C. Andreoiu, P. Bender, A. A. Chen *et al.*, Phys. Rev. Lett. **114**, 192502 (2015).
- [19] Kiyomi Ikeda, Takayuki Myo, Kiyoshi Kato, and Hiroshi Toki, arXiv:1007.2474v2 [nucl-th] 5 Aug 2010.
- [20] G. Baur, C. Bertulani, and H. Rebel, Nucl. Phys. A **458**, 188 (1986).
- [21] R. J. de Meijer and R. Kamermans, Rev. Mod. Phys. **57**, 147 (1985).
- [22] P. E. Hodgson, Nuclear Heavy-Ion Reactions Oxford university press, 15 (1978).
- [23] A. Diaz-Torres, I. J. Thompson, and C. Beck, Phys. Rev. C **68**, 044607 (2003).
- [24] D. R. Tilley, C. M. Cheves, J. L. Godwin, G. M. Hale, H. M. Hofmann, J. H. Kelley, C. G. Sheu, and H. R. Weller, Nucl. Phys. A **708**, 3 (2002).

- 
- [25] K. Rusek, P. D. Cathers, E. E. Bartosz, N. Keeley, K. W. Kemper, and F. Marechal, Phys. Rev. C **85**, 014608 (2003).
- [26] W. Ott, R. Butsch, H. J. Jansch, K.-H. Mobius, P. Paul, G. Tungate, and E. Steffens, Nucl. Phys. A **489**, 329 (1988).
- [27] V. Mihailovic and M. Poljsak, Nucl. Phys. A **311**, 377 (1978).
- [28] V. M. Datar, D. R. Chakrabarty, S. Kumar, V. Nanal, S. Pastore, R. B. Wiringa, S. P. Behera, A. Chatterjee, D. Jenkins, C. J. Lister *et al.*, Phys. Rev. Lett. **111**, 062502 (2013).
- [29] F. C. Barker, Aus. J. Phys. **41**, 743 (1988).
- [30] <http://www.tifr.res.in/~pell/index.html>.
- [31] A. Navin, M. Dasgupta, C. V. K. Baba and A. Roy, Proceedings of DAE symposium on Nuclear Physics **32**, 59 (1989).
- [32] A. Chatterjee, K. Mahata, Suresh Kumar, A. Shrivastava, K. Ramachandran, S. K. Gupta, P. Patale, Sudheer Singh, B. K. Nayak, A. Saxena *et al.*, Proceedings of the International Symposium on Nuclear Physics, **54**, 700 (2009).

- [33] H. Bethe und J. Ashkin in "Experimental Nuclear Physics, ed. E. Segr, J. Wiley, New York, 1953, p. 253.
- [34] <http://www.ortec-online.com/-/media/ametekortec/other/introduction-charged-particle-detectors.pdf?la=en>.
- [35] A. Chatterjee, LAMPS, <http://www.tifr.res.in/pell/lamps.html>.
- [36] <https://root.cern.ch/>.
- [37] R. Rafiei, R. du Rietz, D. H. Luong, D. J. Hinde, M. Dasgupta, M. Evers, and A. Diaz-Torres, Phys. Rev. C **81**, 024601 (2010).
- [38] H. Feshbach, Annals of Phys. (N.Y.) **5**, 357 (1958), **19**, 287 (1962).
- [39] G. R. Satchler, An introduction to nuclear reaction.
- [40] P. K. Rath, S. Santra, N. L. Singh, B. K. Nayak, K. Mahata, R. Palit, K. Ramachandran, S. K. Pandit, A. Parihari, A. Pal *et al.*, Phys. Rev. C **88**, 044617 (2013).
- [41] S. Santra, S. Kailas, K. Ramachandran, V. V. Parkar, V. Jha, B. J. Roy, and P. Shukla, Phys. Rev. C **83**, 034616 (2011).

- 
- [42] S. Santra, S. Kailas, V. V. Parkar, K. Ramachandran, V. Jha, A. Chatterjee, P. K. Rath, and A. Parihari, *Phys. Rev. C* **85**, 014612 (2012).
- [43] K. O. Pfeiffer, E. Speth, and K. Bethge, *Nucl. Phys. A* **206**, 545 (1973).
- [44] R. Ost, K. Bethge, H. Gemmeke, L. Lassen, and D. Scholz, *Z. Phys.* **266**, 369 (1974).
- [45] D. Scholz, H. Gemmeke, L. Lassen, R. Ost, and K. Bethge, *Nucl. Phys. A* **288**, 351 (1977).
- [46] C. Signorini, M. Mazzocco, G. Prete, F. Soramel, L. Stroe, A. Andrichetto, I. Thompson, A. Vitturi, A. Brondi *et al.*, *Eur. Phys. J. A* **10**, 249 (2001).
- [47] J. L. Quebert, B. Frois, L. Marquez, G. Sousbie, R. Ost, K. Bethge, and G. Gruber, *Phys. Rev. Lett.* **32**, 1136 (1974).
- [48] S. K. Pandit, A. Shrivastava, K. Mahata, N. Keeley, V. V. Parkar, P. C. Rout, K. Ramachandran, I. Martel, C. S. Palshetkar, A. Kumar *et al.*, *Phys. Rev. C* **93**, 061602(R) (2016).
- [49] H. Fuchs, *Nucl. Instrum. Methods* **200**, 361 (1982).
- [50] I.J. Thompson, *Comput. Phys. Rep.* **7**, 167 (1988).

- 
- [51] F. G. Perey and G. R. Satchler, Nucl. Phys. A **97**, 515 (1967).
- [52] M. Avrigeanu and V. Avrigeanu, Phys. Rev. C **73**, 038801 (2006).
- [53] H. An and C. Cai, Phys. Rev. C **73**, 054605 (2006).
- [54] E. J. Schneid, A. Prakash, and B. L. Cohen, Phys. Rev. C **156**, 1316 (1967).
- [55] P. L. Kerr, K.W. Kemper, P. V. Green, K.Mohajeri, E. G.Myers, and B. G. Schmidt, Phys. Rev. C **55**, 2441 (1997).
- [56] P. J. Blankert, H. P. Blok, and J. Blok, Nucl. Phys. A **356**, 74 (1981).
- [57] D. Chattopadhyay, S. Santra, A. Pal, A. Kundu, K. Ramachandran, R. Tripathi, D. Sarkar, S. Sodaye, B. K. Nayak, A. Saxena *et al.*, Phys. Rev. C **94**, 061602(R) (2016).
- [58] D. Chattopadhyay, S. Santra, A. Pal, A. Kundu, K. Ramachandran, R. Tripathi, B. J. Roy, T. Nag, Y. Sawant, B. K. Nayak *et al.*, Phys. Rev. C **97**, 051601(R) (2018).
- [59] D. R. Tilley, J. H. Kelley, J. L. Godwin, D. J. Millener, J. E. Purcell, C. G. Sheu, and H. R. Weller, Nucl. Phys. A **745**, 155 (2004).

- [60] E. C. Simpson, K. J. Cook, D. H. Luong, S. Kalkal, I. P. Carter, M. Dasgupta, D. J. Hinde, and E. Williams, *Phys. Rev. C* **93**, 024605 (2016).
- [61] D. Chattopadhyay, S. Santra, A. Pal, A. Kundu, K. Ramachandran, R. Tripathi, B. J. Roy, T. Nag, Y. Sawant, B. K. Nayak *et al.*, *Phys. Rev. C* **98**, 014609 (2018).
- [62] A. Shrivastava, A. Navin, A. Diaz-Torres, V. Nanal, K. Ramachandran, M. Rejmund, S. Bhattacharyya, A. Chatterjee, S. Kailas, A. Lemasson *et al.*, *Phys. Lett. B* **718**, 931 (2013).
- [63] J. E. Bowsher, T. B. Clegg, H. J. Karwowski, E. J. Ludwig, W. J. Thompson and J. A. Tostevin, *Phys. Rev. C* **45**, 2824 (1992).
- [64] L. C. Chamon, B. V. Carlson, L. R. Gasques, D. Pereira, C. D. Conti, M. A. G. Alvarez, M. S. Hussein, M. A. C. Ribeiro, J. E. S. Rossi, and C. P. Silva, *Phys. Rev. C* **66**, 014610 (2002).
- [65] X. Li, C. Liang, and C. Cai, *Nucl. Phys. A* **789**, 103 (2007).
- [66] B. Buck and A. C. Merchant, *J. Phys. G: Nucl. Phys.* **14**, L211 (1988).
- [67] F. Ajzenberg-Selove, *Nucl. Phys. A* **490**, 52 (1988).
- [68] R. J. Spiger and T. A. Tombrello, *Phys. Rev.* **163**, 964 (1967).

- 
- [69] M. Ivanovich, P. G. Young, and G. G. Ohlsen, Nucl. Phys. A **110**, 441 (1968).
- [70] S. Cohen and D. Kurath, Nucl.Phys. A **101**, 1 (1967).
- [71] K. J. Cook, E. C. Simpson, D. H. Luong, S. Kalkal, M. Dasgupta, and D. J. Hinde, Phys. Rev. C **93**, 064605 (2016).
- [72] G. R. Kelly, N. J. Davis, R. P. Ward, B. R. Fulton, G. Tungate, N. Keeley, K. Rusek, E. E. Bartosz, P. D. Cathers, D. D. Caussyn *et al.*, Phys. Rev. C **63**, 024601 (2000).
- [73] P. Schwandt, Snoopy8Q, IUCF Report, Computer Program Library, Indiana Univ. Cyclotron facility.
- [74] S. Raman, C. W. Nestor, Jr., and P. Tikkanen, At. Data Nucl. Data Tables **78**, 1 (2001).
- [75] N. G. Jonsson, A. Backlin, J. Kantele, R. Julin, M. Luontama and A. Passoja, Nucl.Phys. A **371**, 333 (1981).
- [76] D. Chattopadhyay, S. Santra, A. Pal, A. Kundu, B. K. Nayak, K. Mahata, K. Ramachandran, R. Tripathi, V. V. Parkar, S. Sodaye *et al.*, EPJ Web of Conferences **117**, 06022 (2016).

- [77] <http://lise.nscl.msu.edu/pace4.html>.
- [78] A. Pakou, N. Alamanos, A. Gillibert, M. Kokkoris, S. Kossionides, A. Lagoyannis, N. G. Nicolis, C. Papachristodoulou, D. Patiris, D. Pierroutsakou, Phys. Rev. Lett. **90**, 202701 (2003).
- [79] F. Souza, C. Beck, N. Carlin, N. Keeley, R. L. Neto, M. de Moura, M. Munhoz, M. D. Santo, A. Suaide, E. Szanto *et al.*, Nucl. Phys. A **821**, 36 (2009).
- [80] H. Kumawat, V. Jha, V. V. Parkar, B. J. Roy, S. Santra, V. Kumar, D. Dutta, P. Shukla, L. M. Pant, A. K. Mohanty *et al.*, Phys. Rev. C **81**, 054601 (2010).